MHD SIMULATIONS OF CORONAL HEATING

Kuan Vai Tam

A Thesis Submitted for the Degree of PhD
at the
University of St Andrews

2014

MHD Simulations of Coronal Heating

Kuan Vai Tam

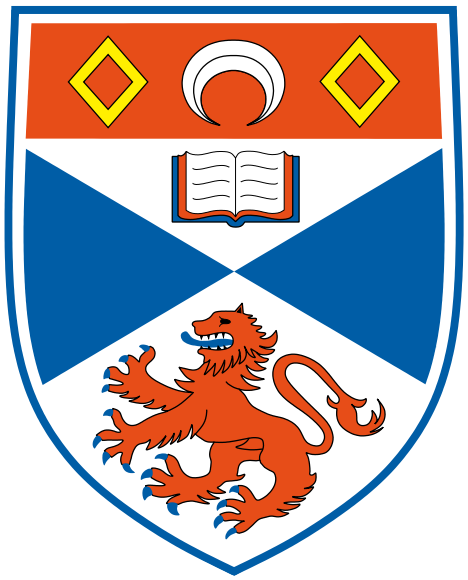

Thesis submitted for the degree of Doctor of Philosophy

of the University of St Andrews

24 January 2014

Abstract

The problem of heating the solar corona requires the conversion of magnetic energy into thermal energy. Presently, there are two promising mechanisms for heating the solar corona: wave heating and nanoflare heating. In this thesis, we consider nanoflare heating only. Previous modelling has shown that the kink instability can trigger energy release and heating in large scale loops, as the field rapidly relaxes to a lower energy state under the Taylor relaxation theory. Two distinct experiments were developed to understand the coronal heating problem: the avalanche effect within a multiple loop system, and the importance of thermal conduction and optically thin radiation during the evolution of the kinked-unstable coronal magnetic field.

The first experiment showed that a kink-unstable thread can also destabilise nearby threads under some conditions. The second experiment showed that the inclusion of thermal conduction and optically thin radiation causes significant change to the internal energy of the coronal loop. After the initial instability occurs, there is continual heating throughout the relaxation process. Our simulation results show that the data is consistent with observation values, and the relaxation process can take over 200 seconds to reach the final relaxed state. The inclusion of both effects perhaps provides a more realistic and rapid heating experiment compared to previous investigations.

Declarations

I, Kuan Vai Tam, hereby certify that this thesis, which is approximately 30,000 words in length, has been written by me, that it is the record of work carried out by me and that it has not been submitted in any previous application for a higher degree. I received particular assistance in the writing of this work in respect of matters of grammar, style, vocabulary, spelling or punctuation. The assistance was provided by a non-academic member of staff.

I was admitted as a research student in September 2009 and as a candidate for the degree of Doctor of Philosophy in September 2009; the higher study for which this is a record was carried out in the University of St Andrews between 2009 and 2014.

Date: _____ Signature of Candidate: _____.
I hereby certify that the candidate has fulfilled the conditions of the Resolution and Regulations appropriate for the degree of Doctor of Philosophy in the University of St Andrews and that the candidate is qualified to submit this thesis in application for that degree.

Date: _____ Signature of Supervisor: _____.

In submitting this thesis to the University of St Andrews we understand that we are giving permission for it to be made available for use in accordance with the regulations of the University Library for the time being in force, subject to any copyright vested in the work not being affected thereby. We also understand that the title and the abstract will be published, and that a copy of the work may be made and supplied to any bona fide library or research worker, that my thesis will be electronically accessible for personal or research use unless exempt by award of an embargo as requested below, and that the library has the right to migrate my thesis into new electronic forms as required to ensure continued access to the thesis. We have obtained any third-party copyright permissions that may be required in order to allow such access and migration, or have requested the appropriate embargo below.

The following is an agreed request by candidate and supervisor regarding the electronic publication of this thesis: Embargo on both of printed copy and electronic copy for the same fixed period of one year on the following ground: Publication would preclude future publication.

Date: _____ Signature of Candidate: _____ Signature of Supervisor: _____.

Acknowledgements

First of all, I would like to thank my supervisor Alan Hood for his ceaseless advices and encouragement. This work would not have been possible without his support, and without the PhD financial aid from the UK Science and Technology Facilities Council (STFC). I have also been given a lot of useful advice by Peter Cargill, and by all of the Solar and Magnetospheric Theory Group at St Andrews.

I must also give special thanks to Andrew Haynes, Michael Bareford and James Threlfall, who have helped me so much in coding and analysis; and Tony Arber, who wrote and provided the development of the 3D MHD Lagrangian remap code which I have been using over these years. Also, thanks to my family and friends for supporting me in my life so that I can carry on my studies.

Publications

This thesis contains work which has been adapted from the following publications:

1. Avalanche effect of kinked unstable coronal loop, by K. V. Tam, A. W. Hood, P. J. Cargill and P. K. Browning (in prep.)

2. Coronal heating by magnetic reconnection in kinked unstable loops - Under thermal conduction and optically thin radiation, by K. V. Tam, A. W. Hood, P. J. Cargill, T. D. Arber and P. K. Browning (in prep.)

Collaboration statement

The numerical experiments in these papers were carrying out by myself and supervised by Alan Hood. Peter Cargill suggested a way to present the data to compare with observations. Philippa Browning provided some insights and advices to the Taylor relaxation approach and ways to present the data. Tony Arber was the original author of the *Lare* code and his advice was sought on my implementation of the optically thin radiation term.

Contents

List of Tables

Chapter 1

Introduction

1.1 The structure of the Sun

The Sun is a middle-aged star at the centre of the solar system. It is in the middle of its life cycle, roughly 4.5 billion years old. The mean radius of the Sun is approximately 700 Mm, which is about 100 times the radius of the Earth. The mass of the Sun is 2×10^{30} kg; this represents 99% of the mass in the solar system. It is composed of 73.46% hydrogen by mass (see Eddy and Ise, 1979), 24.85% helium and the remainder of heavier elements are: oxygen, carbon and so on. The Sun provides heat, light and energy to the solar system and this is one of the reasons it is of such interest to researchers.

The Sun has multiple layers in its structure (see Figure 1.1). The interior cannot be directly observed, but thanks to helioseismology (the study of wave propagation and oscillation in the Sun) and computer modeling, the interior of the Sun can be studied. The deepest of these internal layers, the core, extends from the centre of the Sun to approximately $20 - 25\%$ of the solar radius. The core is where nuclear fusion occurs: energy is primarily generated by the fusion of hydrogen

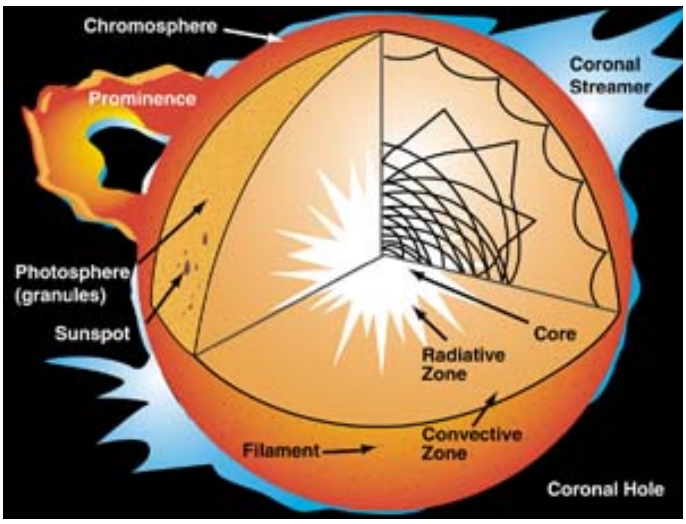

Figure 1.1: Multiple layers of solar interior and its atmosphere (Image credit: http://genesismission.jpl.nasa.gov/).

into helium which drives the power and motions of the Sun. The core temperature and density are extremely high: over 15 MK and 1.6×10^5 kg m^{-3} respectively.

The radiative zone is the next layer out from the core and has an outermost boundary of around 70% of the solar radius. It is also not directly observable. In this layer energy is transferred by radiation, while temperature in this region is slightly lower than the core. While the temperature decreases from the core temperature to 2 MK, the density also decreases from 2×10^4 kg m^{-3} to 200 kg m^{-3}. The motions of photons in this region follow random walks and it may take up to 1.7×10^5 years for a photon to reach the top of the radiative zone (see Chandrasekhar, 1943; Mitalas and Sills, 1992).

Between the radiative zone and the solar photosphere lies the convective zone. The temperature and plasma at the base of the convective zone are approximately 2 MK and 200 kg m^{-3}. This environment makes thermal convection the dominant mechanism by which heat and energy are transferred. Hot material rises to the surface, forming convective cells, which turn cool and sink to the base of the convective zone.

The next layer is the photosphere. It is a visible surface, where most of the solar radiation is emitted into space. It is approximately 500 km thick, over which the average temperature and density fall to around $6,000$ K and 2×10^{-4} kg m^{-3}. This region is influenced by the convection zone in the form of changing patterns of convective cells; this is called granulation and is observable even by ground based telescopes (see Figure 1.2). The cells are called granules and supergranules depending on their size. The typical size of a granule ranges from $150 - 2,500$ km.

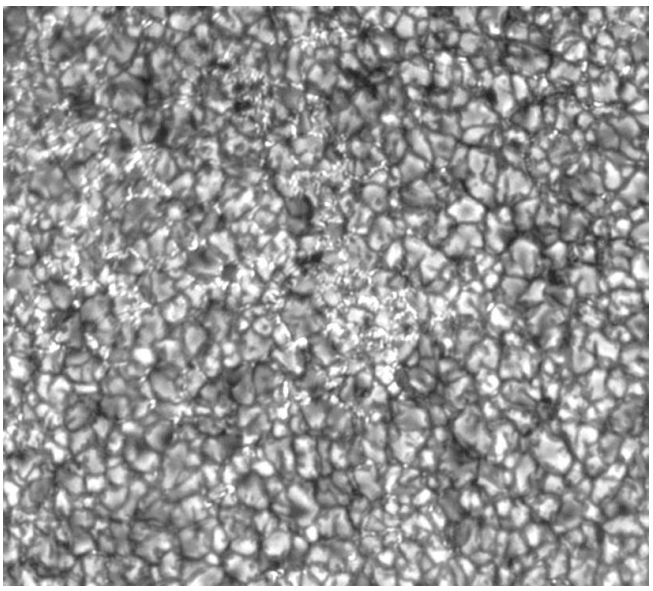

Figure 1.2: Photospheric granulation observed by the Swedish Vacuum Solar Telescope (G. Scharmer, 1997. http://solarscience.msfc.nasa.gov/).

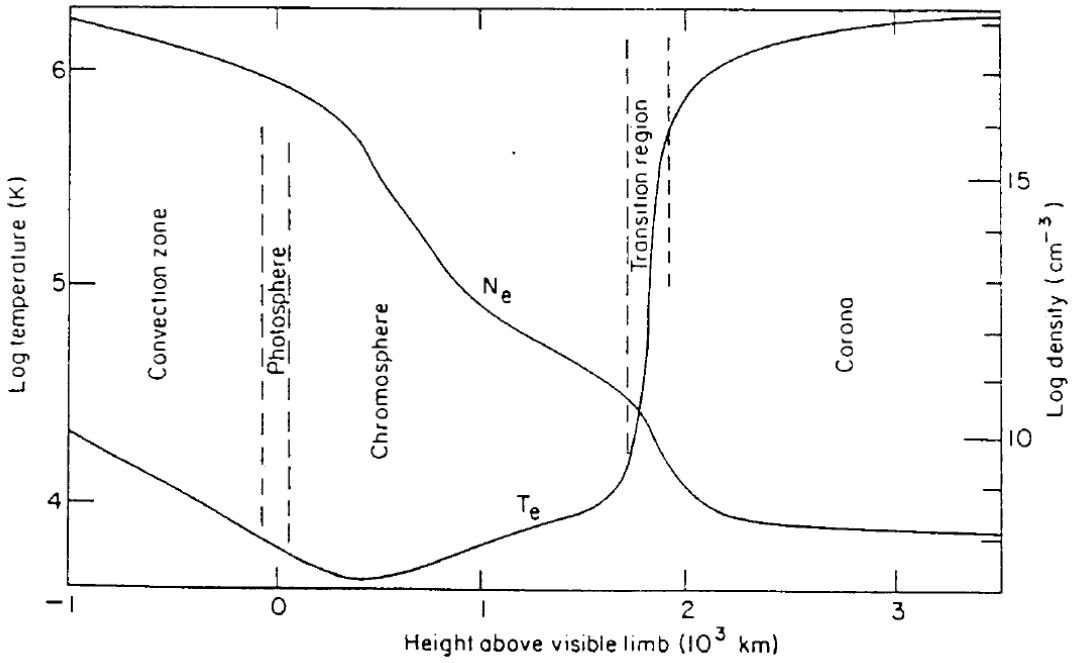

Figure 1.3: The change of temperature and density from the solar surface out into the corona as a function of height (Priest, 1982).

The average lifetime of a granule with a diameter of $1,000$ km, is approximately 8 minutes. The average lifetime of a supergranule with a diameter approximately 3×10^5 km is approximately 24 hours (Freedman and Kaufmann, 2008).

Above the Sun's photosphere, there is a layer roughly $2,000$ km thick called the chromosphere. In this region the density decreases to an average of approximately 2×10^{-8} kg m^{-3}. Chromospheric temperatures decrease from the upper photosphere temperature to a minimum of $3,800$ K, and slowly rise again to $35,000$ K at the top of the chromosphere. The temperature then rises rapidly over a very thin layer to approximately $1-2$ MK, while the density decreases dramatically in this region (see Figure 1.3, about 2 orders of magnitude). This layer is known as the transition region. It does not have a fixed thickness and varies between a few km to 200 km (Lang, 2001).

1.1.1 The solar corona and coronal heating problem

The corona is the outer layer of the solar atmosphere. It lies above the transition region and its thickness varies continuously throughout the Sunspot cycle, usually within 2 solar radii. It can only be observed if the disk of the Sun is blocked out from the line of sight, for example, during an eclipse event or through the use of an instrument like a coronagraph. The temperature of the solar corona is very high ($1-2$ MK) and the density is of the order of 10^{-12} kg m^{-3}. Figure 1.4

Figure 1.4: Left: The solar corona viewed from Chisamba, Zambia during a total solar eclipse on 7 Sep 2001. This picture was taken by Fred Espenak (http://www.mreclipse.com/). Right: The image of the Sun and its corona in a CME event observed by the Large Angle and Spectrometric Coronagraph (LASCO) of the Solar and Heliospheric Observatory satellite (SOHO) and the Solar Dynamics Observatory (SDO) on 23 Jan 2012. (NASA SDO gallery).

shows the fine structures of the solar corona. The total solar eclipse is shown on the left during the solar maximum in May 2001 and a coronal mass ejection (CME) event on Jan 2012 is shown on the right. There are many observable features in the solar corona: e.g. magnetic field structures (coronal loops) and flows of plasma to space (by solar flares, CMEs, solar winds, etc). These features are dominated by magnetic fields and appear continuously under the influence of random photospheric motion. They can be seen in both the quiet and active sun.

Active regions are areas on the solar surface that show enhanced magnetic activity and strength compared to other regions. They are the location of many of the coronal features, such as the coronal loops shown in Figure 1.5. The temperature above active regions is typically higher than other less active areas, with coronal loops loaded with hot particles/plasmas. The brightness of an active region indicates that it has a higher electron density. The typical size of a coronal loop is $20-100$ Mm and the temperature of plasma within it varies from 1 to about 6 MK (Vourlidas et al., 2001). Smaller loops are observed to have short lifetimes (from several hours to days), while the other loops have longer lifetimes (from several days to weeks). Some of the large coronal loops can be fifty to hundreds of Mm, with footpoints anchored in different active regions. Even though there are active regions on the surface of the Sun and hot coronal loops in the solar corona, there must also be a mechanism to convert the energy stored in coronal loops into heat, thus explaining the multi-million degree corona.

Figure 1.3 illustrates the change of temperature and electron number density from the photosphere out into the corona. Up until this point, the temperature of the Sun has steadily decreased with height. How can the temperature of the solar corona rise to over 1 MK as one moved away from the core of the Sun? This has been one of the most challenging questions for the researchers

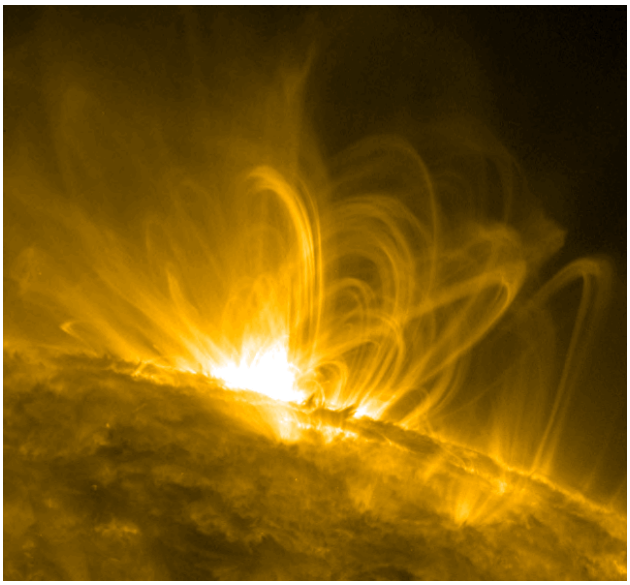

Figure 1.5: An active region of the Sun contains coronal loops of temperature at approximately 1 MK, taken by SDO AIA 171 Å in 1 Dec 2012.

in recent decades and is known as the *coronal heating problem*. The energy used to maintain the hot corona is likely to be held within the complex structure of magnetic fields above the photosphere requiring the magnetic field to store and release energy. It is accepted that highly structured magnetic fields in the solar corona can release a large amount of energy during magnetic field restructuring events (also known as reconnection). When the magnetic fields become unstable or too close to each other, reconnection events may occur and release magnetic energy, which then heats the plasma contained in the field. Reconnection events are observable in large-scale structures such as solar flares and coronal mass ejections.

Magnetic reconnection heating and wave heating are considered to be two of the likeliest mechanisms to explain the coronal heating problem. To determine which mechanism is responsible for the energy releases, we will need to consider the timescale of the photospheric motions. We first define the typical timescale for wave phenomena, Alfvén time (τ_A), by letting the length of a typical coronal loop be L and dividing it by the Alfvén speed (v_A, the speed of a plasma/wave propagates in the direction of the magnetic field), i.e. $\tau_A = L/v_A$. Here, if the timescale of photospheric motions is less than the Alfvén time, the photospheric motions will twist the coronal magnetic fields and bring in the hot plasma/magnetic energy, which could be released in the event of magnetic reconnection. If the timescale of photospheric motion is greater than the Alfvén time, the energy will be released rapidly and propagated in the form of MHD waves. Both wave heating and magnetic reconnection have received much attention as likely the candidates to heat the solar corona. Recent reviews of reconnection heating have been carried out by Klimchuk et al. (2008), Reale (2010) and of wave heating by Parnell and De Moortel (2012).

1.1.1.1 Nanoflare by small-scale magnetic reconnection

Solar flares are sudden and rapid phenomena with intense variations of brightness events. They are capable of releasing energy up to the order of 10^{20} J s^{-1}. Some large flares can even emit energy up to 10^{25} J s^{-1}. However, the occurrence rate of solar flares is irregular (averaged to 1 X-class flare per month); in other words, it is hardly likely to account for the coronal heating problem (Güdel et al., 2003). Therefore, numerous authors (e.g. Parker, 1972; Hudson, 1991) have instead focussed on the idea of heating by smaller flares. Lin et al. (1984) used an X-ray detector to study an event with a single solar flare which corresponded to energy emissions of 10^{20} J. They discovered that most of the emitted energy appeared to be linked to numerous smaller flares down to the detection limit of 10^{17} J. Parker (1988) suggested that the hot corona was actually heated by a very large number of *nanoflares*, with an average energy release of 10^{17} J or lower, with some larger flares which can reach up to 10^{20} J. Porter et al. (1984) have presented some evidence for small-scale energy releases which could be characteristic of nanoflares; they found that an active region with a size around 4×10^{20} m^2 produced intensity variations of $20 - 100\%$ over a timescale of $20 - 60$ seconds. That said, to maintain the multi-million degree corona, many nanoflares must occur at the same time to cover the energy loss of 10^6 J m^{-2} s^{-1} from the active region (Withbroe and Noyes, 1977). The latest observational results, carried out by Testa et al. (2013), suggest that the energy releases by nanoflare events may be even lower: of the order of a few 10^{16} J.

Several questions still remain todate, such as: What is the internal structure of coronal loops? Do they consist of single large cylindrical loops or are they made up of many smaller threads? The idea of multiple threads within a coronal loop has been used in many 1D single field line models (Cargill, 1993, 1994; Klimchuk et al., 2008; Sarkar and Walsh, 2008; Bradshaw and Cargill, 2010). For these multi-thread loops, the coronal heating term is often specified as a function of position and time and is not usually determined in a self-consistent way, as in the 3D simulations. However, there are many benefits to the multi-thread models, in that they can reproduce the observed differential emission measures of coronal loops to compare the results with observational data (See Section 6.6).

It is likely that the magnetic footpoints of a large coronal loop are not located in a single magnetic source but that field lines begin and end in several photospheric sources. This is the idea used in the *coronal tectonics* models of Priest et al. (2002) and Mellor et al. (2005). Large coronal loops will have many current sheets within them and magnetic reconnection will produce heat at these locations (see Section 1.3). This suggests that individual threads (identified by the current sheets) will be heated. However, an alternative approach is that the individual magnetic sources could be rotated by photospheric vortex motions (De Moortel and Galsgaard, 2006a,b). Thus an actual loop may consist of many closely packed twisted or stressed magnetic threads.

Our studies will show 3D simulations of cylindrical coronal loops, which, when made to be-

come kink unstable, demonstrate that a large helical current sheet forms and, once reconnection starts, that this sheet fragments into many smaller sheets. Thus, magnetic reconnection can occur over many different locations and the heating is spread throughout the volume of the loop. The loop here is defined by the region where there is non-zero current and the surrounding potential magnetic field is not heated significantly. The non-linear evolutions of a cylindrical magnetic loop and plasma, using Taylor relaxation (Section1.3.3.3), have been studied by many authors, including Browning and Van der Linden (2003), Browning et al. (2008), Hood et al. (2009) and Botha et al. (2011). Reduced magnetohydrodynamics (RMHD) simulations of coronal loops have also been performed by Rappazzo et al. (2007, 2008). The energy release occurs in the form of small, frequent, localized and impulsive events. This has been shown to hold in many magnetohydrodynamics (MHD) simulations (Hood et al., 2009; Wilmot-Smith et al., 2010; Pontin et al., 2011) for a single twisted loop. The relaxation process is triggered only when the magnetic field is unstable to a kink instability. It is this instability that creates an initial current sheet, enables magnetic field reconnection and releases the stored magnetic energy. How much energy can be released by such event depends on how much energy can be stored before a magnetic reconnection takes place, as well as the final state of the new equilibrium (Heyvaerts and Priest, 1984; Berger and Field, 1984). The most relaxed magnetic state is a potential field and the relaxed magnetic state can be determined by the conservation of magnetic helicity (see Section 1.3.3.3).

Now the question arises as to whether one unstable thread can destabilise a nearby thread. Can a single heating event trigger a neighbouring event and begin a chain reaction/avalanche? Avalanche models have been used to model solar flares (Lu and Hamilton, 1991; Lu et al., 1993; Charbonneau et al., 2001), whereby an initial release of magnetic energy at a single location rapidly spreads and excites multiple energy release sites. Does this approach play a role in coronal heating through one magnetic thread destabilising many others?

In this thesis, we focus on whether the magnetic reconnection in kink-unstable loops can supply enough energy to maintain the hot corona. We first study the possibility of whether an avalanche effect can create nanoflare heating events. Subsequently, we also examine the importance of the cooling effects of thermal conduction and optically thin radiation with respect to nanoflare heating.

1.1.1.2 Wave-based heating mechanisms

Wave heating is also considered as one of the primary coronal heating mechanisms and has been summarised in, for example, Roberts et al. (1984), Nakariakov et al. (1999), Nakariakov and Verwichte (2005) and De Moortel (2005). In the past decade, with the help of a range of ground-based and space-based instruments, a wide range of wave phenomena has been observed in the corona.

One of the most promising types of wave thought to be responsible for the coronal heating is the Alfvén wave. Due to its incompressible nature, the Alfvén wave causes no change in density and emission while transporting magnetic energy along the magnetic field line. It can only be seen by extracting the Doppler effect from the emission lines (see De Moortel and Pascoe, 2012, and Section 6.6).

Alfvén wave disturbances had been observed propagating along some small jets, are known as spicules (Zirin and Cameron, 1998; Freedman and Kaufmann, 2008) in the chromosphere. The mass of these fluxes is approximately 100 times that of the solar wind. The upflows from spicules have a typical velocity of 20 km s^{-1} and can rise up to $5,000$ km above the solar limb. The average lifetime of spicules varies from 4 to 15 minutes. Alfvén waves have also been observed in other solar phenomena, usually associated with regions with a high concentration of magnetic fluxes. However, this subject is beyond the remit of this thesis. We will consider only magnetic reconnection as the main mechanism of heating the solar corona.

1.2 Modelling the coronal magnetic field

The magnetic field of the solar corona often supports extremely hot plasma and the interaction between the field and plasma can be studied by magnetohydrodynamic (MHD) equations (Cowling, 1976; Priest, 1982), most of which will be required below. They describe the macroscopic behaviour of magnetic fields. In this thesis we develop models of the coronal magnetic field, using the MHD equations which combine Maxwell's equations, Ohm's law and fluid equations.

1.2.1 Maxwell's equations

The four Maxwell's equations are:

$$\nabla \times \mathbf{B} = \mu \mathbf{j} + \frac{1}{c^2}\frac{\partial \mathbf{E}}{\partial t}, \tag{1.1}$$

$$\nabla \times \mathbf{E} = -\frac{\partial \mathbf{B}}{\partial t}, \tag{1.2}$$

$$\nabla \cdot \mathbf{B} = 0, \tag{1.3}$$

$$\nabla \cdot \mathbf{E} = \frac{\rho_c}{\varepsilon}. \tag{1.4}$$

Equation (1.1) is Ampére's law, Eq. (1.2) is Faraday's law, Eq. (1.3) is the solenoidal condition, which states that there are no magnetic monopoles and finally Eq. (1.4) is Gauss' law, which is necessary for charge conservation. In these equations, $\mathbf{B}$ represents the magnetic field, μ is the permeability of free space, $\mathbf{j}$ is the current density, c is the speed of light in a vacuum, $\mathbf{E}$ is the

electric field perpendicular to the magnetic field, ρ_c is the charge of density and ε is the permittivity of free space. In a *vacuum space*, the two constants μ and ε are related to the speed of light, $c \approx 3 \times 10^8$ m s^{-1} $\left(\text{as } c = 1/\sqrt{\mu_0 \varepsilon_0}\right)$, while $\mu = \mu_0 = 4\pi \times 10^{-7}$ H m^{-1}, $\varepsilon = \varepsilon_0 = 8.8542 \times 10^{-12}$ F m^{-1}.

In order to simplify the equations, we can perform a dimensional analysis. The typical length-scale in the system can be considered as l_0 and the timescale as t_0. Consequently, the plasma velocity becomes $v_0 = l_0/t_0$. Using Faraday's law (Eq. 1.2), we obtain

$$|\nabla \times \mathbf{E}| \approx \frac{E}{l_0} \qquad \text{and} \qquad \left|\frac{\partial \mathbf{B}}{\partial t}\right| \approx \frac{B}{t_0}.$$

Therefore, the dimensionless electric field can be expressed in terms of velocity and magnetic field,

$$E = \frac{l_0}{t_0} B = v_0 B.$$

Consider now the following terms in Ampére's law (Eq. 1.1),

$$|\nabla \times \mathbf{B}| \approx \frac{B}{l_0} \qquad \text{and} \qquad \left|\frac{1}{c^2}\frac{\partial \mathbf{E}}{\partial t}\right| \approx \frac{1}{c^2}\frac{E}{t_0} = \frac{v_0}{c^2}\frac{B}{t_0} = \frac{v_0^2}{c^2}\frac{B}{l_0}.$$

This suggests that if $v_0 \ll c$, the displacement current term $\partial \mathbf{E}/\partial t$ can be neglected. This is commonly used in situations which model the corona. Provided that the plasma speeds remain highly non-relativistic, Ampère's law may be simplified to:

$$\nabla \times \mathbf{B} = \mu \mathbf{j}.$$

In Eq. (1.4), the charge density is $\rho_c = e(n^+ - n^-)$, where e is the charge on an electron, n^+ is the number of ions and n^- is the number of electrons per unit volume in a fully ionised hydrogen plasma. The plasma must satisfy the condition of charge neutrality, i.e. $n \gg n^+ - n^-$, where n is the total number density. Therefore, we can neglect the charge density if

$$n \gg \frac{\varepsilon}{e}\frac{v_0 B}{l_0}.$$

This implies $\nabla \cdot \mathbf{E} \approx 0$, assuming quasi-neutrality. However, $\nabla \cdot \mathbf{E}$ is never calculated as $\mathbf{E}$ will be eliminated from the system of equations we will use.

1.2.2 Ohm's law

The next equation, relating the current density to the plasma flow, magnetic field and electric field, is Ohm's law:

$$\mathbf{j} = \sigma \left(\mathbf{E} + \mathbf{v} \times \mathbf{B} \right), \tag{1.5}$$

where σ is the electrical conductivity and $\mathbf{v}$ is the plasma velocity. It provides the connection between the electromagnetic equations and the fluid equations. Combining Ohm's law (Eq. 1.5) with Faraday's law (Eq. 1.2), we obtain

$$\begin{aligned} \frac{\partial \mathbf{B}}{\partial t} &= -\nabla \times \left(\frac{1}{\sigma} \mathbf{j} - \mathbf{v} \times \mathbf{B} \right), \\ &= -\nabla \times \left(\frac{1}{\mu\sigma} \nabla \times \mathbf{B} - \mathbf{v} \times \mathbf{B} \right), \\ &= \nabla \times (\mathbf{v} \times \mathbf{B}) - \nabla \times (\eta \nabla \times \mathbf{B}), \end{aligned} \tag{1.6}$$

where $\eta = 1/(\mu\sigma)$ is the magnetic diffusivity. This equation is known as the MHD induction equation and describes the evolution of magnetic fields. This is the form of induction equation used in the *Lare3d* code (see Section 2.2) in order to allow the magnetic diffusivity to be a function of position, $\eta(x, y, z)$. By assuming a uniform η and using the solenoidal constraint (Eq. 1.3), the induction equation can be simplified further:

$$\begin{aligned} \frac{\partial \mathbf{B}}{\partial t} &= \nabla \times (\mathbf{v} \times \mathbf{B}) - \eta \nabla \times (\nabla \times \mathbf{B}), \\ &= \nabla \times (\mathbf{v} \times \mathbf{B}) - \eta \left[\nabla (\nabla \cdot \mathbf{B}) - \nabla^2 \mathbf{B} \right], \\ &= \nabla \times (\mathbf{v} \times \mathbf{B}) + \eta \nabla^2 \mathbf{B}. \end{aligned} \tag{1.7}$$

The first term in the right-hand side is known as the magnetic advection, which describes how the plasma motions affect the magnetic field. The second term is called the magnetic diffusion, which describes how the magnetic field is smoothed by the plasma flow. The ratio of these terms is called the magnetic Reynolds number, R_m. Assessing the dimension of this ratio yields:

$$R_m = \left| \frac{\nabla \times (\mathbf{v} \times \mathbf{B})}{\eta \nabla^2 \mathbf{B}} \right| \approx \frac{v_0 B / l_0}{\eta B / l_0^2} = \frac{v_0 l_0}{\eta}. \tag{1.8}$$

This number can be used to determine which of these two terms will dominate for a given plasma. In the solar corona, l_0 and v_0 are large, and $R_m \sim 10^{14}$. At this level, we can consider the plasma to be perfectly conducting (Priest and Forbes, 2000). Therefore, the magnetic field lines are *frozen* into the plasma, i.e. the field moves with the plasma flow. In this case, magnetic diffusion can be neglected and the induction equation simplifies to

$$\frac{\partial \mathbf{B}}{\partial t} = \nabla \times (\mathbf{v} \times \mathbf{B}).$$

On the contrary, by considering a very small region with the length-scale l_0 dramatically reduced will lead to cases where $R_m \ll 1$. Under this condition, the magnetic diffusion term dominates and the induction equation becomes

$$\frac{\partial \mathbf{B}}{\partial t} = \eta \nabla^2 \mathbf{B}.$$

The magnetic field will tend to relax towards a purely diffusive state, determined by the boundary conditions rather than the flow.

1.2.3 Fluid equations

Any fluid is governed by a set of equations, known as the fluid equations:

$$\frac{\partial \rho}{\partial t} + \nabla \cdot (\rho \mathbf{v}) = 0, \tag{1.9}$$

$$\rho \frac{D\mathbf{v}}{Dt} = -\nabla P + \mathbf{j} \times \mathbf{B} + \rho \mathbf{g} + \text{viscosity}, \tag{1.10}$$

$$\frac{\rho^\gamma}{\gamma - 1} \frac{D}{Dt} \left(\frac{P}{\rho^\gamma} \right) = -\mathcal{L}. \tag{1.11}$$

Equation (1.9) is the mass continuity equation. It states that the total mass of plasma remains unchanged. The quantity ρ is the mass density. This equation can be rewritten as

$$\frac{D\rho}{Dt} + \rho \left(\nabla \cdot \mathbf{v} \right) = 0, \quad \left(\text{with the use of material derivative} \quad \frac{D}{Dt} = \frac{\partial}{\partial t} + \mathbf{v} \cdot \nabla \right).$$

If $\nabla \cdot \mathbf{v} = 0$, we obtain $D\rho/Dt = 0$. Thus, the plasma is incompressible.

Equation (1.10) is the equation of motion, where $-\nabla P$ is the plasma gradient, $\mathbf{j} \times \mathbf{B}$ is the Lorentz force and $\rho \mathbf{g}$ is the gravitational force.

Equation (1.11) is the energy equation. $\mathcal{L}$ is the total energy loss function and γ is the ratio of the heat capacity at constant pressure (C_P) to heat capacity at constant volume (C_v). We take $\gamma = C_P/C_v = 5/3$ throughout this thesis as we consider the gas is simple ideal gas for perfectly ionised plasma. The energy equation can be written in several different forms. In the coronal conditions, the total energy loss function may contain various terms and is often written as

$$\mathcal{L} = -\nabla \cdot \mathbf{q} + L_r - H. \tag{1.12}$$

The first two terms on the right-hand side represent the energy losses by thermal conduction and optically thin radiation. These two terms will be discussed in Chapter 2.2. The last term is the coronal heating term where $H = H_0 + j^2/\sigma + H_v$. The term, H_0, represents the coronal heating

function (which depends on the coronal magnetic field, small scale magnetic reconnection events and wave heating), j^2/σ is the amount of ohmic heating due to large scale coronal currents and H_v is the viscous heating term. In many cases, e.g. ideal MHD, $\mathcal{L}$ is treated as zero.

1.2.4 Force-free equilibria and potential fields

Since the photospheric motions occur slowly compared to Alfvén time, we consider that these motions are time independent and that the MHD system is in static equilibria. Under these conditions, we neglect flows and assume that there is no time variation, i.e. $\mathbf{v} = 0$ and $\partial/\partial t = 0$:

$$0 = -\nabla P + \mathbf{j} \times \mathbf{B} + \rho \mathbf{g}.$$

The equation of motion which remains comprises three forces which balance each other: the pressure gradient, the Lorentz force and the gravitational force.

Under certain conditions, further simplifications may be made. For example, gravity may be neglected by considering that the length-scales in the corona are much less than the pressure scale height ($H = P_0/\rho_0 g$):

$$\left| \frac{-\nabla P}{\rho \mathbf{g}} \right| \approx \frac{P_0/l_0}{\rho_0 g} = \frac{H}{l_0} \gg 1.$$

In addition, we may also express the Lorentz force as

$$\mathbf{j} \times \mathbf{B} = \frac{1}{\mu_0} (\nabla \times \mathbf{B}) \times \mathbf{B} = \frac{1}{\mu_0} (\mathbf{B} \cdot \nabla) \mathbf{B} - \nabla \left(\frac{B^2}{2\mu_0} \right).$$

The terms on the right-hand side are known as magnetic tension and magnetic pressure. Here, we can use the ratio of plasma pressure and magnetic pressure to define a *plasma beta*, i.e.

$$\beta = \left| \frac{\nabla P}{\nabla B^2/(2\mu_0)} \right| \approx \frac{P_0/l_0}{B_0^2/(2\mu_0 l_0)} = \frac{2\mu_0 P_0}{B^2}.$$

If $\beta \gg 1$, the plasma motion is dominated by the plasma pressure force and the magnetic field is unimportant. If $\beta \ll 1$, then it is the reversed. In the solar photosphere, β is found to be close to unity and in the solar corona, the plasma β is often about $10^{-4} - 10^{-2}$ (i.e. $\beta \ll 1$) above active regions (Gary, 2001), hence the plasma pressure term may also be neglected under coronal conditions. The equation of motion may finally reduce to

$$\mathbf{j} \times \mathbf{B} = 0. \tag{1.13}$$

Any magnetic fields satisfying these conditions are called force-free: the Lorentz force vanishes everywhere. Equation (1.13) also implies that $\mathbf{j}$ is parallel to $\mathbf{B}$, hence, $\mathbf{j}$ can be expressed as a

scalar multiple of **B**. By combining Eq. (1.13) with the Ampére's law, Eq. (1.1), it becomes

$$\nabla \times \mathbf{B} = \mu_0 \mathbf{j} = \alpha\left(\mathbf{r}\right)\mathbf{B},$$

where $\alpha = \alpha\left(\mathbf{r}\right)$ is a scalar function of position and is a measure of the twist in the magnetic field.

If $\alpha = 0$, then $\nabla \times \mathbf{B}$ is zero. Therefore, $\mathbf{B} = \nabla\psi$ for some scalar potential ψ which satisfies the Laplace equation $\nabla^2\psi = \nabla \cdot (\nabla\psi) = \nabla \cdot \mathbf{B} = 0$. This is known as a potential field, which has zero-net-electric current and is the lowest possible energy state of the coronal magnetic field with a prescribed normal field component at the boundary.

If α is a non-zero constant, the magnetic field is described as being as non-potential. The simplest non-potential, highest energy field is called a *linear force-free field*, for which α is a constant and satisfies $\nabla^2\mathbf{B} = -\alpha^2\mathbf{B}$.

If α varies along field lines, then $\nabla \times \mathbf{B} = \alpha\left(\mathbf{r}\right)\mathbf{B}$ (provided $\mathbf{B} \cdot \nabla\alpha = 0$). Such a magnetic field is called a *non-linear force-free field*. It consists of electric currents and free energy. Note that if α may be varied in a magnetic field, it will allow the magnetic field to have both high and low twist regions.

1.3 Magnetic reconnection

We should begin with the concept of *magnetic field lines*. A magnetic field line is a representation of magnetic force; the spacing/density of the field line gives the field strength. A magnetic field line is a vector and contains the information of the local magnetic field. The direction of a field

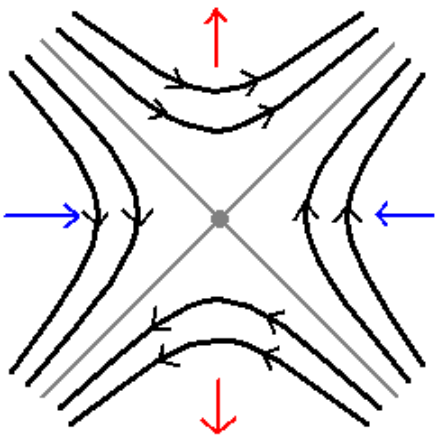

Figure 1.6: Reconnection of magnetic field lines (black curves) at an X-point caused by the inflows indicated by blue arrows. The plasma outflows are indicated by red arrows.

line is always parallel to the magnetic field. In a 3D environment, a group of these field lines can form a flux tube.

Magnetic reconnection involves a topological change in the connectivity of a magnetic field. When the magnetic field lines are stretched or stressed, the field lines will restructure themselves and link with each other. This has been studied since the 1940s and is believed to occur at a localised diffusion region where the magnetic Reynolds number is large ($R_m = v_0 l_0/\eta \gg 1$, see Eq. 1.8 for definition). It is the global reconstruction of magnetic field lines which can rapidly convert part of the stored magnetic energy into heat and plasma flow. After the release of magnetic energy, the magnetic field will reach a lower energy state and a simpler field line configuration (see Taylor relaxation: Section 1.3.3.3). We will now begin to discuss the idea of magnetic reconnection, current sheets and Taylor relaxation.

1.3.1 2D reconnection

The basic concept of 2D magnetic reconnection is shown in Figure 1.6. The opposite-aligned magnetic field lines are moving towards each other under the influence of the inflows from the top and bottom (blue arrows). When the field lines are stressed and intersect at the X-point (gray lines), new field lines may be formed, which are then carried out via the outflows (red arrows). This process allows the magnetic field lines to relax to a lower energy state by releasing the stored magnetic energy into the neighbouring region (sides with red arrows). Such a process can also accelerate particles; however, the amount of plasma and particles which may be accelerated depends on the model of magnetic reconnection. We will begin by looking at two classical mechanisms of 2D reconnection.

Sweet-Parker reconnection

A slow and steady reconnection model was suggested by Sweet (1958) and Parker (1957) as part of their attempt to find approximate solutions to 2D incompressible MHD problems. The model consists of parallel magnetic fields pointing in opposite directions (see Figure 1.7). A diffusion region (gray area) exists at the boundary of the opposite magnetic fields. It is a very long and thin region with a length of $2L$ and width of $2l$, for $L \gg l$. There are also inward plasma flows (blue arrows) pushing the magnetic field lines towards the diffusion region, creating outflows (red arrows) on the two sides. Here, the magnetic field strength is denoted by B and the plasma velocity is denoted by v, with subscriptions of i's and o's to indicate whether the variables are for the inflow or outflow regions. A null point will exist anywhere within the diffusion region at the location where magnetic reconnection occurs.

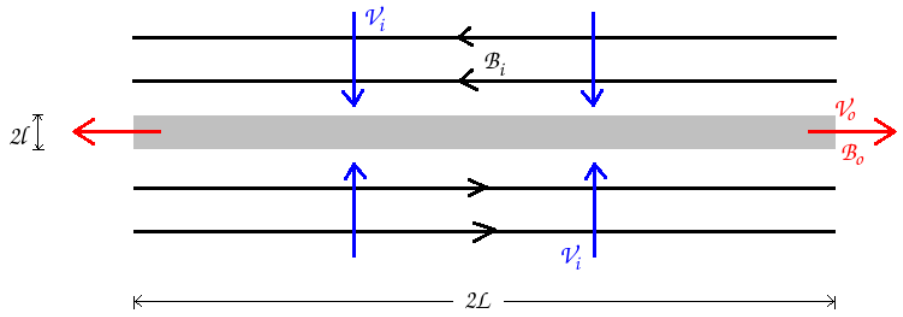

Figure 1.7: Sweet-Parker model: The magnetic field lines are marked by the black curves. Reconnection happens within the diffusion region shaded by gray colour. The blue and red arrows denote the inflows and outflows.

A simple estimate for the reconnection rate may be readily obtained. Field lines must be brought into the diffusion region at the same rate at which the plasma diffuses outwards; this is a steady process. Here, we may estimate the speed of inflow using Eq. (1.7). i.e. $v_i = \eta/l$. Next, we use the conservation of mass to obtain the equality, $4L\rho v_i = 4l\rho v_o$, since the amount of mass must be the same upon entering and leaving the diffusion region. If the plasma density is uniform in the model, the equality can also be simplified to $v_i = v_o l/L$. The velocity of the inflows may be expressed as $v_i^2 = \eta v_o/L$, by multiplying the two equations together. If we consider the plasma is accelerated by the Lorentz force, the outflow speed will then be the same as the Alfvén speed at the inflow site. i.e. $v_o = v_{Ai}$. Thus, the reconnection rate is given by

$$M_i = \frac{v_i}{v_o} = \frac{v_i}{v_{Ai}} = \frac{1}{\sqrt{R_{mi}}},$$

where M_i is known as the *Alfvén Mach number* and R_{mi} is the *magnetic Reynolds number* along the inflow region. Priest and Forbes (2000) suggested that the magnetic Reynolds number in the solar corona is approximately $R_m = 10^{14}$, thus, the reconnection rate is $M_i = 10^{-7}$. However, based on observations (Yokoyama et al., 2001), the Alfvén Mach number should be around 0.001-0.03. Therefore, the Sweet-Parker model does not have a fast enough reconnection rate to explain the reconnection of coronal magnetic fields.

Petschek reconnection

A faster reconnection model was introduced by Petschek (1964). It is an extension of the earlier Sweet-Parker model, using a similar but far smaller diffusion region (see Figure 1.8). Petschek suggested that the Sweet-Parker diffusion region should be limited to a small segment, so that the length-scales are much smaller then the global length-scale. That is $l \ll L \ll L_e$. The plasma

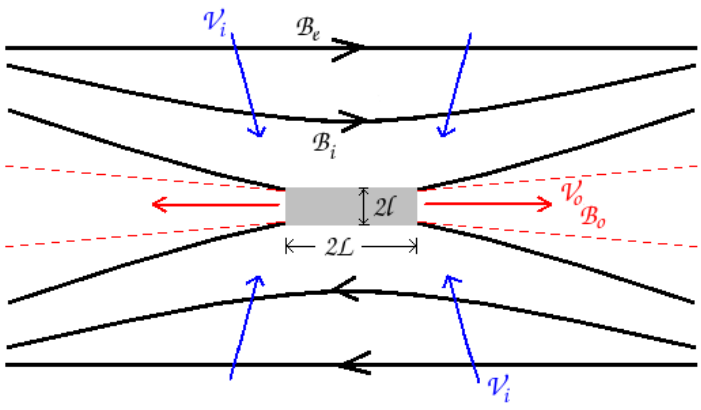

Figure 1.8: Petschek model: The magnetic field lines are marked by the black curves. The diffusion region where reconnection occurs is shaded gray; the plasma inflows and outflows are denoted by blue and red arrows.

inflows (blue arrows) in this model are not necessary perpendicular to the diffusion region, there are four standing slow shocks attached the corners of the diffusion region and the flows travel to the sides (red arrows).

Petschek considered plasma inflows that are almost uniform in his model. The magnetic field (B_i), which is pushed towards the diffusion region, is a small perturbation to the uniform field (B_e). The magnetic field in the diffusion region can be estimated as

$$B_i = B_e \left(1 - \frac{4M_e}{\pi} \log\left(\frac{L_e}{L}\right)\right),$$

where M_e is the reconnection rate. He suggested that a lower limit needs to be put into the equation, as otherwise the mechanism fails. By letting $B_i = B_e/2$ and as L_e/L decreases, the *maximum* reconnection rate is

$$M_e^* = \frac{\pi}{8 \log\left(R_{me}\right)}.$$

This reconnection rate in the solar corona is $M_e^* = 0.012$. It is significantly faster than the Sweet-Parker model and agrees with observation of estimated values (Priest, 1982). Thus, Petschek reconnection is a possible mechanism to explain reconnection of coronal magnetic fields.

1.3.2 Magnetic topology of 3D magnetic fields

In the solar corona, magnetic reconnection is unlikely to be two-dimensional. In order to understand the properties of 3D reconnection, terminologies of *magnetic topology* are necessary.

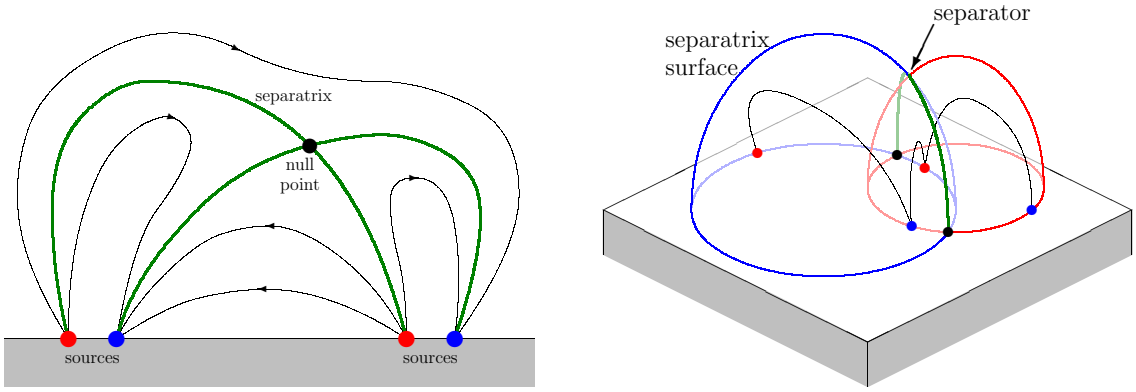

Figure 1.9: The magnetic skeleton of a 2D field (*left*) and a 3D field (*right*). The dots are either positive or negative sources. The black curves with arrows are the magnetic field lines which connect the sources. The separatrices and separators shown in green curves connect the sources and the null points (X-points). In the 3D plot, the separatrices form the separatrix surfaces. Credits: Priest et al. (1997), redrawn by Andrew Haynes.

The study of the structure and connectivity of magnetic field lines is known as *magnetic topology*. There are two ways to investigate magnetic topology: (a) the magnetic skeleton and (b) the quasi-separatrix layers of magnetic fields; a recent review of both categories was published by Longcope (2005). The magnetic skeleton is often used in the study of 3D magnetic fields that feature a finite set of null-points, spines, fans and separators, while quasi-separatrix layers apply to the cases where the magnetic field does not have a finite number of magnetic sources. However, in both cases, the lower boundary can be related to conditions on the solar photosphere. We will now describe both techniques in detail.

1.3.2.1 Magnetic skeleton

The structure of a magnetic field with a finite number of magnetic sources can be described in terms of a *magnetic skeleton*. It has been well researched by many authors and a full description of a magnetic skeleton has been presented by Priest et al. (1997). Generally speaking, a magnetic skeleton consists of several components: sources, null points, separatrices, separatrix surfaces and separators (see Figure 1.9).

In 2D MHD, *magnetic sources* are locations where magnetic field lines enter or leave the computational boundary. They are the footpoints of magnetic field lines. A *magnetic null point* is where the magnetic field strength is zero (e.g. $B_x = B_y = 0$). A null point is either of an X-type or an O-type. An example of an X-type is shown in the left hand side of Figure 1.9. Since an O-type null point is rare in MHD reconnection according to its nature, we will leave it aside. *Separatrices* are special field lines extending from the null points and divides the area into different regions of connectivity; hence, nearby field lines connect to different magnetic sources. In other

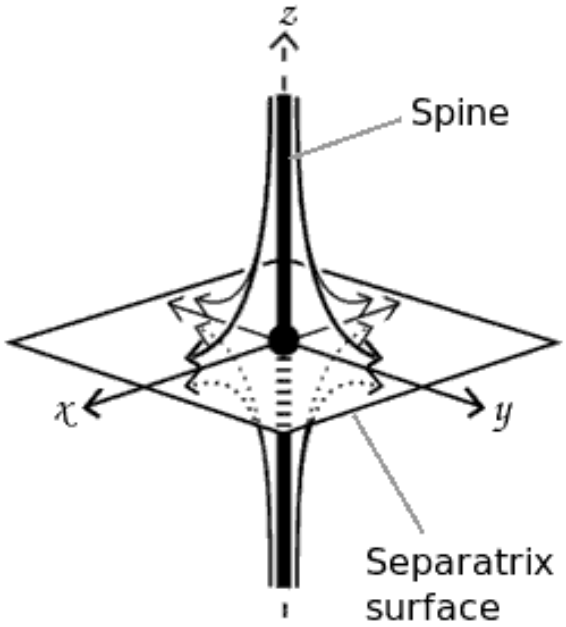

Figure 1.10: The structure of a spine and where the magnetic field lines point towards a positive null point and tangent to the fan surface. Priest et al. (1997).

words, a separatrix is a field line where the mapping of field lines from one footpoint to the other is discontinuous.

The definition of *sources* in 3D MHD is the same as in 2D, but other terms may have slightly different characteristics. In 3D MHD, a *null point* is said to be either positive or negative, in association with the idea of a *magnetic spine* (Figure 1.10). If a null point is positive, the two magnetic field lines of the spine line will point towards the null point. If the null point is negative, the two field lines of the spine line will point away from the null. 3D *separatrix surfaces* are formed by the set of magnetic field lines extending out from a positive or negative null point. These surfaces are the 3D equivalent of 2D separatrices and have discontinuities in the field line mapping across them. Furthermore, a *separator* is the location where two separatrix surfaces intersect with each other by connecting two null points.

Note that separatrix surfaces/curves are also field lines. They are the preferential locations for current sheet formation and magnetic reconnection to take place between the domains that are bounded by separatrices (or separatrix surfaces) (Longcope and Cowley, 1996; Longcope, 2001). As described previously, groups of magnetic flux (or field lines) connect sources to different *flux domains* while the photospheric motions are moving the magnetic sources and changing the properties of magnetic skeleton components. One can use the magnetic skeleton concept to monitor the location of magnetic sources and determine how magnetic flux continuously moves, changes and deforms.

1.3.2.2 Quasi-separatrix layers

As we have already mentioned, null points are not the only sites of reconnection in 3D. For example, in the case of a single coronal loop with its footpoints anchored in the photosphere, then a magnetic null point may not exist. In this case, the magnetic fields will not have a separatrix surface to divide the field lines into different flux domains, which causes difficulties in describing this system using a magnetic skeleton. However, despite the lack of magnetic nulls, quasi-separatrix layers (QSLs) can still appear, providing there is a high concentration of currents (see Priest and Démoulin, 1995; Demoulin et al., 1996). These layers have almost the same properties of separatrix surfaces, except that the mapping of the magnetic field lines between the sources are *nearly* discontinuous. In this type of reconnection, magnetic field lines will have a rapid change of connectivity. In our simulations, we do not have null points in the system and the magnetic reconnection is likely to occure in QSL. We will discuss this more in Section 6.3.

1.3.3 3D reconnection

The basic types of 3D magnetic field structures have been discussed in the previous section. 3D reconnection can occur at null points or even if the nulls are absent, for example, at separators or QSLs which maintain highly concentrated currents. This means that 3D reconnection does not only occur in a diffusion region which is just a single point, line or layer, but also in a finite volume providing its length-scale is much smaller than the global length-scale ($L \ll L_e$).

We can describe 3D reconnection in a mathematical way, through the integration of magnetic flux. We consider a surface **S** which is bounded by a closed contour C and moving with the field

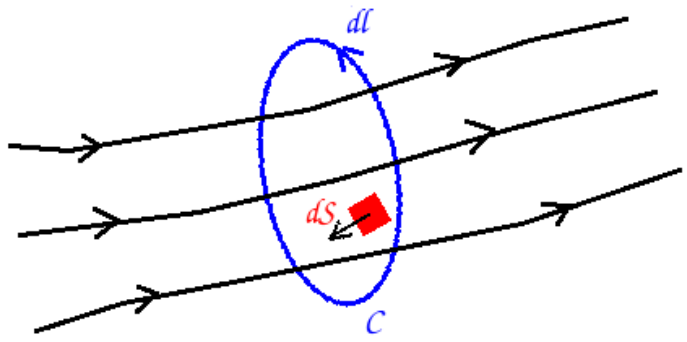

Figure 1.11: Magnetic flux: magnetic field lines (*black* arrows) through a surface (S) bounded by a closed contour (C). $d\mathbf{S}$ and $d\mathbf{l}$ are the differential vector elements of the surface and the boundary of contour respectively.

lines. The change of flux can be expressed as

$$\frac{d\Phi}{dt} = \frac{d}{dt}\int_S \mathbf{B}\cdot d\mathbf{S},$$

where Φ is the magnetic flux, $\mathbf{B}$ is the magnetic field and $d\mathbf{S}$ is the differential vector area element. This equation describes the rate of change of a component of flux passing through the surface $\mathbf{S}$ in time t. Using the Leibniz integral rule for three dimensions, we obtain

$$\frac{d\Phi}{dt} = \int_S \frac{\partial \mathbf{B}}{\partial t}\cdot d\mathbf{S} - \oint_C \mathbf{v}\times\mathbf{B}\cdot d\mathbf{l},$$

where $d\mathbf{l}$ is the differential vector element of the close contour C. The first term on the right-hand side describes the time variation of the magnetic field and the second term is the change of magnetic field due to the plasma motion. Using Stokes' theorem, Faraday's law and then the Ampére's law, this equation can be simplified as follows

$$\begin{aligned}
\frac{d\Phi}{dt} &= \int_S \left\{\frac{\partial \mathbf{B}}{\partial t} - \nabla\times(\mathbf{v}\times\mathbf{B})\right\}\cdot d\mathbf{S},\\
&= \int_S \{-\nabla\times(\eta\nabla\times\mathbf{B})\}\cdot d\mathbf{S},\\
&= -\oint_C \eta\nabla\times\mathbf{B}\cdot d\mathbf{l}, \qquad (1.14)\\
&= -\oint_C \frac{1}{\sigma}\mathbf{j}\cdot d\mathbf{l} \qquad (1.15)
\end{aligned}$$

where $\eta = 1/(\mu\sigma)$ is the magnetic diffusivity, σ is the electrical conductivity and μ is the permeability of free space.

This shows that the closed contour C will move along with the field lines and form the boundary of the flux tube. Therefore, any magnetic reconnection must be placed within the flux tube. In addition, Eq. (1.14) shows that reconnection may only occur at diffusion regions when the magnetic

2D Reconnection	3D Reconnection
1. Must occur at X-type null points.	1. Can occur at null points or in the absence of null points.
2. Occurs at a single point.	2. Occurs continually throughout diffusion region volume - not at a single point.
3. Pairs of field lines break and recombine into two new pairs of field lines.	3. Pairs of field lines or even pairs of surfaces break, but do not recombine into two new pairs of field lines or surfaces.
4. Discontinuous field line mapping.	4. Continuous or discontinuous field line mapping.
5. Stagnation type flow.	5. Counter-rotating flows.

Table 1.1: A comparison of main characteristics of 2D and 3D reconnection (Parnell and Haynes, 2010).

diffusivity (η) becomes non-zero. If a null point exists, $\eta = 0$ and $\mathbf{B} = 0$. This means that reconnection may occur at locations other than at (or near) magnetic pull points. Magnetic field lines can reconnect with each other continuously within diffusion regions; as such 3D reconnection is very different to that seen in 2D.

Numerous papers have been presented on studies of 3D reconnection (e.g. Priest and Démoulin, 1995; Priest and Forbes, 2000; Pontin et al., 2004; Pontin and Craig, 2005; Longcope, 2005; Pontin and Craig, 2006). Parnell and Haynes (2010) have also conducted a recent review of 3D reconnection and characterised the differences of 2D and 3D reconnection (see Table 1.1).

Our main interest of study is the reconnection initiated by kink instability in a magnetic field, which will have no magnetic null point in the system in response to photospheric motions. The plasma dynamics driven by the kink instability will be able to create a high concentration of magnetic currents and thus energy release via reconnection in a diffusion region (probably in QSLs) is possible. Next, we will describe the concepts of current sheet and Taylor relaxation. Both are considered the core subjects in our simulations.

1.3.3.1 Current sheets

As discussed previously, the general size of a coronal loop is large ($L = 20 - 100$ Mm) compared to the pressure scale height while the plasma density in the solar corona is low ($10^{-13} - 10^{-12}$ kg m^{-3}). The coronal magnetic field is, to a good approximation, frozen into plasma. Magnetic reconnection requires a high current density and this requires the formation of short length-scales. If there is a strong current in a small region, then we define this as a current sheet. Current sheets may be formed inside the coronal magnetic field and have a much smaller width (l) compared to the total length of the field ($l \ll L$). Current sheets which evolve with the magnetic field need to satisfy the following condition: the total pressure across the current sheet must be *continuous*, i.e.

$$p_1 + \frac{B_1^2}{2\mu} = p_2 + \frac{B_2^2}{2\mu}, \tag{1.16}$$

satisfying pressure balance on the two sides of current sheet, where the quantities with subscript 1 occur on one side of the current sheet and subscript 2 on the other.

Various papers have already focussed on 3D MHD studies of current sheet evolution (e.g. Longcope and Cowley, 1996; Longcope, 2001; Pontin et al., 2007), therefore, we will not go into detail in this thesis. We quote the mechanisms which may lead to current sheet formation and which are summarised in Priest (1982):

1. When there is an X-type neutral point reconnection, the region near the point may collapse into a current sheet.

2. If two individual magnetic field structures are pushed together, current sheets may form at the boundary between the structures.

3. If an instability rises in an equilibrium magnetic field, the field will try to adjust itself slowly to a new force-free equilibrium. However, it may not happen every time. High magnetic gradients may develop while the magnetic field is evolving. Thus current sheets and fast reconnection may occur, triggering a rapid energy release.

Three of the most important properties of current sheets are also summarised by Priest (1982):

1. In the absence of flows, a current sheet will *diffuse* away at a speed η/l, where η is the magnetic diffusivity. The magnetic field is *annihilated* and the magnetic energy will convert into heat by ohmic dissipation.

2. The region outside a current sheet is effectively *frozen-in* to the plasma. Magnetic flux and plasma may be brought towards the current sheet from the sides at speed v_i. If $v_i < \eta/l$ the current sheet will expand; if $v_i > \eta/l$, the current sheet will then become thinner; otherwise, if $v_i = \eta/l$, the current sheet will remain at a steady width.

3. The enhanced plasma pressure in the centre of the sheet will expel the material from the ends of the current sheet at the Alfvén speed ($v_A = B/\sqrt{\mu\rho}$). Magnetic flux will be ejected together with the material and therefore one of the results is field line reconnection. In 2D MHD reconnection, the centre of the current sheet is an X-type neutral point. In a *steady flow*, magnetic flux will be transported at a constant speed and therefore the rate at which the flux enters the current sheet will be equal to the flux in with the outflow:

   $$B_o v_A = v_i B i, \quad \text{or,} \quad B_o = \frac{v_i}{v_A} B_i,$$

   where the subscripts i and o denote the input and output values respectively. Thus, in the case of sub-Alfvénic inflow ($v_i < v_A$), the outflow magnetic field strength will be smaller than the inflow field strength. i.e. $B_o < B_i$. The remarkable effect here is that a current sheet will *convert magnetic energy into heat and kinetic energy*.

1.3.3.2 Parallel electric fields

The parallel electric field of *a magnetic field line* may be defined from Eq. (1.15). For example:

$$\oint_C E_\parallel \, dl = \oint_C \eta' j \cdot \hat{\mathbf{n}} \, dl = \oint_C \eta' j_\parallel \, dl.$$

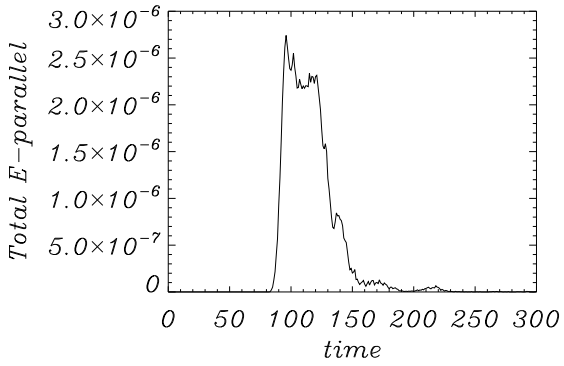

Figure 1.12: The volume-integrated parallel electric field as a function of time from one of our simulation (Case 17). In the simulation, the resistivity, $\eta = 10^{-3}$ when the magnitude of current density exceeds the critical value of $j_{crit} = 5$, otherwise it is zero. See Section 3.1 for details.

This shows that the component of electric field parallel ($E_{\|}$) is proportional to the parallel current ($j_{\|}$) scaled by the resistivity ($\eta' = 1/\sigma$). This also demonstrates that $\oint_C E_{\|}\, dl \neq 0$ is essential for magnetic reconnection, especially in cases where magnetic null points are absent (Schindler et al., 1988).

In Figure 1.12, we present the volume-integrated parallel electric field $\int E_{\|} dV$ as a function of time from one of our experimental results (Case 17; see Section 3.1 for the configuration of magnetic field). In this experiment, we simulated the energy releases in a cylindrical magnetic flux triggered by a kink instability. The resistivity is $\eta' = 10^{-3}$ when the magnitude of current density exceeds the critical value of $j_{crit} = 5$, otherwise it is zero. This figure shows that the total parallel electric field rises up from zero as the kink instability is triggered, a current sheet begins to form, magnetic reconnection occurs and is followed by a continuous decay as the magnetic field relaxed towards a minimum energy state.

1.3.3.3 Taylor relaxation

In order to have a greater understanding of the 3D reconnection of coronal loops (triggered by the kink instability), we must also introduce the Taylor relaxation theory (Taylor, 1974, 1986; Parker, 1983, 1988). An evolution begins with random photospheric motions which bring hot plasma into force-free coronal magnetic fields, while the fields are being twisted and stressed. This is how magnetic energy is stored in the field. If the twisting motions are confined to a localised region, the coronal magnetic field will be building up a net-axial-current. Meanwhile, if these motions are slower than the Alfvén travel time, the magnetic field will pass through a sequence of equilibrium until a magnetic instability eventually occurs. Once an instability occurs, it will create new current sheets and trigger magnetic reconnection to release the stored magnetic energy.

This process will convert part of the magnetic energy into other forms, such as kinetic and thermal energy. Subsequently, the current sheets will spread out and fragment. Such an event should also be able to repeat itself until the topology of the magnetic field is relaxed to a new equilibrium state or the excess magnetic field has vanished. Due to conservation of magnetic helicity (Berger and Field, 1984; Finn and Antonsen, 1985), the amount of magnetic energy that can be released during a single relaxation event is no more than the initial magnetic energy minus the magnetic energy associated with the relevant constant α field (see Section 1.2.4).

In an ideal plasma, the magnetic helicity (H) and a relative magnetic helicity (H_R) are expressed as

$$H = \int_V \mathbf{A} \cdot \mathbf{B}\, dV, \quad \text{and} \quad H_R = \int_V (\mathbf{A} + \mathbf{A}_r) \cdot (\mathbf{B} - \mathbf{B}_r)\, dV. \tag{1.17}$$

Helicity measures the total self-linkage of the given magnetic field. Here, $\mathbf{B}$ is the magnetic field and $\mathbf{A}$ is the vector potential, so that $\mathbf{B} = \nabla \times \mathbf{A}$. The quantities with subscripts (r's) indicate that they are related to a reference field. The resistive dissipation rate of magnetic helicity can be obtained from the induction equation (Eq. 1.6).

$$\frac{\partial \mathbf{B}}{\partial t} = \nabla \times (\mathbf{v} \times \mathbf{B}) + \nabla \times (\eta \nabla \times \mathbf{B}),$$

which integrates into

$$\frac{\partial \mathbf{A}}{\partial t} = \mathbf{v} \times \mathbf{B} - \eta \mathbf{j} - \nabla \phi,$$

where ϕ is an arbitrary scalar function. This function is related to our choice of a gauge function. For simplicity, we take $\phi = 0$, so that

$$\begin{aligned} \frac{dH}{dt} &= \int_V \frac{\partial \mathbf{A}}{\partial t} \cdot \mathbf{B}\, dV + \int_V \mathbf{A} \cdot \frac{\partial \mathbf{B}}{\partial t}\, dV, \\ &= -2\eta \int_V \mathbf{j} \cdot \mathbf{B}\, dV - \int_S \phi \mathbf{B} \cdot d\mathbf{S} + \int_S (\mathbf{A} \cdot \mathbf{v})\, \mathbf{B} \cdot d\mathbf{S} - \int_S (\mathbf{A} \cdot \mathbf{B})\, \mathbf{v} \cdot d\mathbf{S} \\ &\quad + \eta \int_S \mathbf{A} \times \mathbf{j} \cdot d\mathbf{S}. \end{aligned}$$

The terms on the right-hand side corresponding to the surface intergals will vanish due to a closed boundary condition, i.e. $\mathbf{v} = \mathbf{B}_n = \mathbf{j}_n = 0$ at the boundary (Biskamp, 1993). Thus, the equation above can be simplified to

$$\frac{dH}{dt} = -2\eta \int_v \mathbf{j} \cdot \mathbf{B}\, dV.$$

In order to have $dH/dt \neq 0$, it requires $j_{||} \neq 0$ and $\eta \neq 0$. This means magnetic reconnection occurs at current sheets. Taylor (1986) proposed that the process of field line reconnection destroys

all the topological invariants and only the total magnetic helicity survives. However, magnetic helicity can still be affected by global resistive diffusion; we can only treat it as a conserved quantity if, and only if, the change in magnetic helicity is much smaller than the change in magnetic energy (Berger and Field, 1984). This happens if energy dissipation occurs on small spatial scales (Bareford et al., 2011).

The dissipation rate for helicity (dH/dt) and magnetic energy (dW/dt) can be written as

$$\begin{aligned} \frac{dH}{dt} &= -2\eta \int_V \mathbf{j}\cdot\mathbf{B}\, dV \approx -2\eta \frac{B^2 L^3}{\mu_0 l}, \\ \frac{dW}{dt} &= -\eta \int_V \mathbf{j}\cdot\mathbf{j}\, dV \approx -\eta \frac{B^2 L^3}{\mu_0^2 l^2}, \end{aligned}$$

where $\mathbf{j} = \nabla\times\mathbf{B}/\mu_0$ is the current density, L is the global length-scale, l is the typical length-scale of magnetic variation and η is the resistivity (Browning, 1988). Then, the ratio of the dissipation rates is

$$\frac{d_t H/H}{d_t W/W} \sim \frac{l}{L} \ll 1,$$

where $d_t H = dH/dt$ and $d_t W = dW/dt$. This means the dissipation of helicity must be slower than the dissipation of magnetic energy. Browning et al. (2008) have demonstrated that $d_t H/H \propto 10^{-4}$ and $d_t W/W \propto 10^{-2}$ in the relaxation event of kinked unstable loop, i.e. the dissipation rate is 0.01. Thus, we may use kink instability in our simulations. Further justifications regarding conservation of helicity have been discussed by Taylor (1986) and Heyvaerts and Priest (1984).

1.4 Outline of thesis

The coronal heating problem has been a topic of great interest for decades. In this thesis, we develop a small-scale flare heating model and examine whether the energy released by nanoflares is sufficient to heat the solar corona. In the first chapter, we introduced the background of our studies. In Chapter 2, we describe the numerical method we use. In Chapter 3, we use MHD simulations to study the instability and relaxation of a kink-unstable coronal magnetic loop, which allows us to obtain the profiles of flare heating by analysing the current sheet formations, temporal evolutions, etc. In the second part of Chapter 3 (Section3.3), we extend the simulation to a two-loop system. This allows us to determine if an avalanche effect of flare heating is possible. In Chapter 4, we go back to the single loop system and introduce the effects of thermal conduction and optically thin radiation to the simulations. As by doing this we can improve our studies. We will also show whether these cooling mechanisms can impact on our previous results. The final discussion of the results is presented in Chapter 5, and finally, the ongoing future works are detailed in Chapter 6.

	Resolution:	Test Objectives:
Chapter 3	Single thread: parameter studies	
Case 1	$80^2 \times 160$	Low resolution
Case 2	$80^2 \times 160$	Low resolution with a non-zero background resistivity
Case 3	$160^2 \times 320$	Medium resolution
Case 4	$320^2 \times 640$	High resolution
Case 5	$320 \times 160 \times 640$	Twist parameter $\lambda = 1.8$ in a double size domain
Case 5b	160^3	Twist parameter $\lambda = 1.8$ for 600 Alfvén times
Case 6	$320 \times 160 \times 640$	Twist parameter $\lambda = 1.6$ in a double size domain
Case 6b	160^3	Twist parameter $\lambda = 1.6$ for 600 Alfvén times
Case 7	$320 \times 160 \times 640$	Twist parameter $\lambda = 1.4$ in a double size domain
Case 7b	160^3	Twist parameter $\lambda = 1.4$ for 600 Alfvén times
Chapter 3	Two threads: avalanche effects	
Case 8	640×320^2	Threads are 2 units away with twist parameters $\lambda = 1.8$
Case 9	640×320^2	Threads are side by side with twist parameters $\lambda = 1.8$
Case 10	640×320^2	Threads are 2 units away, the thread to be destabilised (if possible) has twist parameter reduces to $\lambda = 1.6$
Case 11	640×320^2	Threads are side by side, the thread to be destabilised (if possible) has twist parameter reduces to $\lambda = 1.6$
Case 12	640×320^2	Threads are 2 units away, the thread to be destabilised (if possible) has twist parameter reduces to $\lambda = 1.4$
Case 13	640×320^2	Threads are side by side, the thread to be destabilised (if possible) has twist parameter reduces to $\lambda = 1.6$
Chapter 4	Single thread: cooling effects	
Case 14	$100^2 \times 400$	Reference case
Case 15	$100^2 \times 400$	With thermal conduction effect
Case 16	$100^2 \times 400$	With optically thin radiation effect
Case 17	$100^2 \times 400$	With both thermal conduction and optically thin radiation
Case 18	$100^2 \times 400$	With both thermal conduction and optically thin radiation and enhance the radiation effect by 4
Case 19	$100^2 \times 400$	With both thermal conduction and optically thin radiation and enhance the radiation effect by 9
Appendix A	Single thread: enhance radiation effects by increasing length-scale by 20	
Case 14b	$100^2 \times 400$	Reference case
Case 15b	$100^2 \times 400$	With thermal conduction effect
Case 16b	$100^2 \times 400$	With optically thin radiation effect
Case 17b	$100^2 \times 400$	With both thermal conduction and optically thin radiation
Case 18b	$100^2 \times 400$	With both thermal conduction and optically thin radiation and enhance the radiation effect by 4
Case 19b	$100^2 \times 400$	With both thermal conduction and optically thin radiation and enhance the radiation effect by 9

Table 1.2: A summary of all the simulations investigated in this thesis.

Chapter 2

Numerical Techniques

2.1 Introduction

In a complex (linear or non-linear) system, finding the analytical solutions to the MHD equations is a difficult problem and therefore we should look for an alternative approach, known as numerical approximations, to find reasonable solutions.

2.1.1 Finite difference method

The *finite difference method* is one of the oldest and simplest ways to obtain approximate solutions to differential equations. It is obtained by replacing the derivatives in the MHD equations by some finite difference approximations. It approximates the complicated equations by a series of algebraic equations that can easily be solved by computers. As we are discussing numerical approximations to the exact solutions, errors will be introduced in the process. One such error is is the *truncation error*.

To keep things simple, we shall consider a 1D equation only. We let $u(x)$ be a continuous function of the independent variable, x. We assume that x can be represented on a grid, so that the domain of x is ($a \leq x \leq b$) and is subdivided by a small finite length Δx over i intervals. The definition of the derivative of the function $u(x)$ becomes

$$\frac{du}{dx} = \lim_{\Delta x \to 0} \frac{u(x + \Delta x) - u(x)}{\Delta x}.$$

If Δx is small, the fraction on the right-hand side will provide a good approximation to the derivative. Then, using a Taylor expansion, we have

$$u(x + \Delta x) = u(x) + \Delta x \frac{du}{dx} + \frac{\Delta x^2}{2} \frac{d^2u}{dx^2} + O(\Delta x^3).$$

Truncating the expansion after 3 terms, we see that the truncation error is proportional to Δx^3. For simplicity, we use subscripts to denote the location of points on the grid,

$$x_i = a + i\Delta x, \quad \text{where,} \quad i = 1, 2, 3, ..., i_{max}.$$

We define u_i as the approximation to the exact solution at $u(x_i)$. From the Taylor series, we have

$$u_{i+1} = u_i + \Delta x \frac{du}{dx}\bigg|_i + O(\Delta x^2), \quad \text{and so,} \quad \frac{du}{dx}\bigg|_i = \frac{u_{i+1} - u_i}{\Delta x} + O(\Delta x).$$

This is known as the forward difference approximation of du/dx. In the MHD system, we also have to deal with time evolution. Therefore, we introduce a similar notation for the time derivatives, with Δt being the finite timestep, so that

$$t_n = n\Delta t, \quad \text{where,} \quad n = 1, 2, 3, ..., n_{max},$$

The forward difference approximation of $\partial u/\partial x$ and $\partial u/\partial t$ for the exact solution, $u(x,t)$, becomes

$$\frac{\partial u}{\partial x}\bigg|_i^n = \frac{u_{i+1}^n - u_i^n}{\Delta x} + O(\Delta x), \quad \text{and,} \quad \frac{\partial u}{\partial t}\bigg|_i^n = \frac{u_i^{n+1} - u_i^n}{\Delta t} + O(\Delta x).$$

Recalling Taylor expansion for the forward differencing method, we can also have

$$u_{x+1}^n = u_i^n + \Delta x \frac{\partial u}{\partial x}\bigg|_i^n + \frac{\Delta x^2}{2}\frac{\partial^2 u}{\partial x^2}\bigg|_i^n + O(\Delta x^3), \tag{2.1}$$

$$u_{x-1}^n = u_i^n - \Delta x \frac{\partial u}{\partial x}\bigg|_i^n + \frac{\Delta x^2}{2}\frac{\partial^2 u}{\partial x^2}\bigg|_i^n - O(\Delta x^3). \tag{2.2}$$

The backward difference approximation can be defined the same way using Eq. (2.2),

$$\frac{\partial u}{\partial x}\bigg|_i^n = \frac{u_i^n - u_{i-1}^n}{\Delta x} + O(\Delta x), \tag{2.3}$$

and the central difference approximation can be defined by subtracting Eq. (2.1) by Eq. (2.2),

$$\frac{\partial u}{\partial x}\bigg|_i^n = \frac{u_{i+1}^n - u_{i-1}^n}{2\Delta x} + O(\Delta x^2). \tag{2.4}$$

Equation (2.4) is accurate to second order because the term, $\frac{\Delta x^2}{2}\frac{\partial^2 u}{\partial x^2}$ vanished during the subtraction. The finite approximation of $\partial^2 u/\partial x^2$ can also be found by adding Eq. (2.1) to Eq. (2.2):

$$\frac{\partial^2 u}{\partial x^2}\bigg|_i^n = \frac{u_{i+1}^n - 2u_i^n + u_{i-1}^n}{\Delta x^2} + O(\Delta x^2),$$

and it is a second order accurate method as well.

2.2 Numerical code

Due to the complexity and non-linear nature of the processes associated with the solar corona magnetic field, a numerical study is an obvious line of approach. We can solve the MHD equations and find numerical approximations by using computational techniques. In this thesis a 3D LAgrangian REmap code (*Lare3d*) is used to perform a numerical approximation to the MHD equations. The code is described in Arber et al. (2001) and solves the full set of MHD equations in three dimensions. We follow the Hood et al. (2009) experiments, with the inclusion of extra routines.

The code updates the variables at fixed locations on a three-dimensional grid. The code solves the equations in a two step process: the Lagrangian step and the remap step. The Lagrangian step is where the code works out the solutions of equations. The remap step will then work out the location of quantities and map the plasma properties back to the original grid cells. The grid is staggered to reduce the need for averaging in calculations and reduce the size of truncation errors. The code also has methods to handle shocks and is able to include extra physics such as resistivity, viscosity, thermal conduction and so on. More information regarding these terms will be discussed later on in this section.

The *Lare3d* code runs with normalised versions of the MHD equations (see Section. 1.2):

$$\begin{aligned}
\frac{\partial \rho}{\partial t} &= -\nabla \cdot (\rho \mathbf{v}), \\
\frac{\partial}{\partial t}(\rho \mathbf{v}) &= -\nabla \cdot (\rho \mathbf{v}\mathbf{v}) + \frac{1}{\mu_0}(\nabla \times \mathbf{B}) \times \mathbf{B} - \nabla P + \text{viscosity}, \\
\frac{\partial \mathbf{B}}{\partial t} &= \nabla \times (\mathbf{v} \times \mathbf{B}) - \nabla \times \left(\eta \frac{\nabla \times \mathbf{B}}{\mu_0} \right), \\
\frac{\partial}{\partial t}(\rho \epsilon) &= -\nabla \cdot (\rho \epsilon \mathbf{v}) - P \nabla \cdot \mathbf{v} + \eta \mathbf{j}^2 - \nabla \cdot \mathbf{q} - L_r + \text{viscous heating},
\end{aligned}$$

with specific energy density, $\epsilon = \frac{P}{\rho(\gamma-1)}$. The quantity $\mathbf{v}$ is the velocity, $\mathbf{B}$ the magnetic field, P the thermal pressure, $\gamma = 5/3$ the ratio of specific heats, ρ the mass density and $\mu_0 = 1.0$ the magnetic permeability in a vacuum. Note that in these equations, η is the resistivity and *not* the magnetic diffusivity, $\eta = 1/\sigma$ where σ is the conductivity.

The heat flux vector, $\mathbf{q}$, and the radiative loss function, L_r, are,

$$\mathbf{q} = -\kappa_{\parallel} (\mathbf{B} \cdot \nabla T) \frac{\mathbf{B}}{B^2} - \kappa_{\perp} (\mathbf{B} \times (\nabla T \times \mathbf{B})) \frac{1}{B^2}, \tag{2.5}$$

$$L_r = n_e^2 \chi T^{\alpha}, \tag{2.6}$$

with $\kappa_{\parallel} = \kappa_0 T^{5/2}$ W/(m K). The constant $\kappa_0 = 10^{-11}$, n_e again is the electron number density, χ and α are constants which vary at temperature ranges (see Klimchuk et al. (2008), Table 2.2 and

below). The effects of gravity are ignored in our coronal loop simulations. The quantities used in the MHD equations are normalised as

$$\mathbf{r} \rightarrow r^*\tilde{\mathbf{r}}, \quad \mathbf{B} \rightarrow B^*\tilde{\mathbf{B}}, \quad \mathbf{v} \rightarrow v_A\tilde{\mathbf{v}}, \quad P \rightarrow P^*\tilde{P}, \quad t \rightarrow t^*\tilde{t}, \quad \rho \rightarrow \rho^*\tilde{\rho},$$

where a tilde denotes a dimensionless variable. $v_A = B^*/\sqrt{\mu_0\rho^*}$ is the Alfvén speed, $t^* = r^*/v_A$ is the Alfvén transit time and $P^* = B^{*2}/\mu_0$ is the reference pressure. Here, $r^* = R$ is the loop radius and $B^* = B_0$ is the initial axial field located at $r = 0$. Removing the tildes from the dimensionless quantities, the MHD equations are finally reduced to a dimensionless form. i.e.

$$\frac{\partial \rho}{\partial t} = -\nabla \cdot (\rho \mathbf{v}), \tag{2.7}$$

$$\frac{\partial}{\partial t}(\rho \mathbf{v}) = -\nabla \cdot (\rho \mathbf{v}\mathbf{v}) + (\nabla \times \mathbf{B}) \times \mathbf{B} - \nabla P + \text{viscosity}, \tag{2.8}$$

$$\frac{\partial \mathbf{B}}{\partial t} = \nabla \times (\mathbf{v} \times \mathbf{B}) - \nabla \times (\eta \nabla \times \mathbf{B}), \tag{2.9}$$

$$\frac{\partial}{\partial t}(\rho \epsilon) = -\nabla \cdot (\rho \epsilon \mathbf{v}) - P\nabla \cdot \mathbf{v} + \eta \mathbf{j}^2 - \nabla \cdot \mathbf{q} - L_r + \text{viscous heating}. \tag{2.10}$$

The current density is in units of $B_0^*/\mu_0 r^*$ and the dimensionless temperature is determined from the ideal gas law for a fully ionised Hydrogen plasma

$$\tilde{P} = 2\tilde{\rho}\tilde{T}.$$

Quantities such as magnetic, kinetic and internal energy will also be calculated. The resistivity in our studies is not uniform: we keep a normalised η explicitly (e.g. $\eta = \eta^*\tilde{\eta}$) in the equations by taking $\eta^* = \mu_0 r^* v_A$, which follows Hood et al. (2009). Here,

$$\tilde{\eta} = \eta_b + \begin{cases} \eta_0, & |\mathbf{j}| \geq j_{crit}, \\ 0, & |\mathbf{j}| < j_{crit}. \end{cases}$$

where η_b is the background uniform resistivity and η_0 is the anomalous resistivity. The anomalous resistivity will be switched on if the magnitude of the current exceeds a critical value of $j_{crit} = 5$. This value is chosen to be greater than the maximum of the equilibrium current, ensuring that the anomalous resistivity is only switched on when a current sheet is forming.

The initial magnetic field consists of a force-free cylindrical loop, of a length of $2L$ and radius r. The magnetic field of the loop is defined as

$$B_\theta = B_0 \lambda r (1 - r^2)^3,$$

$$B_z = B_0 \sqrt{1 - \frac{\lambda^2}{7} + \frac{\lambda^2}{7}(1 - r^2)^7 - \lambda^2 r^2 (1 - r^2)^6},$$

$$\alpha = \frac{2\lambda(1 - r^2)^2(1 - 4r^2)}{B_z}.$$

Here, B_0 is a reference strength of the magnetic field. λ is a constant parameter, which is a measurement of the twist of the field. In our studies, we will mainly use $\lambda = 1.8$, for which the magnetic field is close to but just beyond the ideal kink instability threshold (see Hood et al., 2009).

2.2.1 The grid

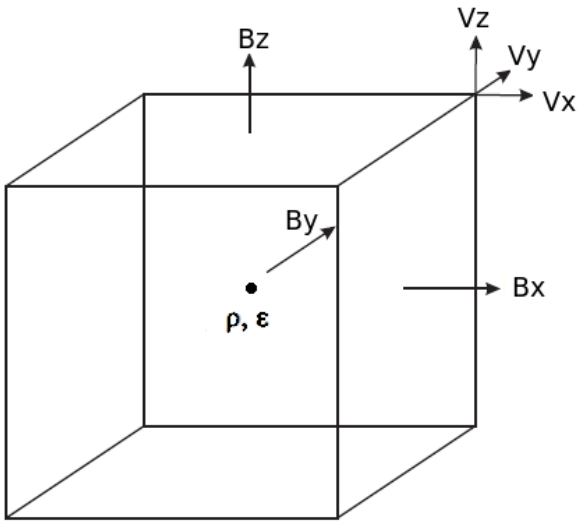

Figure 2.1: A *Lare3d* grid cell (Image credit: Arber et al., 2001).

Since we will add our routines to the code, we must be sure of the variables' location. The variables are calculated at different positions over the grid (see Figure 2.1): the scalar variables such as pressure, density and specific internal energy density are located at the cell centres of the grid; the magnetic field components are defined at the centres of the faces; the velocities and the current components are at the vertices of the grid. Here, we use the same notation as Arber et al. (2001). We define the centre of each grid cell as $xc_{i,j,k}$, $yc_{i,j,k}$ and $zc_{i,j,k}$ in the x, y and z directions; and the cell boundaries as $xb_{i,j,k}$, $yb_{i,j,k}$ and $zb_{i,j,k}$ (the i, j, k subscripts indicate the location of the cell within the computational domain). We also use $dxc_{i,j,k}$, $dyc_{i,j,k}$ and $dzc_{i,j,k}$ to denote the distances between cell centres, while $dxb_{i,j,k}$, $dyb_{i,j,k}$ and $dzb_{i,j,k}$ for the distance between cell boundaries.

For the sake of simplicity, we will consider the one-dimensional staggered grid only (see Figure 2.2). The i-th cell centre (xc_i) is represented by a dot and its cell boundaries (xb_{i-1} and xb_i) are represented by bars. This gives the definition of the distance between the cells as $dxc_i = xc_{i+1} - xc_i$, and similarly the distance between the cell boundaries is $dxb_i = xb_i - xb_{i-1}$. We can also see that the location of the cell boundary is the same as the location of the cell centre

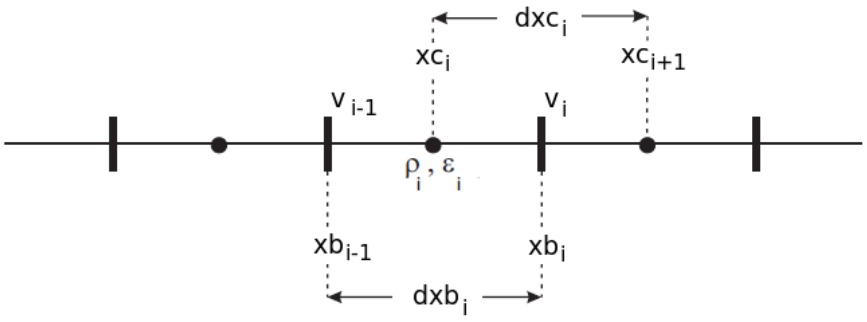

Figure 2.2: The numerical grid is staggered in *Lare3d* (Image credit: Arber et al., 2001).

plus half of the length of the grid cell, i.e. $xb_i = xc_i + dxb_i/2$. Applying this to *Lare3d*, we get

$$dxc_{i,j,k} = xc_{i+1,j,k} - xc_{i,j,k},$$
$$dxb_{i,j,k} = xb_{i,j,k} - xb_{i-1,j,k},$$

When dealing with 3D variables, volume averaging is used for scalar variables such as pressure and density, while surface averaging is used for vectors such as magnetic field and velocity. They are done by an averaging control routine in the package. This can be understood as averaging the magnitude of quantities over the neighbouring cells. For example, a vertex is shared by 8 cells: hence, the average of a scalar over 8 neighbouring cells gives its value at the common vertex. Full detail of the averaging routines can be found in Arber et al. (2001) and the *Lare* manual.

2.2.2 Boundary conditions

The boundary conditions can play a significant role in the plasma evolution. Hence, the results must be interpreted with the boundary conditions in mind. The velocity vector satisfies *line-tying* conditions over the axial boundaries, to simulate the linking of the loops to the denser chromosphere and photosphere footpoints (see Hood, 1986), with the temperature and density fixed at their initial values. For example:

$$\mathbf{v} = 0 \text{ m s}^{-1}, \quad T = 2000 \text{ K}, \quad \rho = 1.67 \times 10^{-12} \text{ kg m}^{-3}, \quad \text{at } z = \pm L.$$

The magnetic field vector components are free-floating so that

$$\frac{\partial B_x}{\partial z} = \frac{\partial B_y}{\partial z} = \frac{\partial B_z}{\partial z} = 0, \quad \text{at } z = \pm L.$$

All the variables are set to be periodic in the x and y boundaries. The initial perturbation (see Section 3.2) we will impose on the magnetic field is a small fraction of the Alfvén speed and it is only the kink unstable mode that will dominate the evolutions.

2.2.3 Lagrangian step

The thermal energy equation is solved by time advancing the internal energy density in three steps, using a time splitting method. They are used by *Lare3d*, the thermal conduction step and the optically thin radiation step. Time splitting methods can provide a simple approach to solve a complex energy system, particularly when the timescales for Alfvén disturbances, thermal conduction and optically thin radiation are distinct and the changes in temperature are small during a single timestep (see Appendix A and Einkemmer and Ostermann, 2013).

The Lagrangian step is a predictor-corrector scheme and is applied to the equation of motion, mass continuity and the energy equation. It is a second-order accurate that predicts the values of variables over half the timestep and then corrects the final values over the full timestep. The code does not use a conservative form for the energy. *Lare3d* uses artificial viscosity to couple shock heating. The prediction and correction steps will be explained in more detail with the aid of a 1D example.

2.2.3.1 1D predictor-corrector step

Consider the Lagrangian form of the 1D equations in the absence of a magnetic field

$$\frac{Dv}{Dt} + \frac{1}{\rho}\frac{\partial p}{\partial x} = 0, \tag{2.11}$$

$$\frac{D\rho}{Dt} + \rho\frac{\partial v}{\partial x} = 0, \tag{2.12}$$

$$\frac{De}{Dt} + \frac{p}{\rho}\frac{\partial v}{\partial x} = 0. \tag{2.13}$$

The variable v is the plasma velocity, p is the pressure, ρ is density and $e = \frac{p}{\rho(\gamma-1)}$ is the specific internal energy density. Recalling the 1D staggered grid from Figure 2.2, where we defined v on the boundaries with ρ and e at the cell centres, we solve the equation in Lagrangian form. The grid will move with the fluid and will not be the same as the original Eulerian configuration (this is fixed by the remap step). The distance between boundaries is defined as dxb_i and the distance between cell centres is $dxc_i = \left(v_i^{n+1/2} - v_{i-1}^{n+1/2}\right)$. Therefore, after a small timestep $(n+1)$, *the change of the cell volume* is

$$\Delta = \frac{dxb_i + \left(v_i^{n+1/2} - v_{i-1}^{n+1/2}\right)dt}{dxb_i} \simeq 1 + (\nabla \cdot \mathbf{v})\, dt.$$

$v_i^{n+1/2}$ is the vertex centred velocity, which means Δ is second-order accurate in time. Since mass conservation must hold, the density after a timestep is $\rho_i^{n+1} = \rho_i^n/\Delta$.

A spatial differencing method is used to maintain a second-order accurate scheme. For example,

$$\begin{aligned}\frac{\partial v}{\partial x}_{c_i} &= \frac{v_i^n - v_{i-1}^n}{dxb_i},\\ \frac{\partial p}{\partial x}_{b_i} &= \frac{p_{i+1}^n - p_i^n}{dxc_i}.\end{aligned}$$

Similar methods are applied to the other variables. The variables and their derivatives must be handled carefully to ensure that they are defined at the correct locations.

2.2.3.2 Predictor step

As stated early in this section, the scheme predicts the values of quantities at half of the timestep and then corrects the final values at the full timestep. The grid cell at the half timestep is

$$dxb_i^{n+1/2} = dxb_i^n + \frac{v_i^n - v_{i-1}^n}{2}\,dt,$$

and the density at the half timestep can be calculated from mass conservation; therefore,

$$\rho_i^{n+1/2} = \rho_i^n \frac{dxb_i^n}{dxb_i^{n+1/2}}.$$

The Euler equations (Eq. 2.11-2.13) give the velocity and the internal energy density at the half timestep as

$$\begin{aligned}\frac{v_i^{n+1} - v_i^n}{dt/2} &= -\frac{1}{\rho_{i+1/2}^n}\frac{p_{i+1}^n - p_i^n}{dxc_i^n},\\ \frac{e_i^{n+1/2} - e_i^n}{dt/2} &= -\frac{p_i^n}{\rho_i^n}\frac{v_i^n - v_{i-1}^n}{dxb_i^n},\end{aligned}$$

and the pressure at the half timestep is

$$p_i^{n+1/2} = e_i^{n+1/2}(\gamma - 1)\rho_i^n \frac{dxb_i^n}{dxb_i^{n+1/2}}.$$

2.2.3.3 Corrector step

The update of the velocity over the full timestep is

$$\frac{v_i^{n+1} - v_i^n}{dt} = -\frac{1}{\rho_{i+1/2}^{n+1/2}}\frac{p_{i+1}^{n+1/2} - p_i^{n+1/2}}{dxc_i^{n+1/2}}.$$

Since mass is conserved during the Lagrangian step, the mass has to be the same as at timestep n. The density will change according to the change of volume. Therefore, we can rewrite $\rho_{i+1/2}^{n+1/2} dxc_i^{n+1/2} = \rho_{i+1/2}^{n} dxc_i^{n}$. i.e.

$$\frac{v_i^{n+1} - v_i^n}{dt} = -\frac{1}{\rho_{i+1/2}^n} \frac{p_{i+1}^{n+1/2} - p_i^{n+1/2}}{dxc_i^n}.$$

This allows all the derivatives to be calculated within the original grid. Note that the velocity is defined at the cell boundary, we need to carry out an averaging with the cell centred ρ to find its value at the same location. We have

$$\rho_{i+1/2}^n = \frac{\rho_i^n dxb_i + \rho_{i+1}^n dxb_{i+1}}{dxb_i + dxb_{i+1}}.$$

The velocity at the half timestep is $v_i^{n+1/2} = \frac{1}{2}\left(v_i^n + v_i^{n+1}\right)$. It can then be used to update the energy:

$$\frac{e_i^{n+1} - e_i^n}{dt} = -\frac{p_i^{n+1/2}}{\rho_i^n} \frac{v_i^{n+1/2} - v_{i-1}^{n+1/2}}{dxb_i^n}.$$

To find the density, we need to update the grid at the same timestep n. Thus, we obtain

$$dxb_i^{n+1} = dxb_i^n + \left(v_i^{n+1/2} - v_{i-1}^{n+1/2}\right) dt,$$

and $\rho_i^{n+1} = \rho_i^n \frac{dxb_i^n}{dxb_i^{n+1}}$.

2.2.4 Remap step

At the end of each Lagrangian step, all the variables are updated on a grid that has moved with the fluid. These variables are mapped back to the original Eulerian grid. This is simply a geometrical step that retains all the physics that took place during Lagrangian step. The details of the remap step can be found in Arber et al. (2001).

2.2.5 Thermal conduction step

The thermal conduction step in *Lare3d* is of the form

$$\rho \frac{de}{dt} = \nabla \cdot \mathbf{q}.$$

The heat flux, $\mathbf{q}$, is dominated by the thermal conduction parallel to the magnetic field, provided the magnetic field does not contain any null points. However, the anisotropic form of heat con-

duction must reduce to the isotropic form when the magnetic field vanishes. The heat flux is

$$-\mathbf{q} = \kappa_{\parallel} \left(\mathbf{B} \cdot \nabla T\right) \frac{\mathbf{B}}{B^2} + \kappa_{\perp} \left(\mathbf{B} \times \left(\nabla T \times \mathbf{B}\right)\right) \frac{1}{B^2}, \tag{2.14}$$

where the first term is the heat flux parallel to the magnetic field, with $\kappa_{\parallel} = 10^{-11} T^{5/2}$ W/(m K), and the second term is the perpendicular component. In the strong field limit, the perpendicular thermal conductivity is

$$\kappa_{\perp} = \frac{4.7}{3.2} \frac{\kappa_{\parallel}}{{\omega_e}^2 {\tau_e}^2},$$

where the electron gyrofrequency is $\omega_e = eB/m_e c \approx 1.76 \times 10^{11}$ B rad/sec and the collision time is

$$\tau_e = \frac{3\sqrt{m_e}(kT_e)^{3/2}}{4\sqrt{2\pi} n_e \lambda e^4} = 3.44 \times 10^5 \frac{T_e^{3/2}}{n_e \lambda} \text{ sec},$$

(see NRL Plasma Formulary). In addition, we know that $\kappa_{\perp} = \kappa_{\parallel}$ when $B = 0$. Hence, we can approximate $\kappa_{\perp}$ by

$$\kappa_{\perp} = \frac{\kappa_{\parallel}}{1 + 0.68 {\omega_e}^2 {\tau_e}^2} = \frac{\kappa_{\parallel}}{1 + B^2 / {B^2}_{min}}.$$

Rather than work with the exact values of $B^2/B^2_{min} = 0.68 {\omega_e}^2 {\tau_e}^2$, which will be extremely small, we choose an appropriate value of B_{min} for computational convenience (see Boyd and Sanderson, 2003). Substituting our expression of $\kappa_{\perp}$ into Eq. 2.14 and with an arrangement of the terms, we can express the heat flux as

$$-\mathbf{q} = \kappa_{\parallel} \left(\frac{1}{B^2_{min} + B^2}\right) \left(\mathbf{B} \cdot \nabla T\right) \mathbf{B} + \kappa_{\parallel} \frac{B^2_{min}}{B^2_{min} + B^2} \nabla T.$$

When the magnetic field is strong, this reduces the usual expression for the parallel heat flux. However, if $B \rightarrow 0$, it becomes the correct isotropic heat flux. The advantage of such an approach is that there is no numerical difficulty when a magnetic null point is present in the computational domain. Previous simulations of thermal conduction effects on kinked unstable loops have been conducted by Botha et al. (2011).

2.2.6 Optically thin radiation step

When we begin our studies, *Lare3d* (ver 2.3) does not contain the routine of optically thin radiation as standard; here we describe our routine for optically thin radiation. The radiation loss function is a piecewise continuous form, $L_r = n_e^2 \chi T^{\alpha}$, where n_e is the electron number density while χ and α are constants over specified temperature sub-ranges (see Table. 2.1, *left*).

In c.g.s dimensional			*Lare3d* normalised		
T(K)	χ	α	T(MK)	χ_*	α
$10^{4.30} < T \leq 10^{4.60}$	$10^{-21.85}$	0	$0.0200 < T \leq 0.0398$	1.2303	0
$10^{4.60} < T \leq 10^{4.90}$	10^{-31}	2	$0.0398 < T \leq 0.0794$	870.96	2
$10^{4.90} < T \leq 10^{5.40}$	$10^{-21.2}$	0	$0.0794 < T \leq 0.2510$	5.496	0
$10^{5.40} < T \leq 10^{5.75}$	$10^{-10.4}$	-2	$0.2510 < T \leq 0.5620$	0.3467	-2
$10^{5.75} < T \leq 10^{6.30}$	$10^{-21.94}$	0	$0.5620 < T \leq 1.9950$	1	0
$10^{6.30} < T \leq 10^{7.00}$	$10^{-17.73}$	-2/3	$1.9950 < T \leq 10.000$	1.6218	-2/3

Table 2.1: The constants for optically thin radiation function used by Rosner et al. (1978).

We normalise L_r by writing the equation in the following manner:

$$L_r = n_e^2 n_{e0}^2 \chi T^\alpha T_0^\alpha = n_e^2 \chi_0 T^\alpha,$$

and $\chi_0 = n_{e0}^2 \chi T_0^\alpha$. In S.I. units, $\chi = 10^{-13}\chi_{\text{c.g.s.}}$. At $T = T_0 = 10^6$ K, $\alpha = 0$, $\chi_{\text{c.g.s.}} = 10^{-21.94}$ erg s^{-1} and $n_e = 5 \times 10^{14}$ m^{-3}. Therefore,

$$\chi_0 = 10^{-21.94} \times 10^{-13} \times \left(5 \times 10^{14}\right)^2 \times \left(10^6\right)^0 = 2.87 \times 10^{-6} \text{ J s}^{-1} \text{ m}^{-3}.$$

This agrees with the value quoted by the author of *Lare3d* (private communication, 2011). Due to the fact that *Lare3d* uses the variable of mass density, ρ, other than the number density, n_e, we have to normalise the radiative loss function again for the use of ρ.

$$\begin{aligned} L_r &= n_e^2 n_{e0}^2 \chi T^\alpha T_0^\alpha, \\ &= \frac{\rho^2}{m_p^2} \frac{\rho_0^2}{m_{p0}^2} \chi T^\alpha T_0^\alpha, \\ &= \rho^2 \frac{\chi}{m_{p0}^2} \frac{\rho_0^2}{m_p^2} T^\alpha {T_0}^\alpha. \end{aligned}$$

Here, $n_e = \rho/m_p$ and m_p is the mass of a proton. We then normalise it again for a temperature region around $T = 10^6$ K to obtain

$$L_r = \rho^2 \chi_0 \left[\frac{\chi/m_{p0}^2}{\chi_0/m_{p0}^2} \frac{{T_0}^\alpha}{{T_0}^{\alpha_0}} \right] \frac{\rho_0^2}{m_p^2} T^\alpha {T_0}^{\alpha_0} = L_r^* \left[\rho^2 \chi_* T^\alpha\right],$$

where $L_r^* = \chi_0 \frac{\rho_0^2}{m_p^2}$, and $\chi_* = \frac{\chi}{\chi_0} {T_0}^\alpha$.

At a coronal temperature of $T = T_0 = 10^6$ K, the constants are $\alpha = 0$ and $\chi_* = 1$. Thus, we have $L_r^* = 10^{-21.94} \times 10^{-13} \rho_0^2/m_p^2 = 1.148 \times 10^{-35} \rho_0^2/m_p^2$. If $T = 4 \times 10^4$ K and $\alpha = 2$,

$$\chi_* = \frac{10^{-31} \times 10^{-13}}{10^{-21.94} \times 10^{-13}} \left(10^6\right)^2 = 807.96.$$

Modified Rosner version			Klimchuk version		
T(MK)	χ_*	α	T(MK)	χ_*	α
$0.0200 < T \leq 0.0398$	1.2589	0	$0.0200 < T \leq 0.0933$	573.68	2
$0.0398 < T \leq 0.0794$	794.33	2	$0.0933 < T \leq 0.4677$	0.4668	-1
$0.0794 < T \leq 0.2510$	5.01186	0	$0.4677 < T \leq 1.5136$	1	0
$0.2510 < T \leq 0.5623$	0.3162	-2	$1.1536 < T \leq 3.5481$	1.8579	-3/2
$0.5623 < T \leq 1.9953$	1	0	$3.5481 < T \leq 7.9433$	0.1821	1/3
$1.9953 < T \leq 10.000$	1.5849	-2/3	$7.9433 < T \leq 42.658$	2.8895	0
			$42.658 < T \leq 100.00$	0.0103	1/2

Table 2.2: The modified version of optically thin radiation function from Rosner et al. (1978) (*left*) and the function used by Klimchuk et al. (2008) (*right*). These functions are of the form $\rho^2 \chi T^\alpha$ J m^{-3} s^{-1} in *Lare3d*. The normalised constant, $L_r^* = 1.2589 \times 10^{-35} \rho_0^2 / m_p^2$, for the new Rosner's version; and $L_r^* = 1.9 \times 10^{-35} \rho_0^2 / m_p^2$ J m^{-3} s^{-1} for the Klimchuk's version.

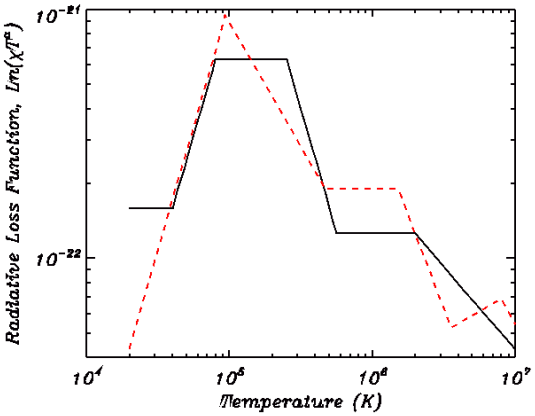

Figure 2.3: Comparison of the optically thin radiative loss function by Rosner et al. (1978) (*black solid* curve) and Klimchuk et al. (2008) (*red dashed* curve). It shows that Klimchuk's radiation is higher then Rosner's at 10^6 K.

A full normalized version is presented in Table. 2.1 (*right*) and these values agree with the ones used in the latest version of *Lare3d*.

During the study of our simulation results, we have found out that the radiative loss function used by Rosner et al. (1978) has a huge discontinuity in the piecewise temperature function. Therefore, a modified version is provided in Table. 2.2 (left-hand column). A later version of an optically thin radiative loss function used by Klimchuk et al. (2008) is also introduced in the right-hand side of the table. Throughout this thesis, we present our results using Klimchuk's version. A comparison of the two radiative loss functions is shown in Figure 2.3. It indicates that both the optically thin radiation approximations show a general decrease from a temperature of 10^6 K to 10^5 K. It also shows that the solid curve (Rosner version) has a slower energy decrease compared to the dashed curve (Klimchuk version).

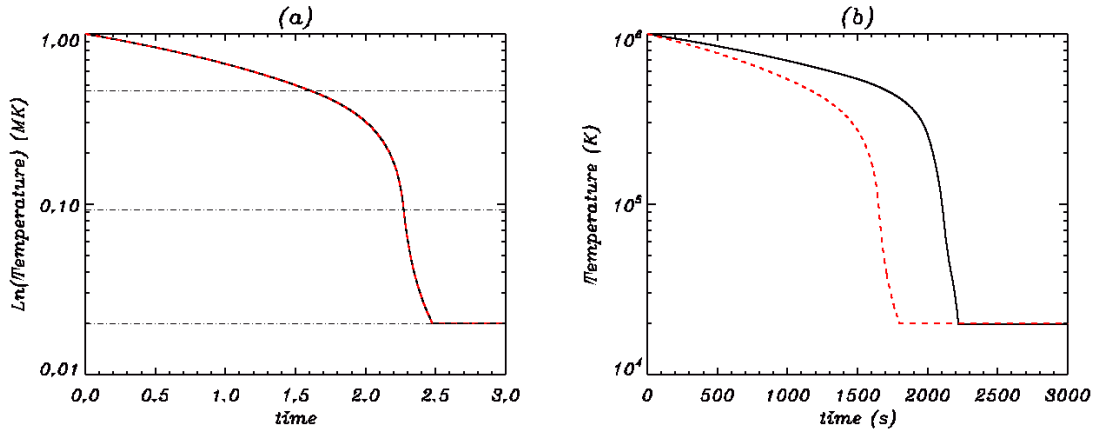

Figure 2.4: **(a)** A comparison of the analytical solution (in *black solid*) and the numerical solution of the optically thin radiative loss function (Klimchuk et al. (2008) version in *red dashed*). **(b)** 1D simulation of temperature decays from 1 MK under the effect of optically thin radiation (Klimchuk et al. (2008) version in *red dashed* and Rosner et al. (1978) version in *black solid*).

In the optically thin radiation step in *Lare3d*, the energy equation is taken as

$$\rho \frac{de}{dt} = -\rho^2 \chi T^\alpha = -L_r. \tag{2.15}$$

It is solved by a simple centred in space, finite difference scheme. Defining $\delta e = e^{n+1} - e^n$ as the change of internal energy during the timestep from t_n to t_{n+1}, we have,

$$\delta e = -\frac{\delta t}{2} \rho^n \chi^n \left((T^n)^\alpha + (T^n + \delta T)^\alpha \right) \approx -\delta t \rho^n \chi^n \left((T^n)^\alpha + \frac{\alpha}{2} (T^n)^{\alpha-1} \delta T \right),$$

where the superscript n indicates the variable is evaluated at a time $t = t_n$. Expressing δT in terms of δe will leads us to

$$e^{n+1} = e^n - \frac{L_r^n}{\rho^n / \delta t + \alpha L_r^n / (2e^n)}. \tag{2.16}$$

The timestep is restricted so that the temperature does not change by more than 1% during any timestep. This restriction is not as severe as the other CFL conditions, but it is important near the peak of the radiative losses.

A simple 1D simulation is carried out to compare the analytical solution to Eq. (2.15) and the numerical solution obtained from Eq. (2.16) (see Figure 2.4(a)). We use the optically thin radiative loss function (from Table. 2.2, *right*) to check the cooling effect at the temperature range $10^4 \leq T(\mathrm{K}) < 10^6$. For simplicity, we take $\rho = 1$, δt is fixed as a small value and the timestep restriction is not reinforced. Thus, optically thin radiation is the only cooling mechanism. The

energy equation, $de/dt = -\chi T^{\alpha}$ can be rewritten as

$$\frac{dT}{dt} = -C_1 \chi T^{\alpha}, \quad \text{and integrated to} \quad \int_{t_0}^{t} T^{-\alpha} dT = -C_1 \chi \int_{t_0}^{t} dt.$$

Here, $C_1 = (\gamma - 1)/2$ is a constant of variable conversion, which relates the energy and temperature in *Lare3d* ($\tilde{e} = \tilde{T}/C_1$). The analytical solution to the equation is

$$T(t) = \left[T(t_0)^{1-\alpha} - (1-\alpha)(t_1 - t_0) C_1 \chi\right]^{1/1-\alpha}.$$

t_0 and $T(t_0)$ are the constant variables of time and temperature for the temperature function $T(t)$ at different temperature ranges. For example, taking $T_0 = 1$ MK and $t_0 = 0$ will give us $\chi = 1$, $\alpha = 0$ and $T_1 = 0.4677$ MK since T_0 is in the temperature range of $0.4677 < T(\text{MK}) \leq 1.5136$. We then obtain

$$\begin{aligned} T_1 &= \left[{T_0}^{1-0} - 1(1-0)(t_1 - 0) C_1\right]^{1/1-0} \\ &= T_0 - C_1 t_1. \end{aligned}$$

This means that it will take time $t_1 = (T_0 - T_1)/C_1 = (1 + 0.4677)/C_1 = 1.5969$ to radiate the energy and reduce the temperature from $T_0 = 1$ MK to $T_1 = 0.4677$ MK. We can then repeat the same for the next temperature range, $0.0933 < T \leq 0.4677$, to obtain

$$T_2 = \left[{T_1}^2 - 0.4668(1+1) C_1 (t_2 - t_1)\right]^{-1/2},$$

i.e. $t_2 = t_1 + (T_1^2 - T_2^2)/(0.9336 C_1) = 2.2718$. We can repeat the same process until the temperature is reduced to the minimum.

A comparison of the analytical solution (black solid) shows a perfect match with the approximate solution (red dashed) to Eq. (2.16) in Figure 2.4(a). We have also run 1D simulations of the radiative cooling process to compare the differences between the two radiative loss functions used by Rosner and Klimchuk (see Table. 2.2 and Figure 2.4(b)). In both cases, the initial conditions are given as temperature $T = 1$ MK, magnetic field strength $B_0 = 10^{-3}$ Tesla, plasma density $\rho_0 = 1.67 \times 10^{-12}$ kg m^{-3} and a length scale of 2.5×10^6 m. The black solid curve (for Rosner's version) shows that the plasma temperature starts to decrease linearly from 1 MK. It then drops rapidly around $t = 1800$ s until it reaches 2×10^4 K, where the optically thin radiation becomes ineffective. The red dashed curve (for Klimchuk's version) shows exactly what we had expected as it follows the loss curve. The temperature of plasma starts to decay linearly until $t = 1400$ s. Then it drops rapidly again until it reaches 2×10^4 K. Thus, we are confident that we can correctly follow the temperature during the cooling steps.

2.2.7 Total energy balance

The MHD equations, Eq. (2.7-2.10) can be combined in the following form to demonstrate the conservation of energy.

$$\frac{\partial}{\partial t}\int\left(\frac{1}{2}\rho v^2+\frac{B^2}{2\mu_0}+\frac{P}{\gamma-1}\right)dV+\int\left(\frac{1}{2}\rho\mathbf{v}v^2+\frac{\mathbf{E}\times\mathbf{B}}{\mu_0}+\frac{\gamma P\mathbf{v}}{\gamma-1}-\kappa\nabla T\right)\cdot d\mathbf{S} = -\int\rho^2\chi T^{\alpha}dV. \quad (2.17)$$

The first term is the rate of change of the total energy, de/dt, where the terms within the first volume integral correspond to the total kinetic energy, $W_{Ke}=\int\frac{1}{2}\rho v^2\,dV$, total magnetic energy, $W_B=\int\frac{B^2}{2\mu_0}\,dV$ and total internal energy, $W_{Int}=\int\frac{P}{\gamma-1}\,dV$.

The second integral is the flux integral, which describes the flux of energy through the two footpoints, due to the kinetic energy, Poynting flux, the enthalpy flux and the conductive flux. The conductive flux is initially zero but there can be a heat flux through the loop ends; when the hot plasma reaches the loop ends heat will be conducted away from the corona. The periodic side boundary conditions mean that there is no net contribution to this integral from the sides. Meanwhile, the term on the right hand side of Eq. (2.17) represents the total radiative loss throughout the computational volume. By monitoring all the terms in this equation, we can identify which terms increase in response to the loss of magnetic energy. In addition, any artificial loss of energy due to numerical diffusion can also be determined.

2.3 Summary

In this chapter we introduced the *Lare3d* code and some of the numerical techniques used within the code. In *Lare3d*, the numerical grid is staggered: the variables are defined at different positions on the grid. This simplifies the code, so that there is less averaging, hence, errors are reduced. We have explained the idea of the predictor-corrector scheme and showed how the code implements the Lagrangian step and remaps the variables back to the original Eulerian grid in a similar way. We then discussed the use of thermal conduction and optically thin radiation, the additional functions designed to increase the realism of the simulations. We also discussed the differences between the two optically thin radiation functions used by Rosner et al. (1978) and Klimchuk et al. (2008). Note that *Lare3d* is a Lagrangian-remap code intended to solve the nonlinear MHD equations in three spatial dimensions; hence, it can be used to simulate a wide range of solar coronal problems.

Chapter 3

Flare Heating By Kink Instability

The energy release by nanoflares occurs in the form of small, frequent, localized and impulsive events, as discussed in Section 1.1.1.1. In this Chapter, we begin to describe our 3D coronal loop models. Previous simulations by Browning et al. (2008) confirmed the hypothesis that a kink-unstable magnetic field relaxes towards a minimum energy state in accordance with Taylor relaxation theory. However, the cases presented by Browning used a non-zero total axial current. If the coronal loops carry a net axial current, it will blur the distinction between the loop boundaries and the background magnetic field. Generally speaking, a potential magnetic field/loop should have purely axial field lines. When a coronal loop is stressed by photospheric footpoint motions, twisting motions begin. Magnetic currents will be generated and confined to some localised regions, thus, the integrated current across the cross section of the loop will be zero. Hence, in magnetic field reconnection a confined field with zero-net-axial-current is a better choice for the representation of the solar coronal loops (see Lionello et al., 1998). A mathematical description of this is presented in Section 3.1.1.

Following the work by Hood et al. (2009), an unstable magnetic field/loop is subjected to a small initial velocity disturbance in order that the kink instability will grow and develop a complex current sheet structure. Reconnection will subsequently occur, releasing magnetic energy and heating the field. The aim of our study is to identify whether such an event can also trigger an energy release in the nearby fields and therefore generate heating right across the complete, multi-threaded coronal loop structure.

We simulate the 3D nonlinear dynamics of a multi-threaded coronal loop. In observing whether it is possible to trigger an avalanche effect, we simplify things and investigate how two neighbouring magnetic loops interact when one of them becomes kink unstable first. Under what conditions can the neighbouring field release its stored magnetic energy too? We restrict our attention to two loops because the nonlinear evolution of kink instability requires high numerical resolution in order to conserve total energy and to resolve the current sheets created; there are insufficient computing resources at the present time to investigate in detail the avalanche effect in a truly multi-threaded loop. However, we can demonstrate the viability of the concept. In this section, we will look at a series of models: (a) single thread cases, which can help us study if energy release is sufficient for coronal heating; (b) cases with two or more threads, keeping one thread as

kink unstable and varying the stability properties and closeness of the nearby threads.

The outline of this chapter is shown as follows. Section 3.1 describes the MHD equations used and the numerical method for their solution, together with the initial equilibria of the magnetic fields and the boundary condition used. Section 3.2 examines how these cases evolve by detailing at their energy profiles, current sheet formation, temperature profile and field line connectivity. This section describes how the kink instability can provide sufficient energy to heat the solar corona. Section 3.3 describes the evolution of two loop studies. When energy is released from an unstable loop, it is able to trigger a faster-acting instability in a neighbouring loop; this section will also show that such events are capable of triggering an instability in a stable loop. Finally, a discussion of the results and the conclusion are presented in Section 3.4.

3.1 Numerical method

The Lare3d code has been described in detail in Section 2.2 and therefore we will not discuss it again here. Instead we will discuss the initial equilibria for the configuation of our magnetic fields.

3.1.1 Initial equilibria

In the solar corona, the ratio of gas pressure to magnetic pressure is so small (around 10^{-3}) that the magnetic field can be assumed to be force-free. Hence, $\nabla \times \mathbf{B} = \alpha(r)\mathbf{B}$. In our studies, each equilibrium magnetic thread has a zero net axial current. For simplicity, we assume that each thread can be modelled by a straight twisted cylinder, with the cylinder axis located at (x_0, y_0) and use the smooth α profile used by Hood et al. (2009). For $r^2 = (x - x_0)^2 + (y - y_0)^2 \leq 1$, the magnetic field components of each thread have the form

$$\begin{aligned} B_\theta &= B_0 \lambda r (1 - r^2)^3, \\ B_z &= B_0 \sqrt{1 - \frac{\lambda^2}{7} + \frac{\lambda^2}{7}(1 - r^2)^7 - \lambda^2 r^2 (1 - r^2)^6}, \\ \alpha &= \frac{2\lambda(1 - r^2)^2(1 - 4r^2)}{B_z}, \end{aligned} \tag{3.1}$$

and for $r^2 \geq 1$,

$$B_\theta = 0, \qquad B_z = B_0 \sqrt{1 - \frac{\lambda^2}{7}}, \qquad \alpha = 0, \tag{3.2}$$

B_0 is the magnetic field strength on $r = 0$ and λ is a constant parameter, which is a measurement of the twist of the field. Figure 3.1 shows the isosurface of the magnetic field strength and the magnetic field lines from one of our simulations to illustrate the initial equilibrium of magnetic

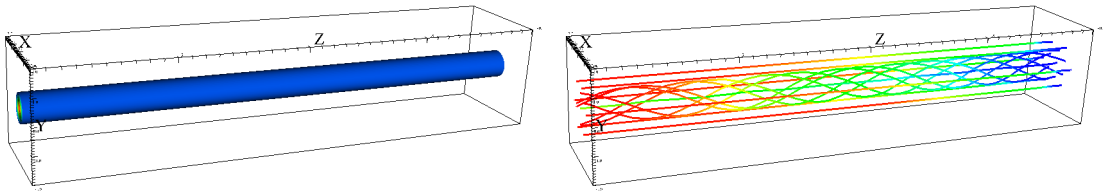

Figure 3.1: The isosurface plot of the magnitude of magnetic field (*left*) and the magnetic field lines (*right*) to illustrate the configuration of the initial equilibrium. The field lines are coloured by their lengths (from red to blue).

field.

The choice of λ is restricted by the fact that $B_z > 0$ and, hence, $\lambda < 64/965\sqrt{1351} = 2.438$. λ_{crit} is called a stability threshold, which is a particular value to identify whether the loop is stable (if $\lambda < \lambda_{crit}$) or unstable (if $\lambda > \lambda_{crit}$). The stability threshold varies based upon the aspect-ratio of the magnetic loop. In our study, the aspect-ratio of the loops is 1:20 and therefore the stability threshold is $\lambda_{crit} = 1.586$. This critical value is found by using a numerical instability code called *CILTS* (see Browning and Van der Linden, 2003; Browning et al., 2008; Bareford et al., 2011, and Section 3.2.2).

Other forms of equilibrium fields have been studied by Browning and Van der Linden (2003), Browning et al. (2008), Hood et al. (2009), Bareford et al. (2010) and Bareford et al. (2011). Their studies consisted of two constant-α regions surrounded by a uniform axial potential field. Since the α profile has both positive and negative values, the total magnetic helicity in the equilibrium field will be relatively small, therefore, the Taylor relaxed state will be very close to a potential field. i.e. in the mid-plane $z = 0$, the magnetic fields will evolve to a uniform field in the axial direction. B_x and B_y will be non-zero only near the photospheric boundaries. Here, we assume that the photospheric motion (v_θ) generates the magnetic field ($B_\theta(r)$). Then if $v_\theta = 0$ outside the magnetic field, $B_\theta(r = 1) = 0$ for $r \geq 1$. The integrated current across the cross section with $j_z = \frac{1}{r}\frac{d}{dr}(rB_\theta(r))$ becomes

$$\int_{r=0}^{r=1} j_z \, r \, dr \, d\theta = 2\pi \int_{r=0}^{r=1} \frac{d}{dr}(rB_\theta) \, dr = 2\pi \left[rB_\theta(r)\right]_0^1 = 0.$$

Thus, the magnetic field carries zero axial net current.

3.2 Parameter studies with single loop

A number of single thread simulations are described in order to understand the initial setup. We will then modify this to include more threads as we move towards a more realistic avalanche

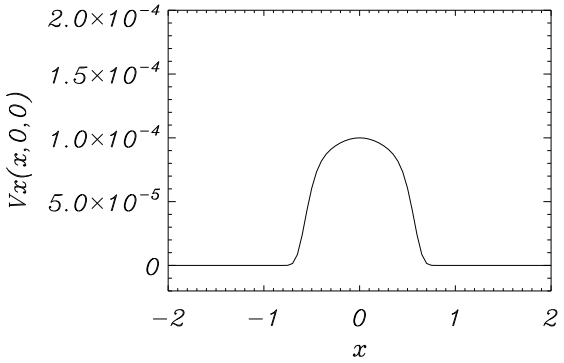

Figure 3.2: The initial profile of $v_x(x,0,0)$ for Case 1, i.e. the initial perturbation added to the magnetic field.

model. The computational domains have specified sizes of $L_x = L_y = 4$ and $L_z = 20$ in the axial direction. The width of the domains is 4 times the radius of the coronal loop. It has been shown by Browning et al. (2008) that the outer boundary does not significantly influence the stability properties of the magnetic field (with zero net current), if it is more than twice the radius of the magnetic field. An unstable equilibrium thread will always be at the centre of the computational domain. It has a twist parameter of $\lambda = 1.8$, which is beyond the threshold for magnetic stability. The thread is given an initial helical velocity perturbation, which will allow the instability in the loop to develop. When $r \leq 1$, the initial perturbation is of the form

$$\begin{aligned} v_r(r,\theta) &= -C_1 \frac{B_z^2 + B_\theta^2}{B_z + krB_\theta} \left(1 - 2r^2 - 8(2r)^6\right) e^{-4r^4} \cos\left(\frac{\pi z}{2L}\right), \\ v_\theta(r,\theta) &= \frac{B_z v_\perp}{B_z^2 + B_\theta^2}, \\ v_z(r,\theta) &= C_1 \frac{B_\theta v_\perp}{B_z^2 + B_\theta^2}. \end{aligned}$$

With v_r and v_θ prescribed, the cartension velocity components are given by

$$\begin{aligned} v_x &= v_r \cos\theta + v_\theta \sin\theta, \\ v_y &= v_r \sin\theta - v_\theta \cos\theta. \end{aligned}$$

Here, v_r is the radial component of the perturbed velocity, $2L$ is the loop length, $r = \sqrt{x^2 + y^2}$ is the radial coordinate, $k = 6/20$ is the wave number and the constant $C_1 = 10^{-4}$ reduces the amplitude so that the perturbation is only small (see Figure 3.2).

This perturbation will trigger a kink instability since the velocity is of the form $v(r,\theta) = e^{i(m\theta + kz)} \cos\left(\frac{\pi z}{2L}\right)$ with a helical kink mode ($m = 1$). Since the loop is unstable to the ideal kink instability, the initial perturbation will eventually grow in amplitude and the kink instability

will develop reasonably fast.

The simulations are either running at a low resolution with a $80^2 \times 160$ grid, a medium resolution with a $160^2 \times 320$ grid, or a high resolution with a $320^2 \times 640$. It takes about three days to run a 300 Alfvén times simulation under high resolution with 32 processors. Two forms of resistivity are also considered; a background resistivity (η_b) to be chosen and an anomalous resistivity ($\eta_0 = 10^{-3}$) for $|\mathbf{j}| \geq j_{crit} = 5$. The anomalous resistivity is considered as reasonably large and was used by Hood et al. (2009), Bareford et al. (2010) and Bareford et al. (2011).

By the end of this section, we will have knowledge regarding the change in various parameters in the code. We will also outline a number of ways to study the numerical results. A ummary of the simulations is given below.

Case 1: A zero background resistivity ($\eta_b = 0$) is chosen and run with low resolution.

Case 2: A non-zero background resistivity ($\eta_b = 2 \times 10^{-4}$) with low resolution.

Case 3: Zero background resistivity ($\eta_b = 0$) with medium resolution. This is our reference case.

Case 4: Zero background resistivity ($\eta_b = 0$) with high resolution.

Case 5: A single thread without initial perturbation in a double size domain (see Table 1.2 at the end of Chapter 1). The twist parameter is $\lambda = 1.8$ in this case.

Case 6: As Case 5 with a marginally unstable single thread with $\lambda = 1.6$.

Case 7: As Case 5 with a stable single thread with $\lambda = 1.4$.

3.2.1 Integrated energies as function of time

To begin our analysis, we studied the behaviour of the three different energy terms, integrated over the computational volume. The three energy terms are magnetic energy (W_B), kinetic energy (W_{Ke}) and internal energy (W_{Int}) and their definitions are

$$W_B = \int \frac{B^2}{2\mu_0}\, dV, \quad W_{Ke} = \int \frac{1}{2}\rho v^2\, dV, \quad \text{and} \quad W_{Int} = \int \frac{P}{\gamma - 1}\, dV.$$

Consider Case 1 and Case 2, which are both run at a low resolution but with a different background resistivity. The black curves in Figure 3.3 show the simulation results for Case 1 ($\eta_b = 0$). They show that the volume integrated energy profiles, along with the helicity and the maximum current profiles, remain unchanged initially. At time $t = 50$, the kink instability starts and the

thread becomes unstable. The total magnetic energy begins to drop from 87.76 quickly and then levels off at around $t = 200$. This behaviour is expected from the Taylor relaxation theory. The subsequent loss of magnetic energy becomes slower as the field relaxes towards a minimum energy state. By the end of the simulation, the magnetic energy has dropped by 1.6713.

Due to energy conservation, the loss of magnetic energy has to be converted into an other form of energy, such as kinetic and internal energy. Therefore, as the magnetic energy drops, the kinetic and internal energies rise and eventually the magnetic field will reach a new, lower minimum energy state. Such behaviour can be seen in all of the simulations presented in this thesis.

The kinetic energy begins to rise very slowly at $t = 30$ and then peaks twice, reaching a maximum of 0.059 at $t = 135$, followed by a fast decay. There is a possible third peak which appears at a much later time at $t = 220$, while the field is trying to relax to a lower energy state through a sequence of small reconnection events. The internal energy also remains at zero initially, i.e. there is no heating during this stage, then rises rapidly as the magnetic energy is released from $t = 50$, followed by a levelling off from $t = 200$. By the end of the simulation, the internal energy has increased by 1.009, while the total energy lost is 0.661. This loss of total energy in the field is $0.661/87.76 < 1\%$ of the initial total energy. Such loss is presumably due to numerical diffusion and thus we can conclude that energy is balanced within the grid resolution. Moreover, this loss will be reduced as we increase the resolution.

The helicity and maximum current plots also show a similar evolution, which demonstrates that the instability occurred around $t = 50$ to $t = 150$. Figures like these can help us to identify the details over the evolution. The key result is that the change of helicity is so small compared to the loss of magnetic energy, which is supported by the Taylor relaxation theory (Section 1.3.3.3).

Introducing a background resistivity alters the evolution of the instability. The red curves in Figure 3.3 show the results for Case 2 (with non-zero background resistivity, $\eta_b = 2 \times 10^{-4}$). The magnetic energy is seen to be diffused by the background resistivity before the instability takes place. It begins to dissipate constantly from $t = 0$ to $t = 70$. It then decays quickly until the end of the simulation. Meanwhile, the kinetic energy remains at zero and then increases slowly from $t = 50$. It can be seen that it peaks three times during the simulation with a maximum of 0.036 at $t = 165$. The internal energy also increases at a constant rate between $t = 0$ to $t = 70$. Subsequently, it increases again between $t = 100$ and $t = 200$ and then the increase becomes slower until the end of our simulation. Overall, the internal energy increases by 1.237, while the magnetic energy drops by 1.637. The total energy remains constant until $t = 70$, followed by a rapid drop towards 0.4 governed by the mainly magnetic forces. The energy loss to numerical dissipation is again less than 1%. From the results obtained, we can see that most of the magnetic energy is converted to internal energy. We can also see that the background resistivity does alter

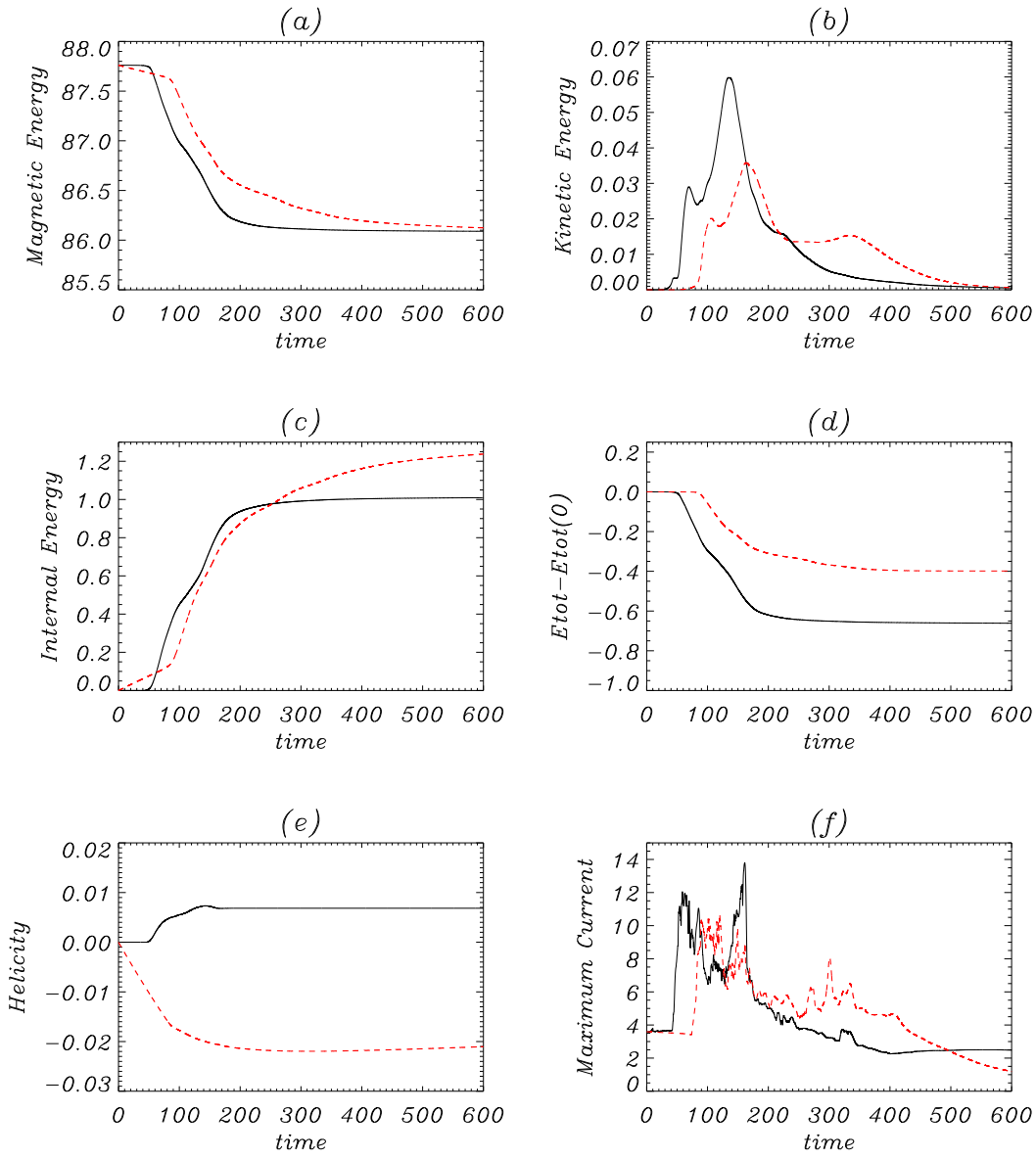

Figure 3.3: Plots of volume-integrated **(a)** magnetic energy, **(b)** kinetic energy, **(c)** internal energy, **(d)** total energy, **(e)** helicity and **(f)** maximum current for Case 1 and Case 2. Case 1 (*black*): with $\eta_b = 2 \times 10^{-4}$. Case 2 (*red*): with $\eta_b = 0$. The initial total energy of each case is 87.76. These simulations are both generated by low resolution simulations.

the evolution: the kink instability is delayed and the numerical dissipation is reduced and probably generates more heat.

Since we are more interested in whether an unstable thread is capable of triggering an instability in a nearby thread, we will keep $\eta_b = 0$ to remove the influence of background resistivity. In addition, we can increase the resolution in order to generate the more accurate results. Therefore,

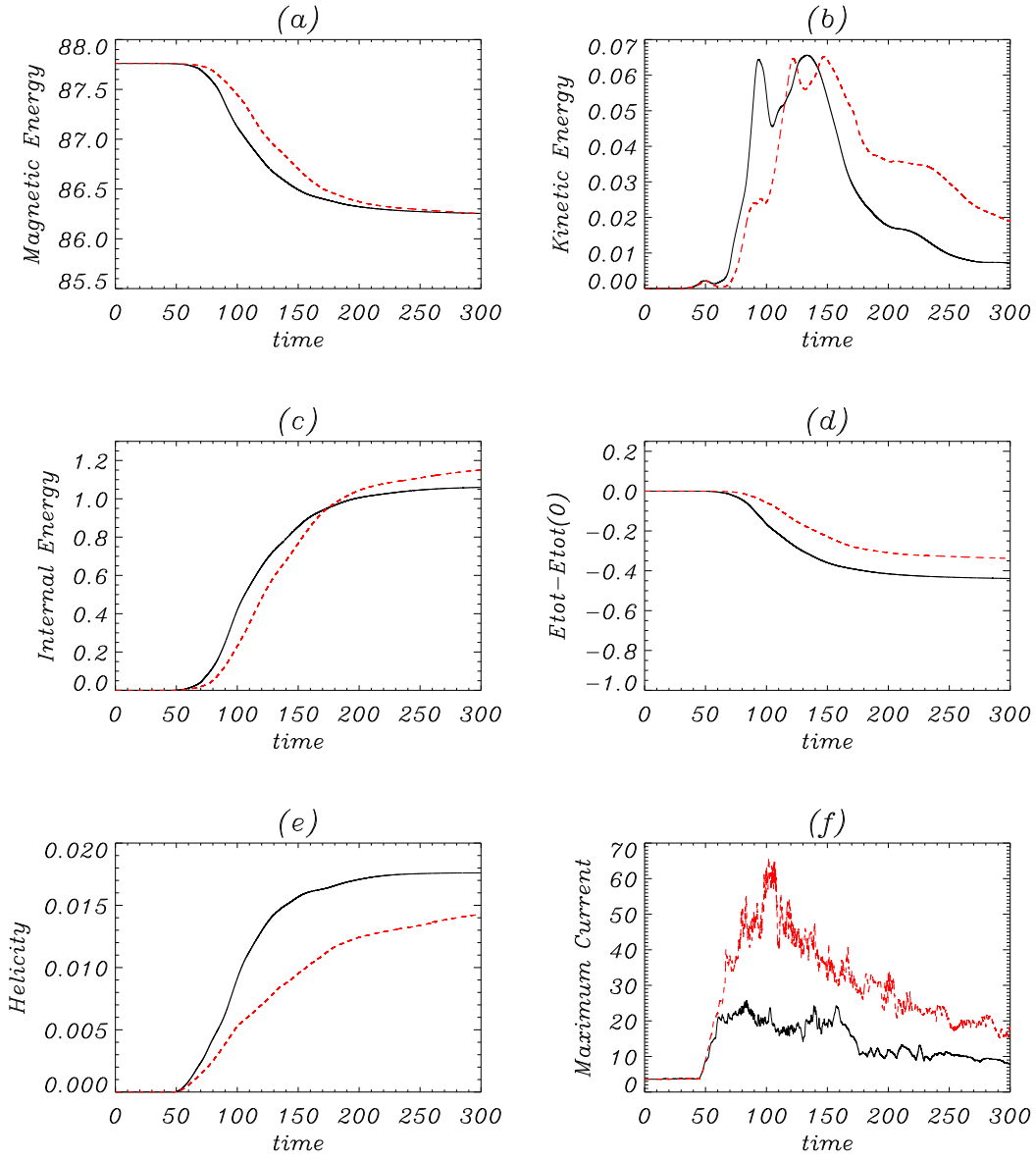

Figure 3.4: Plots of volume-integrated **(a)** magnetic energy, **(b)** kinetic energy, **(c)** internal energy, **(d)** total energy, **(e)** helicity and **(f)** maximum current for Case 3 and Case 4. Case 3 (*black*) is generated by a medium resolution and Case 4 (*red*) by a high resolution. The initial total energy of each case is 87.76.

Case 3 and Case 4 are introduced: in these cases, all the parameters are are idendical to Case 1, except the resolution is increased from $160^2 \times 320$ to $320^2 \times 640$. Figure 3.4 shows the changes in evolution, which we can summarise as follows. First, the rise time of the instability is delayed as the resolution is increased; second, the loss of magnetic energy has been reduced. By the end of the simulation, the magnetic energy has dropped by 1.505 and 1.507 in Case 3 and Case 4. It can also be seen that the gain of kinetic energy and internal energy has been increased, while the

loss of total energy has dropped to 0.438 and 0.337 in Case 3 and Case 4. These suggest that the higher resolution we use, the more accurate results we achieve. Subsequent results will be taken from simulation runs of medium resolution, as it will minimise the resources required to generate, store and analyse the data.

3.2.2 Instability conditions

We must also discuss how the individual magnetic threads behave when there is no initial perturbation imposed (Cases 5-7). The initial magnetic fields are analytically in equilibrium but, because of truncation errors introduced by the finite difference methods, the simulations will have a small but non-zero Lorentz force. The size of this force depends on the grid resolution. Therefore, these small truncation errors can eventually excite the kink instability in an unstable magnetic field.

We undertook targeted simulations to study the evolution of equilibrium threads that have no initial perturbations, to estimate the time for the instability to develop due to truncation errors. We use a variety of twist parameter values (i.e. values of λ). This will show us how the detailed time evolution depends on the nature of the twist profile; so for an avalanche event the magnetic thread must be destabilised before the time that the instability would develop due to truncation errors.

The threads will be located at the left-hand side of the computational domain (e.g. centred at $(x, y) = (-1, 0)$), with lengths $L_x = 8$, $L_y = 4$ and $L_z = 20$. The results presented below are taken from medium resolution simulations ($320 \times 160 \times 320$). This configuration allows us to add an unstable thread on the right-hand side and examine the avalanche effect. The normalised magnetic field strengths are $B_0 = 1.0$ (see Eq. 3.1 and Eq. 3.2). A summary of the simulations below.

The energy plots for Cases 5-7 are shown in Figures 3.5(a-c). The figures are as expected. In Case 5, since there is no initial perturbation included, the instability begins at a much later time compared to Case 3. The instability starts at around $t = 160$. At this point, the magnetic energy (and internal energy) plots show a shallower decrease (and increase) compared to Case 3. The kinetic energy rises slowly and takes longer to reach its maximum value at time about $t = 280$. The purple and red curves show that if we reduce the twist parameter to lower values (such as $\lambda = 1.6$ and 1.4), the threads remain in equilibrium over the entire simulation (the end time of each case is 300 Alfvén times).

To examine the stable and unstable profiles by the change of λ more closely, we have run a series of follow up simulations for Cases 5-7 (see Figures 3.5(d-f)), with a low resolution and a smaller computational domain (halving the size and resolution in the x-direction, i.e. $L_x = 4$). The blue curves show that the $\lambda = 1.6$ thread has an instability rise at $t = 380$. i.e. it is an unstable thread. Meanwhile, the $\lambda = 1.4$ thread remains in an equilibrium, which suggests that it is a stable thread.

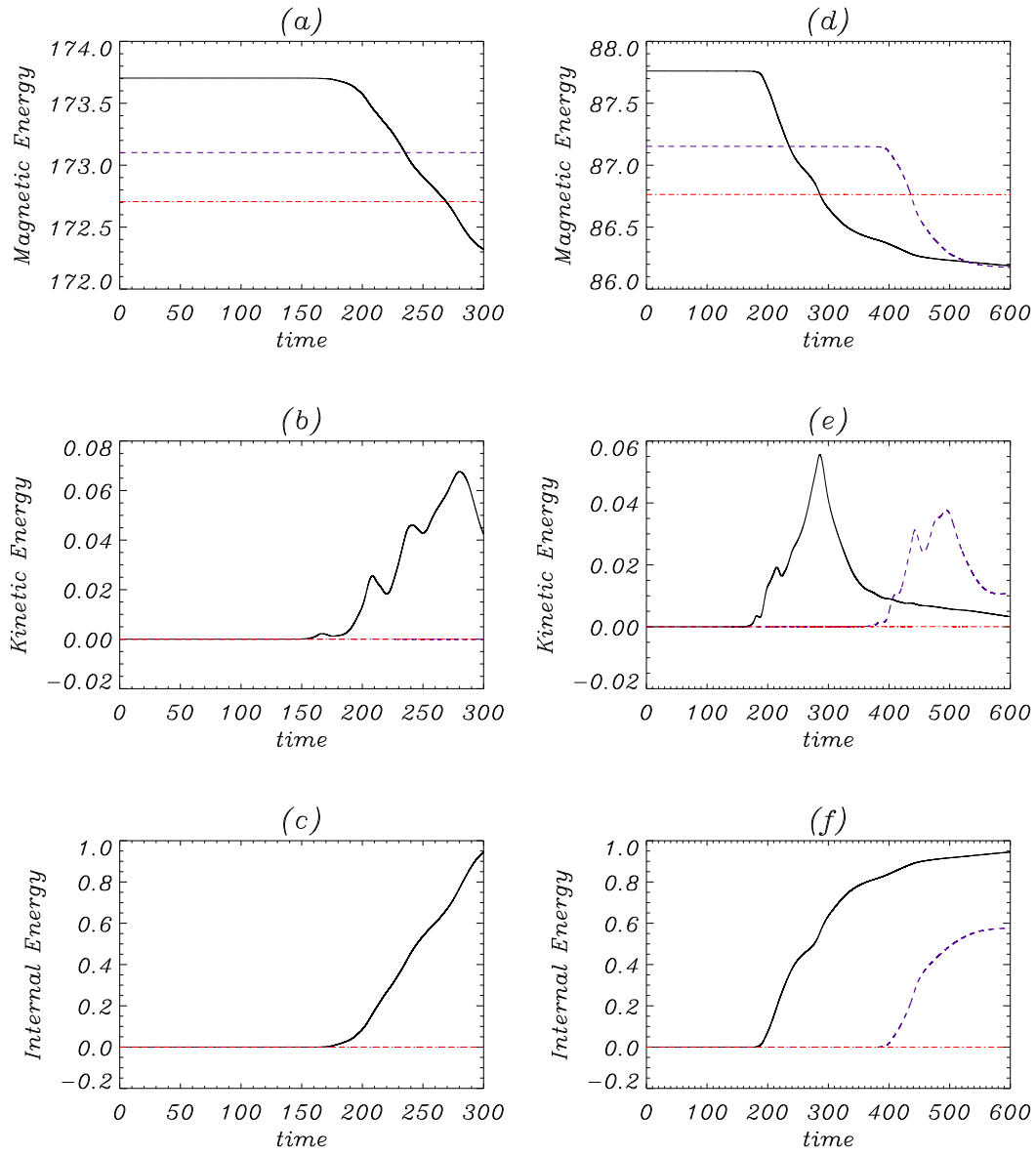

Figure 3.5: Plots of **(a)** magnetic energy, **(b)** kinetic energy and **(c)** internal energy over 300 Alfvén times for Case 5 (*black*), Case 6 (*purple*) and Case 7 (*red*). A set of follow-up simulations **(d)**-**(f)** have also been run with lower resolution $80^2 \times 160$ grid for 600 Alfvén times.

Recently, we have been able to confirm that the twist parameter $\lambda = 1.4$ does indeed give a stable magnetic field profile. Bareford et al. (2011) studying the instability thresholds with a series of α and λ profiles, confirm that $\lambda = 1.586$ is a critical value for marginal linear instability. Note that the reduction of resolution may vary the evolution time due to numerical errors; nevertheless we are using it as a reference time to indicate an avalanche effect. The magnetic thread will become unstable long before the times mentioned previously.

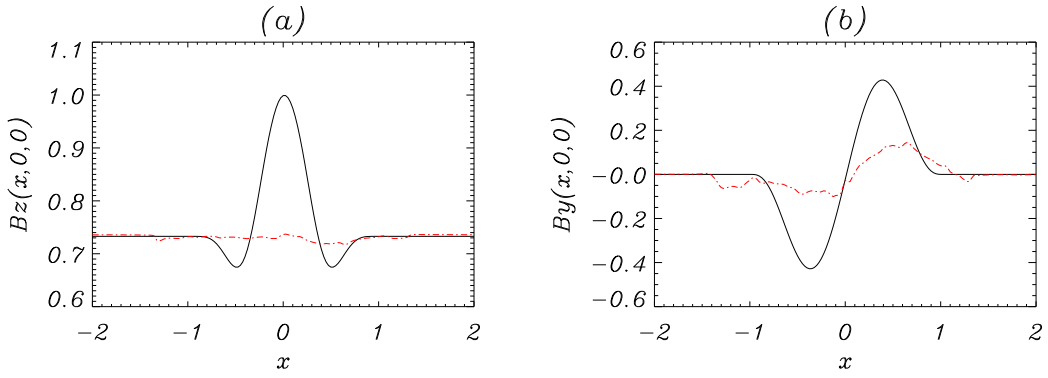

Figure 3.6: Case 3: The initial (*black*) and final (*red*) profiles of **(a)** $B_z(x,0,0)$ and **(b)** $B_y(x,0,0)$.

3.2.3 Phases of evolutions

Next, we begin to look into the details of the evolution in the threads in order to ascertain how the relaxation process takes place and relaxes the energy. Consider Figure 3.6(a,b), which shows the initial (*black*) and final (*red*) profiles of the magnetic field components of $B_z(x,0,0)$ and $B_y(x,0,0)$ for Case 3. The structure of the field components is defined by Eqs. 3.1 and 3.2. Initially, the maximum value in $B_z(x,0,0)$ is unity and is given by the normalised magnetic field strength for $B_0 = 1.0$ with a twist parameter $\lambda = 1.8$. The injection of an initial perturbation can be seen in Figure 3.2, which causes the unstable loop to develop a kink instability, triggers energy release and then relaxes the magnetic field towards a minimum energy state. The final stage of these profiles show evidence of relaxation (red curves). The magnetic field in $B_z(x,0,0)$ is nearly smoothed down to a uniform field, while the $B_y(x,0,0)$ has reduced to about $1/3$ of its maximum at $t = 0$. In addition to these, the $B_y(x,0,0)$ profile can also be an indication of magnetic reconnection. It can be seen that the structure of B_y has a negative magnitude from the left-hand side of the loop (e.g. $-1.5 < x < 0$) and a positive magnitude on the right-hand side of the loop (e.g. $0 < x < 1.5$) at all times. Such a signature can be a good source to confirm the occurance of magnetic reconnection in the multiple threads cases (see Figure. 3.15 for Cases 10 to 13 for comparison).

Figure 3.7 shows the evolution of Case 3 over 300 Alfvén times. By plotting the logarithm of the kinetic energy, any straight line segment could be indicative of a linear instability. The gradient line will be approximately *twice* the value of the growth rate (Browning et al., 2008). This is because the velocity is: $v \sim e^{\sigma t}$ at the initial development of the kink instability, while the plasma density (ρ) is still approximately constant. Consequently, the kinetic energy can be approximated by $W_{Ke} = \int \frac{1}{2}\rho v^2 \, dV \propto e^{2\sigma t}$.

Thus $\ln(W_{Ke}) = 2\sigma t +$constant. Initially, the kinetic energy decays slowly until around Alfvén

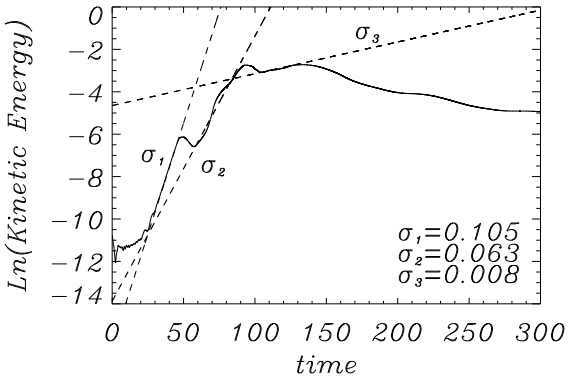

Figure 3.7: Case 3: The logarithm plot of kinetic energy together with the growth rate estimates.

time $t = 25$. Due to the development of an unstable mode, the kinetic energy rises rapidly once the linear instability has achieved a positive growth rate $\sigma_1 = 0.105$, followed by other non-linear growths with some small drops in between. Every time there is a rise in energy growth rate, there will also be current sheet formation and an increase in temperature.

3.2.4 Current sheet formations and field line evolutions

Consider now the current sheet formation of Case 3. The isosurface plots of the current density are shown in Figure 3.8. At time $t = 50$, there is a sign of growing instability and it develops into a kinked structure at $t = 70$. Figure 3.9 also shows the plasma velocity and current density in the mid-plane of the volume. The velocity components, v_x and v_y, are shown in terms of arrows. The magnitude of velocity components is proportional (and scaled by a factor of 4) to the size of the arrow heads and the length of arrows are also proportional to the magnitude of the horizontal velocity. At time $t = 50$, a kink instability creates a strong plasma flow to create an initial current sheet in the thread. From the centre of the cross section, the flow moves the plasma to the right-hand side near the edge of the thread which then returns to the left-hand side through the ends of current sheet. The occurrence of plasma flow and current sheet match the time at which the energy profiles begin to change. The current sheet becomes a stronger one at $t = 75$, with two

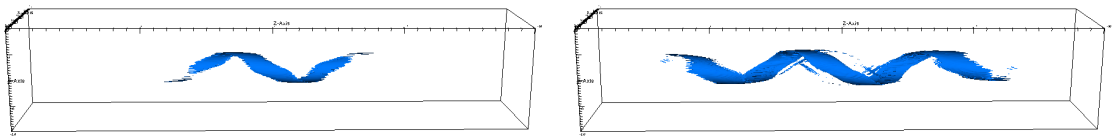

Figure 3.8: Case 3: The plots of isosurface of current density, $j = j_{crit}$, at time $t = 50$ (*left*) and $t = 70$ (*right*).

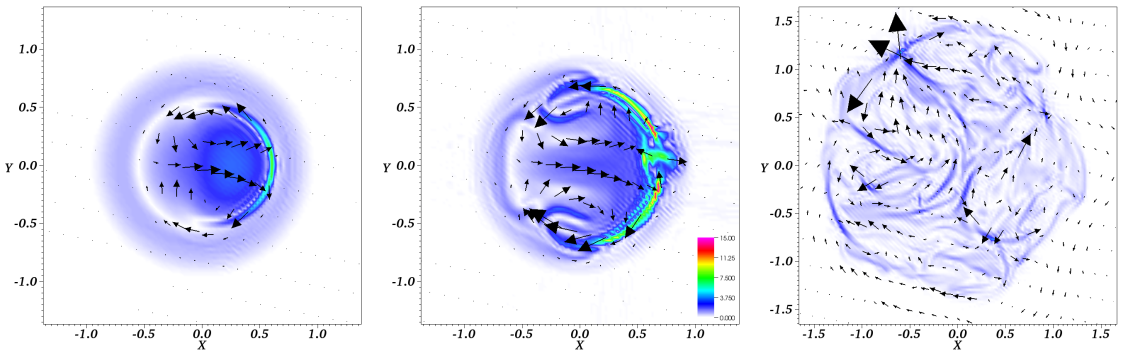

Figure 3.9: Case 3: Contour plots of the current density, $j(x, y, 0)$, at time: **(a)** $t = 50$ (*left*), **(b)** $t = 75$ (*middle*) and **(c)** $t = 300$ (*right*). The colour scale for the current density is from 0 (light purple) to 15 (*red*). The arrows also show the velocity components, v_x and v_y and the length of arrows is proportional to the magnitude of the horizontal velocity. They are scaled by a factor of 4, 8 and 16 times for (a)-(c) respectively.

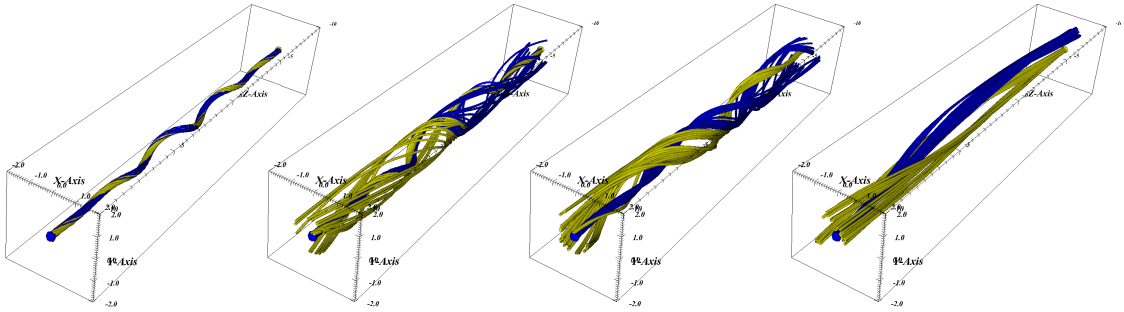

Figure 3.10: The field lines plots of Case 3 at time: **(a)** $t = 50$, **(b)** $t = 75$, **(c)** $t = 110$ and **(d)** $t = 300$, from the *left* to the *right*. The yellow field lines are drawn from $(x, y, z) = (0, 0, -10)$ while the blue field lines are drawn from $(x, y, z) = (0, 0, 10)$.

vortex patterns near the loop boundary. The plasma flow is seen to be reduced near the centre, however, it remains strong around the two vortex flows. By the end of the simulation, the size of the flows becomes even smaller and the current sheet has split into fragments of various strengths, filling and expanding the thread's cross section. This could be one indication of where magnetic reconnection occurs. To confirm this, we can track the evolution of the magnetic field lines. Field lines are tracked from the centre of each footpoint to the opposite side (see Figure 3.10). At time $t = 50$, a helical structure emerges as the kink instability is triggered. Throughout the simulation the current sheet expands and then splits into fragments; the field lines can also be seen as straightened, indicating that they are undergoing reconnection under the relaxation process. By the end of the simulation the field lines are untwisted and the energy in the field is approaching its lowest state. The current density and field lines have also expanded out to about one and a half times the loop radius, surrounded purely by the axial field.

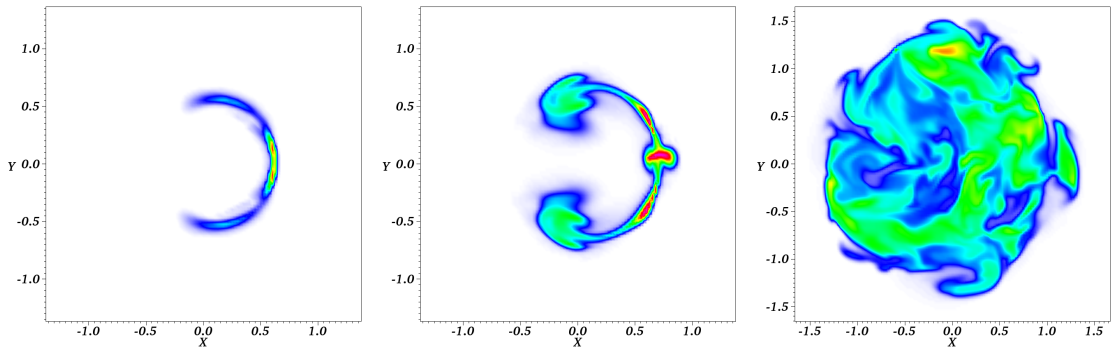

Figure 3.11: Case 3: The contour plots of the temperature $T(x, y, 0)$ at time: **(a)** $t = 50$ (*left*), **(b)** $t = 75$ (*middle*) and **(c)** $t = 300$ (*right*). The colour scale in (a) varies from 0 (*blue*) to 0.002 (*red*), and 0 (*blue*) to 0.04 (*red*) for (b) and (c).

3.2.5 Heating and temperature evolutions

For simplicity, the intital temperature in the computational volume is set to zero, which will then rise to various high values during the evolution. The temperature profile of Case 3 is shown in Figure 3.11 and Figure 3.12. At time $t = 50$, a small amount of heat is detected at the peak associated with where the new current sheet forms. This peak has a dimensionless temperature of 1.3×10^{-3}. At $t = 75$, the high temperature spreads outwards as the current sheet develops into the region where the vortex patterns are seen. When the kinetic energy reaches a maximum of $\tilde{T} = 0.065$ at $t = 130$, the maximum temperature reaches a value of about $\tilde{T} = 0.04$. The hot region eventually expands to about 1.5 times the initial radius and the overall temperature reduces to about $\tilde{T} = 0.005 - 0.02$.

The effective heating of the field can be estimated by the temperature, which is made dimensionless in the simulation. The dimensional temperature can be calculated by using a number of typical coronal values. We set the magnetic field strength to be $B_0 = 50$ G and the mass density is $\rho_0 = 10^{14} \times 1.6726 \times 10^{-27}$ kg m^{-3}. The dimensional temperature is therefore around $T = 7 - 28 \times 10^7$ K, where $T = \tilde{T} \frac{{B_0}^2}{\mu\rho_0} \frac{1}{R}$ K and $\tilde{T}$ is the dimensionless temperature obtained from *Lare3d*. These values are relatively high compared to those taken from observations; this is because we did not allow the thermal energy to leave the system. The inclusion of thermal conduction would bring down the temperature in the system by roughly a factor of 10 (Botha et al., 2011) and the inclusion of optically thin radiation may reduce the temperature even further, hence, the results should be comparable to observed values. In the next chapter, we will include thermal conduction and optically thin radiation in our simulations and discuss the importance of these features for nanoflare heating.

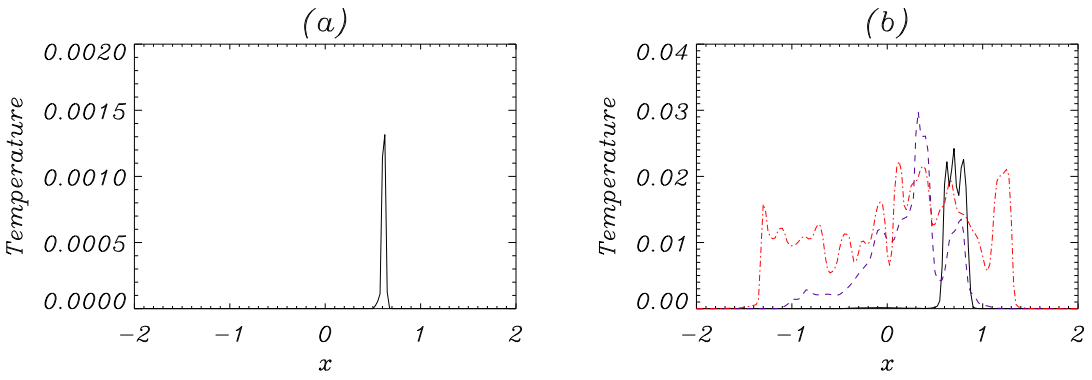

Figure 3.12: Case 3: The temperature plots of $T = (x, 0, 0)$ at times: **(a)** $t = 50$ and **(b)** $t = 75$ (*black*), $t = 130$ (*purple*) and $t = 300$ (*red*). The initial and background temperatures are set to 0.

3.3 Multiple loops

In the previous section, we have shown that nanoflares caused by kink instability can release sufficient amounts of energy to raise the temperature the solar corona. However, to maintain the multimillion-degree temperature, will require many heating sources that collectively provide continuous heating. Therefore we propose that nanoflare heating is valid because of a possible avalanche effect. In this section, the form of resistivity is as previously stated (see Section 3.2) and we will begin to examine the avalanche effects.

The aim of our studies in this section is to propose that an unstable loop can trigger an avalanche effect in nearby loops. An unstable equilibrium thread, which will initiate the avalanche, will always be located at the right-hand side of the system (centred at either $(x, y) = (2, 0)$ or $(x, y) = (0, 0)$). The twist parameter of the thread is $\lambda = 1.8$, a value beyond the ideal MHD marginal stability threshold. This thread is given an initial helical velocity perturbation (see Figure 3.13(a) and Hood et al. (2009)). Since the thread is unstable, the initial perturbation will eventually grow in amplitude, allowing the kink instability to develop reasonably quickly. The thread we are attempting to destabilise will be given different values of λ and will always be located in the left-hand side of the system, centred at $(x, y) = (-2, 0)$. This will allow us to investigate whether the unstable thread on the right can destabilise that on the left.

The results presented below are generated with a high resolution grid of $640 \times 320 \times 320$ in the x, y, z directions. The size of the computational domain is unchanged. In performing comparisons, we are confident that an avalanche effect in nanoflare heating is possible. This may help us to explain how heating is spread across a large coronal volume, thereby providing continuous heating to the solar corona. A summary of the various simulations is now given.

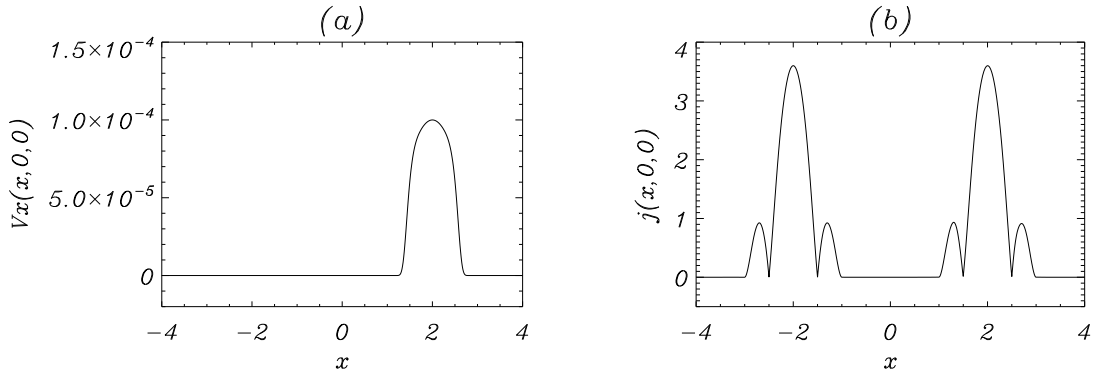

Figure 3.13: The initial profiles of **(a)** velocity and **(b)** magnitude of the current density at the mid-plane for Case 8.

Case 8: Two unstable equilibrium threads are located at $(x, y) = (2, 0)$ and $(x, y) = (-2, 0)$. Since the threads both have a radius of $r = 1$, the outer edges of the threads have a distance 2 units from each other. Both fields have a twist parameter of $\lambda = 1.8$. Only the right-hand thread is given an initial helical perturbation to the velocity. At the mid-plane $z = 0$, this perturbation is in the x direction and is shown in Figure 3.13. Note how the perturbation is centred on the axis of the right-hand thread and is zero outside it.

Case 9: This is the same as Case 8, except that the threads are now centred at $(x, y) = (0, 0)$ and $(x, y) = (-2, 0)$. Hence, the outer edges of the threads are touching each other at $(-1, 0)$.

Case 10: The axes of the two threads are at the same locations as in Case 8 but the left-hand thread has a reduced twist parameter of $\lambda = 1.6$. With this value of the twist parameter this thread would be stable on its own over a simulation lasting only 300 Alfvén times (see Case 6).

Case 11: This is the same as Case 10 but with the threads centred at $(x, y) = (0, 0)$ and $(x, y) = (-2, 0)$.

Case 12: This is the same as Case 8, except that the thread centred at $(x, y) = (0, 0)$ has a reduced twist parameter of $\lambda = 1.4$. The value of this twist parameter means this thread is stable when isolated from other threads (see Case 7).

Case 13: This is the same as Case 12 but with the threads centred at $(x, y) = (0, 0)$ and $(x, y) = (-2, 0)$.

When $\lambda_0 = 1.8$, we select $B_0 = 1.0$ (see Eq. 3.1 and Eq. 3.2). As discussed previously, the background magnetic field (at $r > 1$) must be the same everywhere and the magnetic field strength for a different λ thread must be recalculated so that continuity holds. For example, when $\lambda_1 = 1.6$, $B_1 = \sqrt{\frac{1-1.8^2/7}{1-1.6^2/7}} = 0.92$. Similarly, if $\lambda_2 = 1.4$, $B_2 = \sqrt{\frac{1-1.8^2/7}{1-1.4^2/7}} = 0.864$.

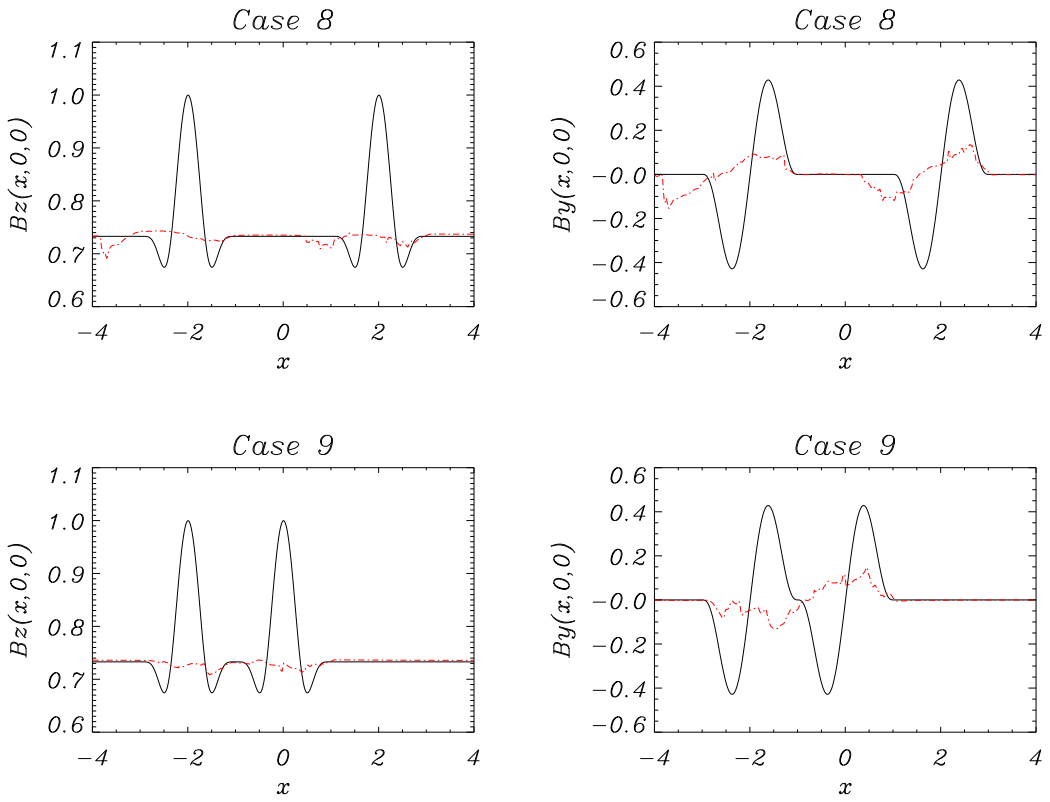

Figure 3.14: The initial (*black*) and final (*red*) profiles of $B_z(x,0,0)$ and $B_y(x,0,0)$ for Case 8 and Case 9.

3.3.1 Initial and final states

Figures 3.14 to 3.15 show the initial $(t = 0)$ and final $(t = 300)$ radial profiles of $B_z(x,0,0)$ and $B_y(x,0,0)$ for all cases. For Case 8, the magnetic field strength of both threads are initially the same, as they share the same twist parameter of $\lambda = 1.8$. A similar form can be observed in Figure 3.13(b), which shows the corresponding current density profiles. However, due to the injection of an initial perturbation to the right-hand side thread, the velocity profiles will not be identical in each thread (see Figure 3.13(a)). The given perturbation will help the unstable thread on the right to develop a kink instability at an earlier stage, which will trigger energy release and then relax toward a minimum energy state. By the end of the simulation, both threads have evolved to essentially the same final state, with an almost uniform axial field component, B_z and a significantly reduced twist in the field lines, as shown by the reduced values of B_y. However, the precise temporal evolution is needed to determine whether the left-hand thread is actually driven unstable by the kink instability in the right-hand thread or not. Note that $B_y(x,0,0)$ is clearly zero between the two threads. In Case 9, the two threads are placed next to each other with a result very similar to Case 8; both threads relaxing towards a more potential state. In this case, however,

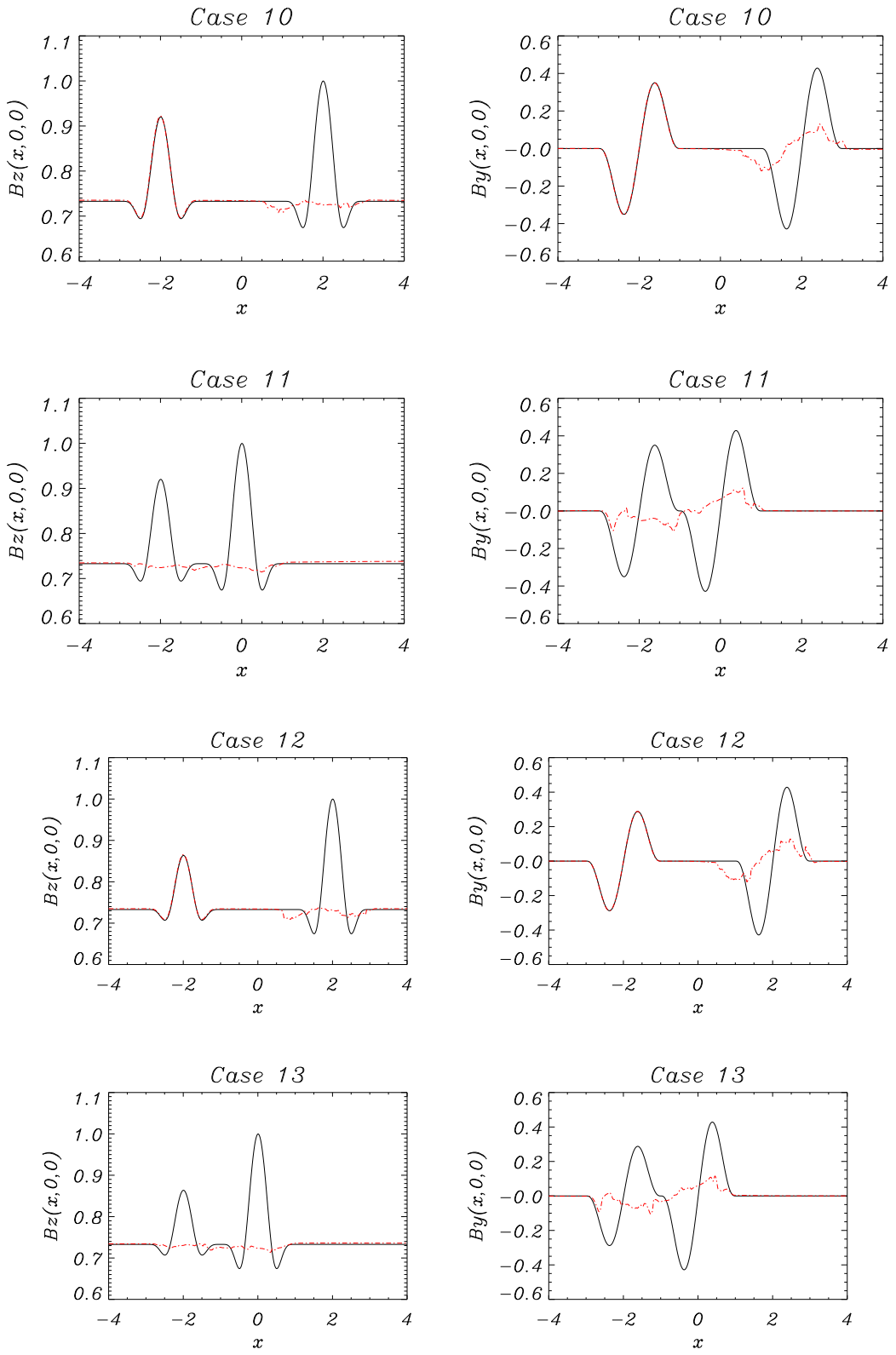

Figure 3.15: The magnetic field plots of $B_z(x,0,0)$ and $B_y(x,0,0)$ for the initial (*black*) and final (*red*) profiles of Case 10 to Case 13.

it appears that the threads have been combined into one single large loop, as shown by the B_y profile. The magnitude of B_y is negative for $x < -1$ and is positive for $x > -1$, hence, the twist is around a common axis.

Cases 10 and 12 result in only the unstable right-hand threads being relaxed, while the left-hand threads remain unchanged from their initial states (see Figure 3.15). However, when these threads are brought next to each other (as in Cases 11 and 13), a difference can be seen. Both of the B_z and B_y profiles show clear evidence of relaxation in the left-hand thread, which is also combined with the right-hand thread into one single magnetic structure at the end of the simulations.

The first impression to be gained from the figures is: when the two magnetic threads are sufficiently close together, the instability in the right-hand thread is also triggered in the relaxation event of the left-hand thread and thus the two threads system of Cases 9, 11 and 13 evolve into a single-loop like system. We will attempt to examine the energy and temperature evolution, current sheet formation and field lines disturbation to confirm this finding.

3.3.2 Integrated energies as function of time

Before looking at the the volume-integrated functions, it is wiser to first study the growth rates of energy in the fields, as they illustrate the dynamic progresses. The linear growth rates can be estimated from the logarithm of kinetic energy profiles (see Browning et al., 2008).

In Case 8, the kinetic energy decays slowly until around Alfvén time $t = 30$ (see Figure 3.16). Due to the development of an unstable mode, the kinetic energy rises rapidly with a linear growth rate of $\sigma_1 = 0.081$. It then increases again with a non-linear growth rate of $\sigma_2 = 0.2$ until $t = 80$ and is followed by a slow decay. There is also a small rise of $\sigma_3 = 0.027$ between time $t = 95$

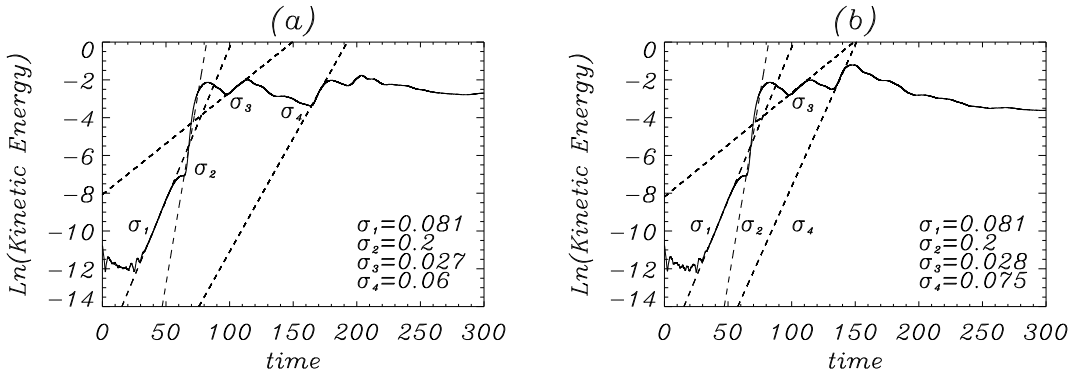

Figure 3.16: The log plots of kinetic energy as a function of time and the estimate growth rates for **(a)** Case 8 and **(b)** Case 9.

	Case 8	Case 9	Case 10	Case 11	Case 12	Case 13
σ_1	0.81	0.81	0.81	0.81	0.81	0.81
σ_2	0.2	0.2	0.2	0.2	0.2	0.2
σ_3	0.027	0.028	0.027	0.035	0.028	0.027
σ_4	0.06	0.075	-	0.06	-	0.04

Table 3.1: The table of the growth rates in kinetic energy for Cases 8-13.

and $t = 105$. When the loops are put together (Case 9), the growth rate of kinetic energy has a slightly larger value of $\sigma_4 = 0.075$ between time $t = 130$ to 150 and is followed by a steeper decay towards the end of the simulation. The value of the growth rates from $t = 160$ onwards are slightly higher and occur earlier than for the separated case. This indicates that the energy release from an unstable loop can influence its neighbouring thread and result in an additional rapid release of energy.

A summary of the growth rates for Cases 8 to 13 is shown in Table. 3.1, it indicates that when the magnetic threads are moved closer together, the growth rates will rise in either σ_3 or σ_4.

3.3.2.1 Evolution of magnetic and internal energies

We begin to discuss the evolution of each form of energy by studying the volume-integrated magnetic, internal and kinetic energies as a function of time. Figures 3.17 and 3.18 show the temporal evolution until the end of the simulations at $t = 300$.

The left-hand column of Figure 3.17 shows the change of volume-integrated magnetic energy, $W_B = \int \frac{B^2}{2\mu_0} dV$, for Cases 8-13. In Case 8, the magnetic energy remains at its initial value until $t = 65$, followed by a slow decrease corresponding to a release of magnetic energy. The decrease becomes significantly slower between $t = 125$ and $t = 165$. As discussed by Taylor (1974, 1986), this initial rapid decrease followed by a much slower one is an indication that the magnetic field is relaxing towards a minimum state. This behaviour repeats once from $t = 164$ onwards, as the instability of the second thread is triggered. The total magnetic energy has dropped by 3.031 by the end of the simulation. The red dashed curve in the same plot shows the magnetic energy profile of Case 9. It follows the same initial evolution as in Case 8. However, the second phase of magnetic energy release occurs slightly earlier, at time $t = 135$, as the loops are now placed right next to each other. Our experiments show that the closer together the threads are the sooner the second instability is triggered. By the end of the simulation, the magnetic energy has dropped by 3.069 and slightly more energy is released than in Case 8. The vertical dashed lines indicate the times when a new current sheet is about to form (see Section 3.3.3). Note that the overall magnetic energy drop is almost identical for Cases 8 and 9, which confirms the relaxation processes had taken place and were very close to potential.

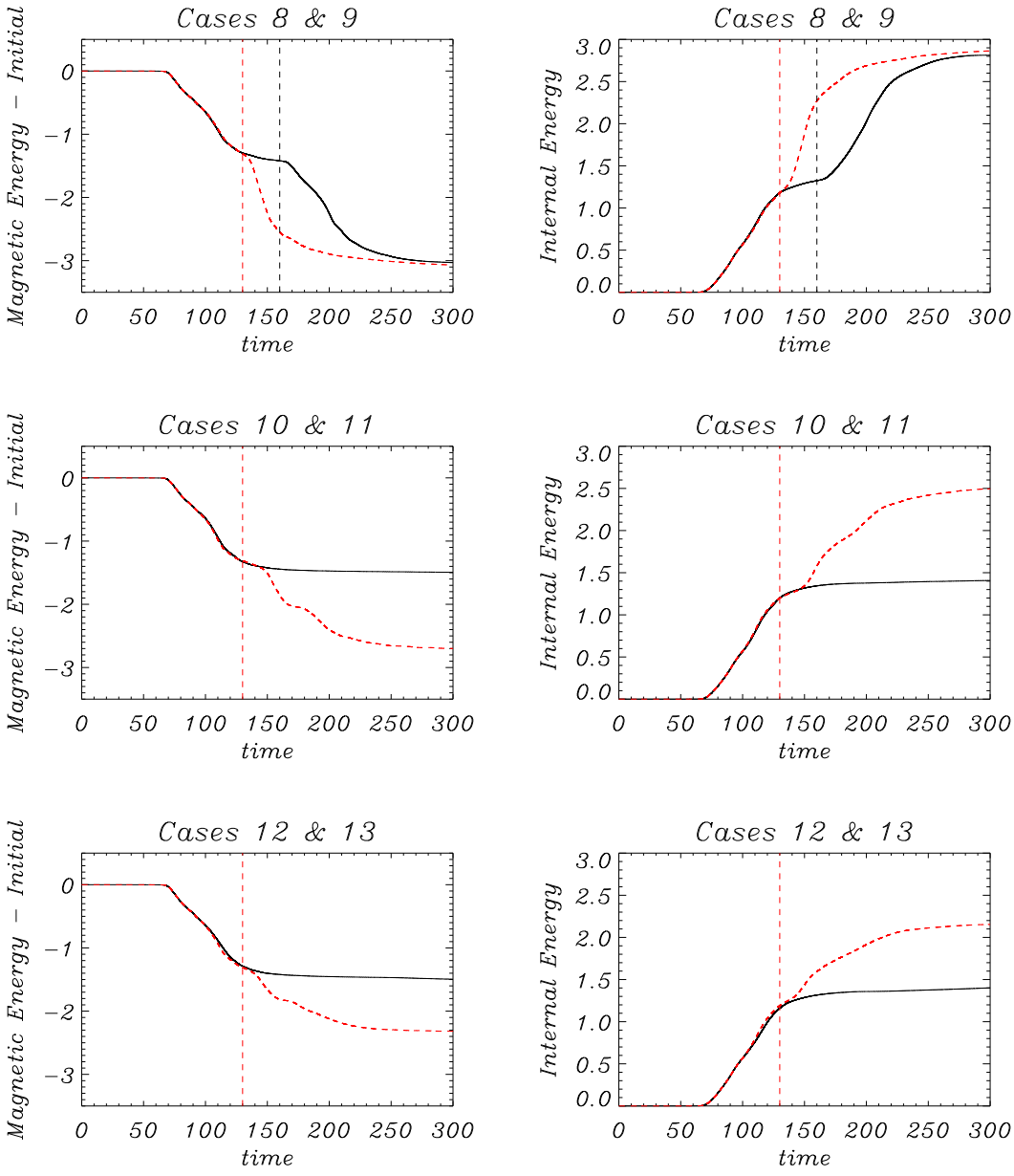

Figure 3.17: The left column shows the total magnetic energy minus the initial value as a function of time and the right column shows the temporal evolution of the total internal energy. The top row shows the results for Case 8 (*black solid* curve) and Case 9 (*red dashed* curve), while the middle shows the results for Case 10 (*black solid* curve) and Case 11 (*red dashed* curve), the bottom row shows the results for Case 12 (*black solid* curve) and Case 13 (*red dashed* curve). The total magnetic energy in the volume at time $t = 0$ is 175.52 for Cases 8 and 9, 174.91 for Cases 10 and 11 and 174.52 for Cases 12 and 13.

Recall that $\lambda = 1.6$ is also an unstable twist profile, in which an instability triggered by truncation errors will occur at about $t = 380$ or later if there is not an initial perturbation injected to the field. In Cases 10 and 11, we introduce the $\lambda = 1.6$ profile to the thread on the left. In Case 10, while the threads are placed a distance apart, as in Case 8, the magnetic energy remains unchanged until an instability starts (at $t = 65$). It then begins to decrease slowly in a manner similar to Case 8. However, the decline does not have a second phase. The black curve in for Case 10 shows the decay of magnetic energy is gentled from $t = 130$ onwards, as the loop approaches a minimum energy state. The overall magnetic energy has dropped by 1.493 by the end of the simulation, which is about 49.26% of the result for Case 8. It indicates that only the right-hand side loops become unstable.

A higher energy release can be observed if these loops are moved closer together. The red curve for Case 11 shows the variation of the energies. Between time $t = 130$ and 140, the magnetic energy is levelling off at the same value and at time $t = 141$, the magnetic energy decreases again as the second thread is destabilised. This did not happen for Case 10. By the end of the simulation, the magnetic energy has dropped by 2.698. This shows that a marginally unstable equilibrium thread can be destabilised at a significantly earlier time by this avalanche effect. Similar variations can also be observed in Cases 12 and 13. A stable twist profile ($\lambda = 1.4$) is also introduced to the left-hand threads in Cases 12 and 13. Their evolution of magnetic energies act similarly to Cases 10 and 11 respectively, while their final magnetic energy has dropped by 1.495 only in Case 12 (when the threads are separated) and by 2.317 in Case 13 (when the threads are touching). This result is very important as it shows that a stable field can be destabilised by a neighbouring unstable one. However, in the current situation we do not have the computing resources to determine the conditions for that to occur.

When the magnetic energy is released, the volume-integrated internal energy, $W_{Int} = \int \frac{P}{\gamma - 1}\, dV$, shows a similar size of increase at the same times and hence the majority of the released magnetic energy is transferred into a rise in the internal energy of the plasma (see the right-hand column of Figure 3.17). The internal energy in Case 8 shows a similar pattern to the magnetic energy variation: it rises slowly at $t = 65$ and then rises again at $t = 164$, before it slowly levels off at a value of 2.813. In Case 9, the internal energy also follows the path of Case 8 initially. It rises from $t = 65$ and $t = 130$, before it relaxes towards a stable state. By the end of Case 9, when the threads are moved to touch each other, the internal energy has increased by 2.864, slightly higher than Case 8.

The internal energy curve of Case 10 is also a mirror image of its magnetic energy curve. It rises at $t = 65$ and begins to level off from $t = 130$ onwards. By the end of the simulation, the internal energy has only increased by 1.407, 50% of the value in Case 8. If the threads are moved together (in Case 11), the internal energy will repeat the rise again since time $t = 141$. By the end of the simulation, the red curve for Casee 11 shows that internal energy has increased by 2.494,

which is 88.7% of the value in Case 8 and 177.3% of the value in Case 10. Similar evolutions of Cases 10 and 11 can be also seen in Cases 12 and 13, when a stable twist profile of $\lambda = 1.4$ is introduced to the left-hand side loop. The internal energy of Case 12 has only increased by 1.401 (49.8% of the value in Case 8), while the internal energy of Case 13 has increased by 2.154 (76.6% of the value in Case 8 and 206.9% of the value in Case 12).

The most interesting result is that there will be a quicker magnetic energy release in the left-hand side threads if these threads are moved closer together, as the avalanche events in Cases 9, 11 and 13.

3.3.2.2 Evolution of kinetic energy

Due to energy conservation, the loss of magnetic energy has to be converted into other forms of energy, such as kinetic energy and internal energy. Therefore, similar variations can also be observed in corresponding figures. The magnitude of the volume-integrated kinetic energy,

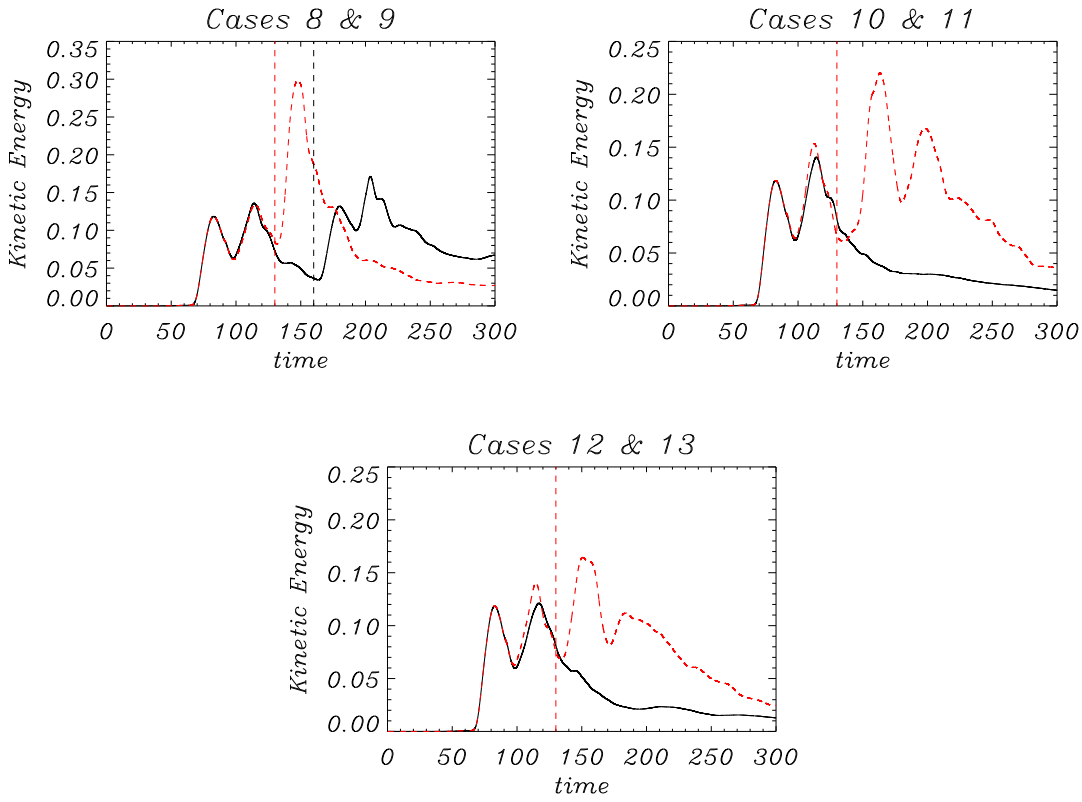

Figure 3.18: The temporal evolution of the total kinetic energy for **(a)** Case 8 (*black solid* curve) and Case 9 (*red dashed* curve), **(b)** Case 10 (*black solid* curve) and Case 11 (red dashed curve) and **(c)** Case 12 (*black solid* curve) and Case 13 (*red dashed* curve).

$W_{Ke} = \int \frac{1}{2}\rho v^2 \, dV$, is significantly smaller than the magnitude of the volume-integrated internal energy and hence most of the magnetic energy released appears as heat and not motion. However, the small changes in the kinetic energy are easier to detect and rapid changes in kinetic energy are clear indicators of dynamical events. In all six cases in this section, the kinetic energy only begins to rise rapidly at about $t = 65$ (see Figure 3.18) as the unstable right-hand thread is excited. It then peaks twice, reaching a maximum of 0.136 around $t = 115$, followed by a slow decay. Without the occurrence of a second thread, this slow decay would continue as the magnetic field relaxes towards a stable, static equilibrium.

For Case 8, the kinetic energy begins to rise again around $t = 165$, as the second thread is driven unstable. It also peaks twice and reaches a maximum of 0.171 at $t = 200$, before it starts to decay towards a minimum energy state. This double-peaked feature is directly related to the evolution of current sheet formation, which we will discuss in the next section. Case 9, however, shows a much earlier rapid rise at time $t = 132$, followed by a fast decay around $t = 150$ after it reaches a maximum value of 0.298. By the end of the simulations, there is more kinetic energy left in Case 8, suggesting that this configuration still has to reach its final Taylor relaxed state.

When the left-hand thread has a stable twist profile, the kinetic energy behaves initially as expected, in response to the unstable right-hand thread. The black curves for Cases 10 and 12 in Figure 3.18(b,c) peak only twice, followed by a gentle decay without any further increase. Clearly only the energy in the one unstable thread has been released. However, in Cases 11 and 13, when the threads are placed next to each other, the kinetic energy shows a dramatic increase as the second stable thread is destabilised by the disturbances of the first unstable thread.

3.3.2.3 Energy evolution of each thread

We calculate the temporal evolution of the volume integrated energies in the left-hand and right-hand halves of the plasma volume separately, as this will help us to understand the detailed evolution of the individual threads. In Case 8, the right-hand side is excited by an initial perturbation, while the left-hand side is only destabilised by the instability in the right-hand side. Figure 3.19 shows the magnetic and kinetic energy as functions of time in each volume. The red curves show the energy profiles of the right-hand side volume, the blue curves the left-hand side volume and the black curves the sum of the two curves.

The black curve (Figure 3.19, *top left*) for Case 8 shows the two stage release of magnetic energy as discussed previously. The red dashed curve shows that the right-hand side is actually losing more magnetic energy than the total value, between times $t = 65$ and $t = 180$. Since the majority of this released magnetic energy transfers into internal energy, there is an increase in the pressure in the right-hand volume. This creates an expansion in the thread and pushes the plasma

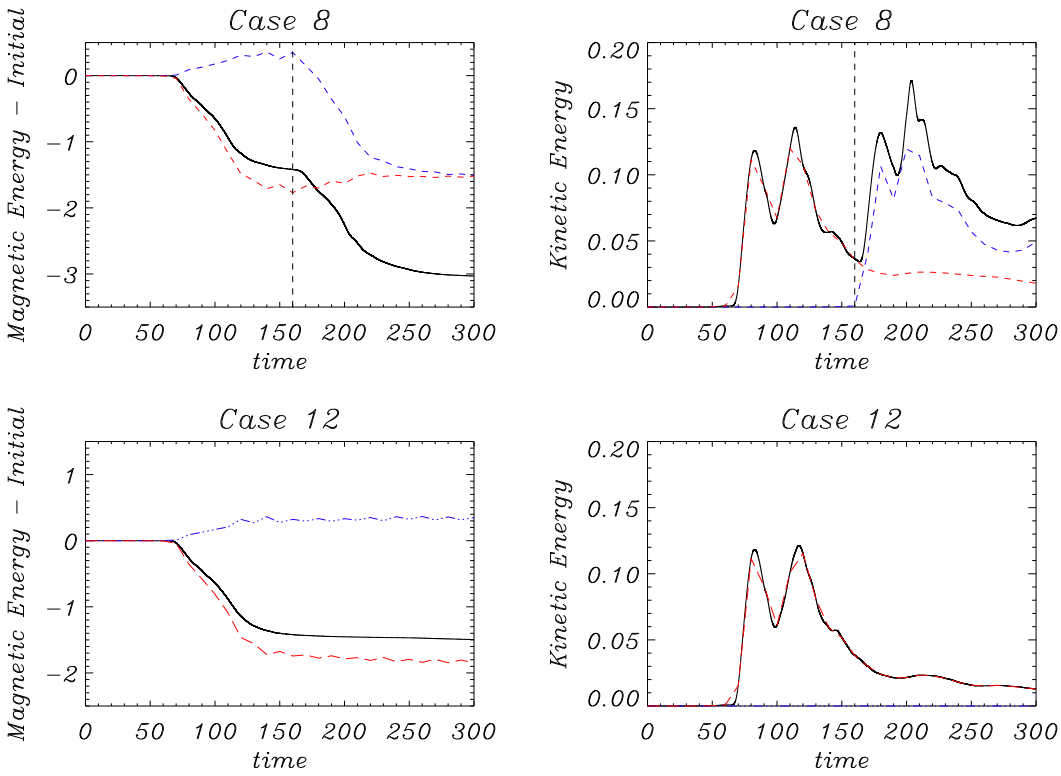

Figure 3.19: The temporal evolution of the volume integrated energy plots of Case 8 and Case 12. The magnetic energy at time $t = 0$ is 175.52 for Case 8 and 174.52 for Case 12. The black curves show the energy profiles as in Figure 3.17, while the red curves show the energy profiles on the left-hand side of the domain and the blue curves for the left-hand side.

into the left-hand volume, compressing the magnetic field and increasing the magnetic energy there. This is shown in the blue triple dotted-dashed curve. This increase in magnetic energy in the left-hand volume starts to slow as the amount of energy released in the right-hand volume is reduced. However, once the kink instability is triggered in the left-hand volume the magnetic energy is again reduced. The comparable behaviour can also been seen in the the kinetic energy plot of for Case 8 (see Figure 3.19, *top right*).

When we consider the time evolution of the magnetic energy for Case 12 (Figure 3.19, *bottom left*), we can see the increase in magnetic energy in the left-hand volume agin as the energy in the right-hand volume decreases. However, in this case, there is no secondary instability and the magnetic energy in the left-hand volume remains enhanced. The kinetic energy curves (Figure 3.19, *bottom right*) can also confirm that there is no dynamical development in the left-hand volume as the volume-integrated kinetic energy (*black* curve) and right-hand-volume-integrated kinetic energy (*red* curve) lie on top of each other.

It is also possible to calculate the initial energy contained in each thread. The volume-integrated

magnetic energy in cylindrical coordinates is given by

$$W_B = \int_r \int_\theta \int_z \frac{B^2}{2\mu_0} r dr d\theta dz.$$

Substituting Eq. (3.1) into the integral gives

$$\begin{aligned} W_B &= \int_0^{2\pi} d\theta \int_{-10}^{10} dz \int_0^1 \frac{B_\theta^2 + B_z^2}{2} r dr \\ &= 10\pi B_0^2 \left(1 - \frac{\lambda^2}{8}\right). \end{aligned}$$

Therefore, if $\lambda_0 = 1.8$ and $B_0 = 1$, the magnetic energy contained in the thread is 16.68. Similarly, for $\lambda_1 = 1.6$ and $B_1 = 0.92$, the energy contained in the thread is 18.08. Finally, if $\lambda_2 = 1.4$ and $B_2 = 0.86$, the energy contained is 17.67.

3.3.3 Current and magnetic field line evolution

We start by considering the temporal evolution of the magnitude of the current density in Cases 8 and 9 before discussing the structure of the field lines. Figure 3.20 shows the cross section of current density magnitude of Case 8 (*left*) and Case 9 (*right*). Due to the initial perturbation, a kink instability creates an initial current sheet (red colour in the contour plot) within the right-hand side thread at time $t = 60$. It matches the time at which the energy profiles begin to change for both cases. The current sheet becomes stronger at $t = 80$ for both Cases 8 and 9, with two observable vortex patterns near the thread boundary. This suggests that magnetic reconnection is likely to occur and will be discussed below. The current within the right-hand thread begins to fragment and many small-scale current structures are seen at a later time. This has been discussed by various authors (e.g. Hood et al., 2009) and seems to be a key part of the Taylor relaxation process.

The second thread is then destabilised by the first thread and this is seen in the current density plots as the formation of a second current sheet. For Case 8 this occurs at $t = 160$ and for Case 9 at $t = 130$. By the end of each simulation, $t = 300$, the current has fragmented and spread across in each thread. For Case 8, the regions of small scale current remain distinct and are separated by a region of essentially potential magnetic field. However, in Case 9, there is a clear indication that the two threads have combined to form a single larger structure in Figure 3.20 (*bottom right*).

We then track the evolution of the magnetic field lines for Case 8. The field lines around the centre of each thread are traced from one photospheric end to the opposite as shown in Figure 3.21 for Case 8. These are coloured red and yellow for the left-hand thread and blue and green for the right-hand thread. If there is no magnetic reconnection, then the red/yellow and blue/green field

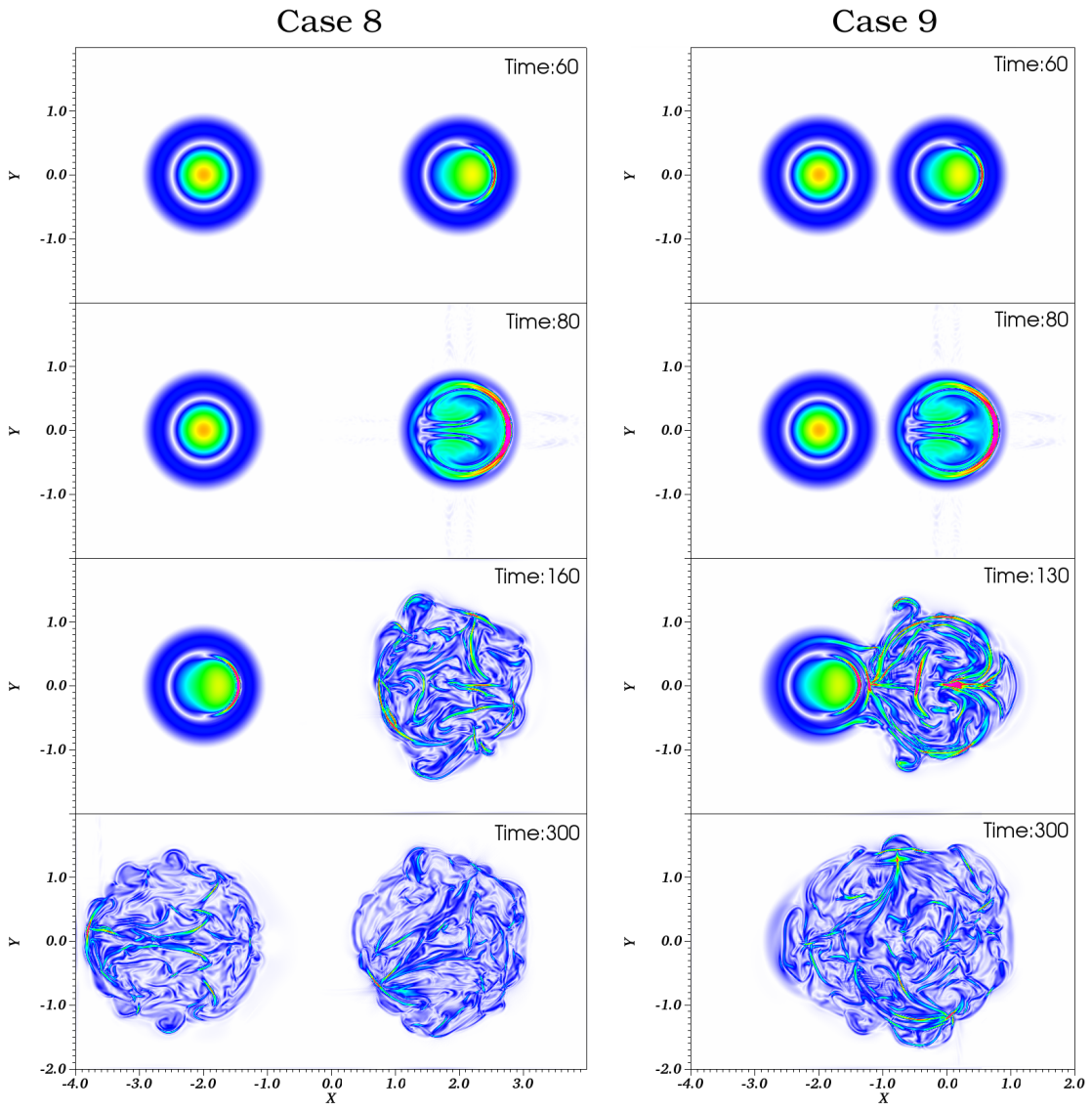

Figure 3.20: The contour plots of the magnitude of current density, $j(x, y, 0)$, as a function of (x, y) and $z = 0$ at times. The figures on the left and right are for Cases 8 and 9 respectively. The colour scale for the current density goes from 0 (*white*) to 5 (*red*).

lines will lie on top of each other. If there is a reconnection, then the ends of the field lines will not locate at the original footpoints. At time $t = 60$, a helical structure can be seen on the right-hand side thread, as the kink instability is excited. The field lines are seen to unwind or straighten. Reconnection has occurred in Figure 3.21(b) at $t = 80$. In particular, the green field lines start from the thread axis at the far end of the right-hand thread. However, these field lines completely encircle the thread axis at the near end. The green and blue field lines do not follow the same paths indicates that magnetic reconnection has occurred. Once the second instability is triggered, the left-hand thread follows a similar evolution. By the end of the simulation, the field lines are

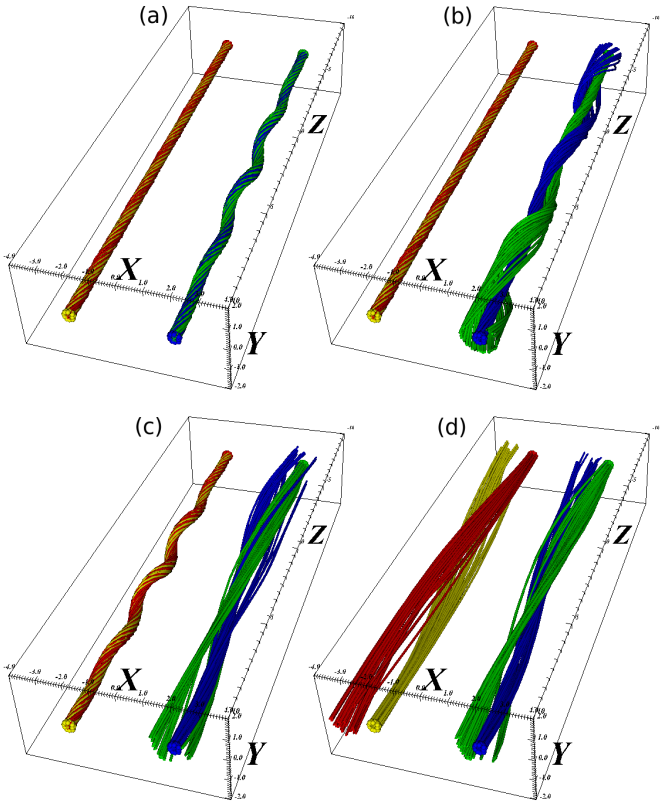

Figure 3.21: Case 8: the field line plots at time: **(a)** $t = 60$ (*top left*), **(b)** $t = 80$ (*top right*), **(c)** $t = 160$ (*bottom left*) and **(d)** $t = 300$ (*bottom right*). The yellow and red field lines are drawn from $(x, y, z) = (-2, 0, 10)$ and $(x, y, z) = (-2, 0, -10)$ while the blue and green field lines are drawn from $(x, y, z) = (2, 0, 10)$ and $(x, y, z) = (2, 0, -10)$.

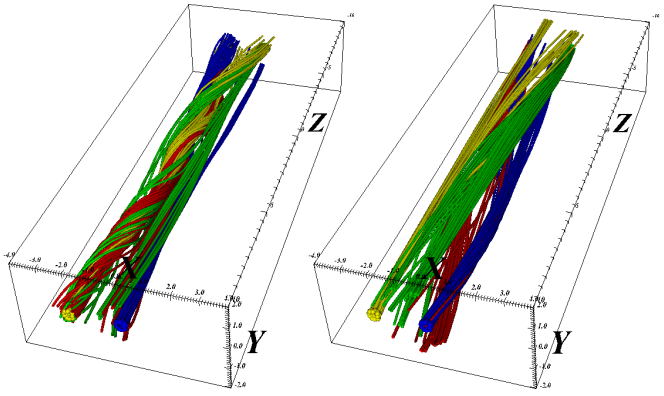

Figure 3.22: The field line plots for Case 9 at time: $t = 150$ (*left*) and $t = 300$ (*right*). The yellow and red field lines are drawn from $(x, y, z) = (-2, 0, 10)$ and $(x, y, z) = (-2, 0, -10)$ while the blue and green field lines are drawn from $(x, y, z) = (0, 0, 10)$ and $(x, y, z) = (0, 0, -10)$.

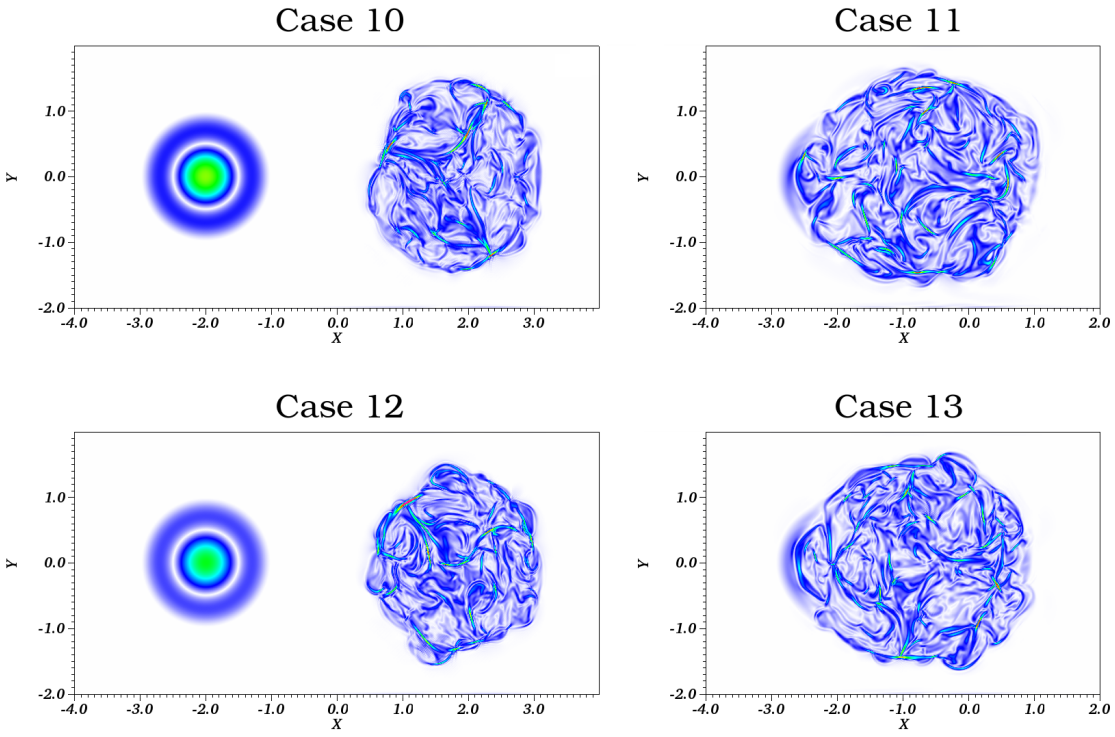

Figure 3.23: $t = 300$: The contour plots of current density, $j(x, y, 0)$, for Cases 10-13 with colour scale defined from 0 (white) to 5 (*red*).

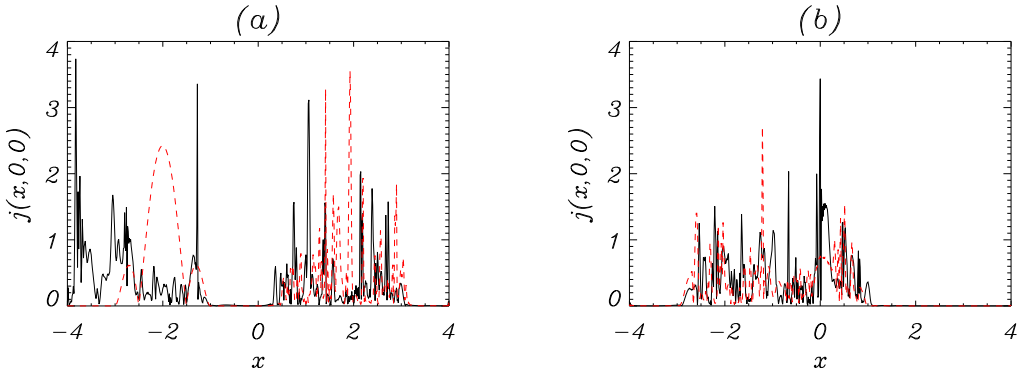

Figure 3.24: $t = 300$: plots of the magnitude of current density, *j(x,0,0)*, for four cases. The black and red curves in **(a)** represent Cases 8 and 12, and **(b)** Cases 9 and 13.

nearly untwisted and the two threads remain completely distinct.

Figure 3.22 shows the field line plots for Case 9 at time $t = 150$ (*left*) and $t = 300$ (*right*). What is clearly shown is that various coloured field lines are now wrapping around each other, forming one weakly twisted magnetic loop. It will be interesting to see if future simulations can

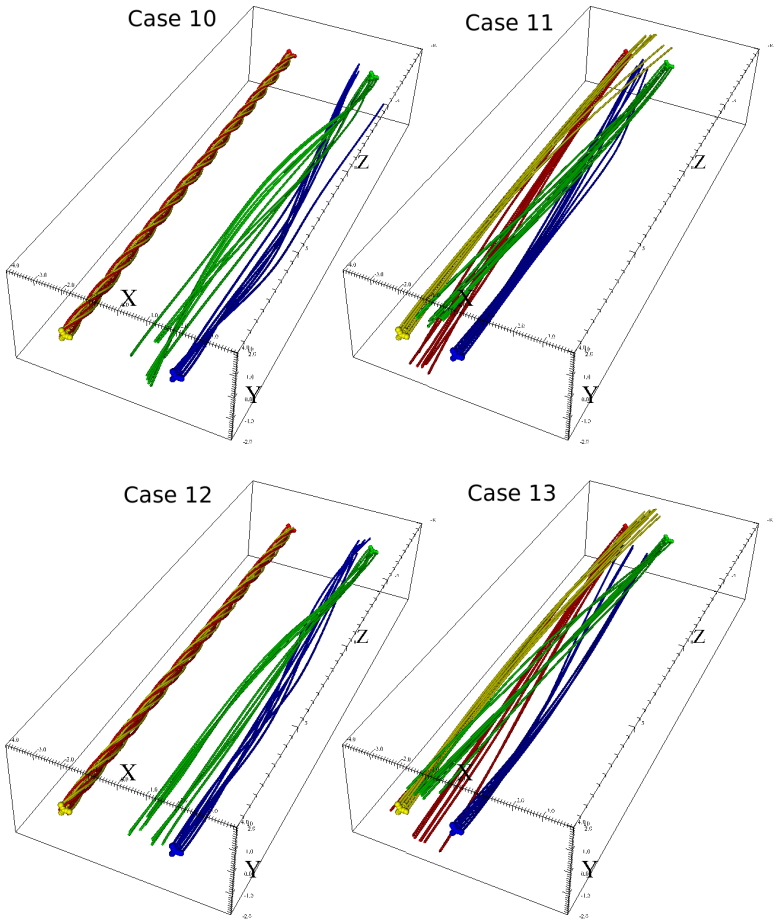

Figure 3.25: $t = 300$: The field line plots for Cases 10 to 13 while the field lines are drawn from the respective footpoints.

determine the maximum distances apart where the individual threads can still merge into one loop. The contour plots of current density and field line plots of Cases 10 to 13 are also shown in Figures 3.23 and 3.25 for comparison.

The final stages of the magnitude of the current densities, $j(x, 0, 0)$, for Cases 10 to 13 are also presented in Figure 3.24. The threads on the left are ideally stable to ideal MHD disturbances as $\lambda = 1.4$. i.e. the current density profiles should not change if there is no external force to trigger the kink instability in the stable thread. The red curve for Case 12 in Figure 3.24(a) shows the result we expected. Very little happens to the left-hand side thread as it is not affected by the unstable thread located 2 units away on its right-hand side. However, when the threads are moved together, the stable thread is then driven unstable, as shown in Figure 3.24(b) (*red*). The initial smooth current density profile of the left-hand side thread is disrupted everywhere across $-3 < x < 1$. There is also a maximum peak of current of 2.68 at $x = -1.25$, which is very close to where the threads are touching each other.

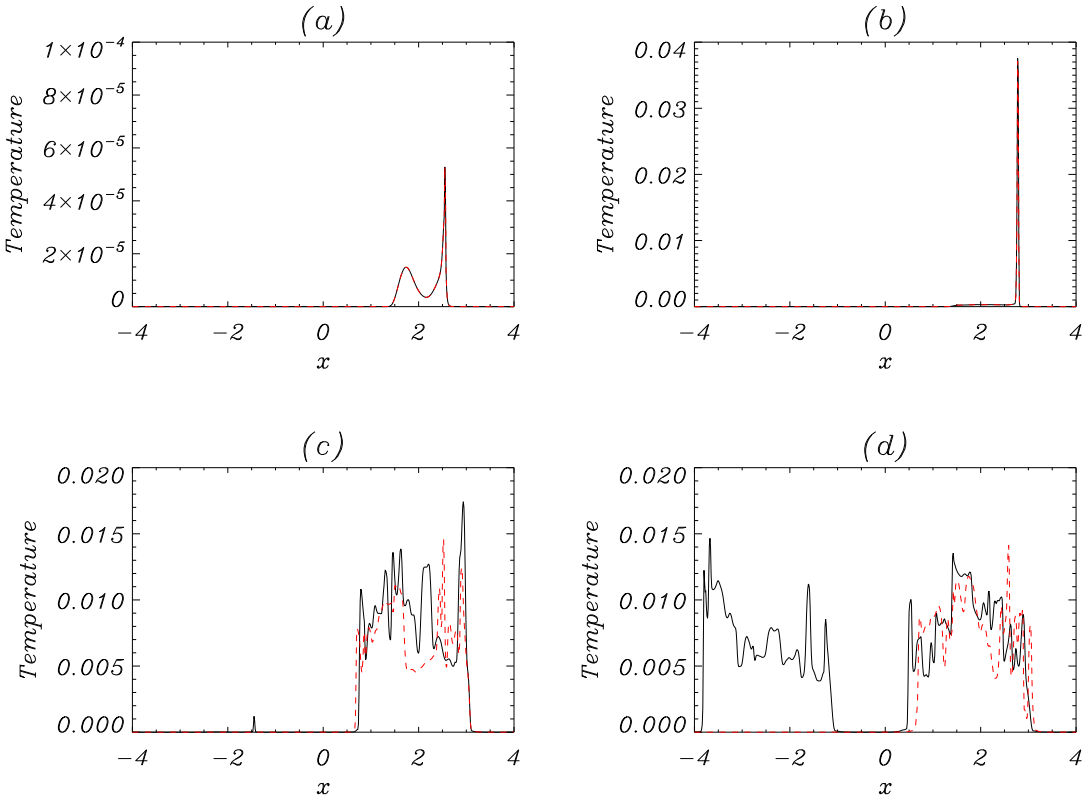

Figure 3.26: Temperature plots, $T(x, 0, 0)$, as a function of x at $y = z = 0$ for Case 8 (*black*) and Case 12 (*red*). The times are **(a)** $t = 60$, **(b)** 80, **(c)** 160 and **(d)** 300.

3.3.4 Heating and temperature profiles

In this section, we will study the temperature profiles as a function of $T(x, 0, 0)$ for the selected cases. The temperature evolution of Case 8 is shown in Figure 3.26 by the black curves. At time $t = 60$, a small amount of heating is detected at the peak where the new current sheet is forming. The peak has a dimensionless temperature of 5.28×10^{-5} and keeps rising. Later at $t = 80$, the peak reaches a value of 0.0376. During the simulation, a kink instability also develops within the left-hand loop and brings a new peak of dimensionless temperature $T = 1.2 \times 10^{-3}$ at $x = -1.4$. This peak is also detected where the new current sheet raises in the left-hand loop at $t = 160$. As the instability develops, the rise in temperature in the left-hand side loop becomes comparable with the loop on the right. The energy and the temperature of these loops are both expanded to about 1.5 times of their original loop radii. By the end of the simulation, the temperature of each loop varies between $0.005 - 0.015$.

The temperature profile of Case 9 is shown as the black curves in Figure 3.27. A peak appears at the edge of the unstable threads, at $t = 60$ and then rises to a value of 0.038 in temperature at

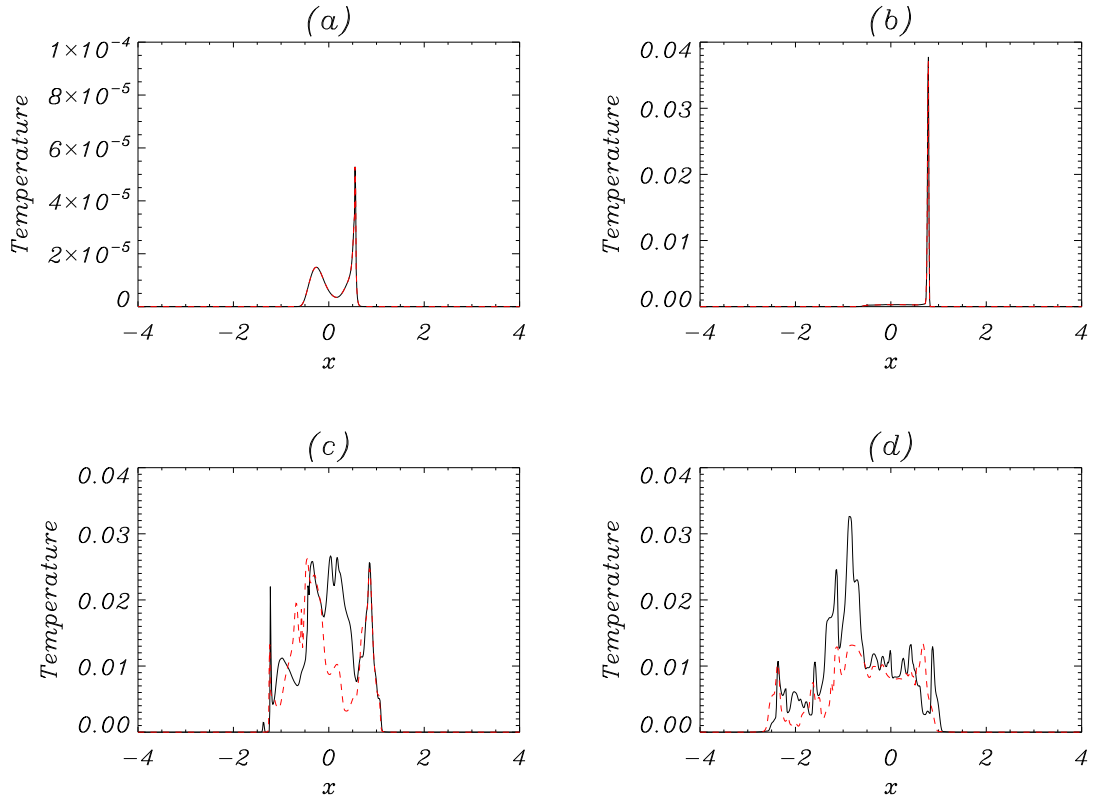

Figure 3.27: The temperature plots, $T(x, 0, 0)$, as a function of x at $y = z = 0$ for Case 9 (*black*) and Case 13 (*red*). The times are **(a)** $t = 60$, **(b)** 80, **(c)** 130 and **(d)** 300.

$t = 80$ in agreement with Case 8 (Figure 3.26(b)). However, as the loops are placed together, there is a change in the temperature evolution. At $t = 130$ (see Figure 3.27(c)), a small temperature peak, with a maximum 2.2×10^{-5}, begins to appear at around $x = -1.4$. It is within the left-hand side thread. These threads are then combined into a single larger loop structure and raise the maximum temperature to a significantly higher value. The maximum temperature in the final stage of the simulation peaks at 0.0326 at around $x = -0.8$. We can also see there is a non-uniform profile of the temperature at $T(x, 0, 0)$ which is distributed now across the region between $x = -2.75$ to $x = 1.25$. The whole of this cross section is heated to a temperature around $0.004 - 0.02$.

These figures show that a higher temperature can be achieved when the threads are moved together. This can presumably be explained in terms of the different volume of heated plasma. The final internal energy in Cases 8 and 9 are approximately the same; however, we have two expanded threads in Case 8 with a larger heated area than the merged threads in Case 9.

Figure 3.26 and Figure 3.27 also show the temperature profiles of Case 12 and Case 13 by the red curves. In Case 12, the left-hand thread is not excited as it is sufficiently far away from

the unstable right-hand thread. It remains in an equilibrium with approximately zero temperature throughout the simulation. In Case 13, when the threads are placed next to each other, both become unstable and combine into a single large loop structure again from $x = -2.5$ to $x = 1.0$ with hot plasma right across this region. The maximum temperature in Figure 3.27(d) is significantly larger for Case 9 than Case 13, since there is more free magnetic energy available to heat the plasma. What is surprising is that the maximum temperature of Case 9 is also higher than Case 8 (see Figure 3.26(d)). So, although both threads are unstable, the temperature is higher when the two unstable threads are touching each other. These plasma, when viewed from the side (from observation), will appear brighter than the cases without a second thread.

The effectiveness of the heating of coronal loops through the excitation of reconnection events in multiple magnetic threads can be assessed by studying the resulting temperatures after the magnetic field has relaxed. The dimensionless temperature after heating is approximately in the range of $\tilde{T} = 0.005 - 0.015$, i.e. around $T = 7 - 21 \times 10^7$ K. These values are again higher than the observed values. Of course, we expect the actual values to be smaller with the inclusion of thermal conduction. This effect will reduce the maximum temperature in the system by about a factor of 10 (Botha et al., 2011). The inclusion of optically thin radiation may reduce this even more. However, the aim of this work is not to exactly reproduce the coronal values but to show that an avalanche effect can occur if the magnetic threads are sufficiently close together.

3.4 Conclusions

In this chapter, we began our case studies with several simple cases to understand the code and the relationship between the parameters. We have also demonstrated some of the techniques we can use to analyse the simulation results, for example, figures of energetics, temperature, field lines evolutions. We were able to show that an equilibrium magnetic thread triggered by a kink instability is able to release sufficient energy when governed by Taylor relaxation theory. Subsequently, in the second part of this chapter, we have extended the study in order to determine whether or not the avalanche effect exists in the same kind of environment.

We enlarged the computational domain so that we could identify whether an unstable thread is capable of destabilising a neighbouring thread. In our experiments, we consider two magnetic threads in our system, with one thread always unstable to the kink instability and excited by an initial velocity perturbation. The second thread is either in a stable, marginally unstable or unstable equilibrium and is placed either beside the unstable thread or a distance of 2 units away from the edge of it. This gives 6 different combinations for the arrangement of the magnetic threads. A summary of the results is presented in Table 3.2. It shows the times at which there is a rapid decrease of magnetic energy in the first thread and the second thread. This gives a reasonable

Energy release	Time (τ_A)					
	Case 8	Case 9	Case 10	Case 11	Case 12	Case 13
First thread	68	68	68	68	68	68
Second thread	164	135	-	141	-	138
Final states	Case 8	Case 9	Case 10	Case 11	Case 12	Case 13
Magnetic energy	-3.031	-3.069	-1.493	-2.698	-1.495	-2.317
Internal energy	+2.813	+2.864	+1.407	+2.494	+1.401	+2.154

Table 3.2: Energies: The time at which magnetic energy starts to decrease in each case, together with the change in magnetic and internal energies by the end of the simulations.

estimate of when the main heating begins in the plasma. For all cases, the first thread begins to release its free energy at the same time. From Case 9 we see that the start of the second energy release occurs sooner when the threads are closer together than when they are further apart. Cases 9, 11 and 13 are almost at the same time, even though the left-hand side thread in Cases 11 and 13 should remain stable (for more than 300 Alfvén times) without the presence of the unstable nearby threads.

The remarkable result from these simulations is that, an individual stable magnetic thread can be destabilised by a neighbouring unstable thread, providing that they are close enough together. However, it is not immediately clear whether this loop can subsequently destabilise another stable thread. It is difficult to run such a simulation. Sufficient grid resolution is required to ensure that numerical dissipation does not cause an individual thread to evolve in an artificial manner. Our investigations suggest that each thread must have the order of 80 (lower resolution) or 160 (higher resolution) grid points across their diameters. In addition to this, there may be potential fields in between the threads and there must be a gap at the sides to remove the influence of the side boundary conditions. Hence, with our present computing resources, we can realistically simulate two (at high resolution) and possibly three magnetic threads (at lower resolution). Initial results for three threads (at lower resolution) suggest that one unstable thread can destabilise only one other thread. Moreover, each thread has the same basic form of magnetic field with two parameters: namely the field strength on the thread axis and the twist parameter, λ. Both threads are twisted in the same sense. Another experiment (which is not presented in the thesis) shows that reversing the twist in the second thread (basically reversing the direction of the axial current) results in Case 13 only having the one unstable thread. So the sense of twist could be important in whether an avalanche occurs or not. There are now many different configurations that must be investigated before one can reach firm conclusions regarding the onset of a true avalanche effect.

Chapter 4

Thermal Conduction And Optically Thin Radiation

We have seen that nanoflare heating can heat the plasma to several MK (Cargill, 1994; Cargill and Klimchuk, 2004; Bradshaw and Cargill, 2006), while a magnetic field begins to relax and plasma is free to cool down by thermal conduction and optically thin radiation. These cooling mechanisms can reduce heat effectively, but they may not happen simultaneously. It is because at the coronal temperatures, the thermal conduction timescale is much shorter than the radiation timescale. The ratio between the two is highly dependent upon the density and the plasma temperature. The denser the plasma in the magnetic field, the more energy losses due to optically thin radiation. The typical coronal timescales of thermal conduction and radiation are 600 and $3,000$ seconds (Priest and Hood, 1991). The difference between the two timescales indicates that optically thin radiation is less important in the coronal environment, which will be discussed in Section 4.2.4.

The aim of this chapter is to extend previous work by including additional physics, namely thermal conduction and optically thin radiation. Hood et al. (2009) showed that it is possible to heat the solar corona through the nonlinear 3D evolution of a kink mode instability, when only considering ohmic heating and viscous heating. Botha et al. (2011) have also shown in simulations that thermal conduction can spread the energy across more of the plasma and reduce the excessive loop temperatures achieved by Hood et al. (2009).

We will begin to introduce the other class of cooling mechanism, optically thin radiation, which was absent from the series of kinked unstable 3D models. We will also include thermal conduction in the simulation, which will improve the system's energy balance. Zero or one-dimensional models that included optically thin radiation have also been presented by many authors, such as Cargill (1994), Cargill and Klimchuk (2004), Klimchuk et al. (2008) and Bradshaw and Cargill (2010). These models are run with both medium to large length scale and high initial temperature (several MK). Their simulations are also run for $1,500 - 2,500$ seconds (or even 5000 seconds in some cases), to try to produce actual emission measures by adding results from hundreds of models. Such configurations allow both cooling mechanisms, namely thermal conduction and optically thin radiation, to cool down the plasma. Due to the fact that optically thin radiation has a very long timescale and thus, is less important in a fast energy release model. Reale and Landi (2012) have also investigated ways to change and improve the radiative losses in simulations,

such as: (1) using more accurate atomic data and transition rates; (2) increasing the plasma ion abundance composition and (3) changing the plasma element abundance composition.

We will study six separate cases to investigate the importance of thermal conduction and optically thin radiation during their evolution: the heating of a cool loop to coronal temperature (from $2,000$ K to a few MK). In each case, the magnetic loop is initially in an unstable equilibrium with zero net axial current. It is also sufficiently twisted that it is unstable to an ideal kink instability. Such a set up will create the initial current sheet that will trigger magnetic reconnection. The magnetic energy released from this event will be converted into some kinetic energy, but mainly into heat.

For the cases investigated, we have a computational domain with sizes $L_x = 4$ and $L_y = 4$, that is 4 times the radius of the coronal loop to ensure that the effects of the rigid wall boundary conditions are minimised and $L_z = 20$ in the axial direction. Each equilibrium loop has a normalised radius of one and, therefore, has the same aspect-ratio of 20, as in previous works (Browning and Van der Linden, 2003; Browning et al., 2008; Hood et al., 2009). We have run all the simulations with two different grid resolutions, namely a lower resolution with $100^2 \times 400$ gridpoints and a higher resolution with $200^2 \times 800$ gridpoints. The higher resolution does reveal more fine structures, as expected, but the detailed time evolution, for example of the total energies, is only weakly dependent on the resolution. If the same features appear in the two different resolutions, then we believe that they have been resolved. The cases we investigate are:

Case 14: An unstable equilibrium loop with initial temperature of 2×10^4 K but without the effects of thermal conduction effect and optically thin radiation. This is our reference evolution.

Case 15: As for Case 14 but with thermal conduction effect included. This case almost similar to that investigated by Botha et al. (2011), except that we have a different boundary condition, grid resolution and we have set a minimum temperature.

Case 16: As Case 14 but with only optically thin radiation included. By neglecting thermal conduction, we can determine the importance of radiation on its own.

Case 17: As Case 14 but with both thermal conduction and optically thin radiation included.

Case 18: As Case 17 but with the initial density increased by a factor of two. This enhances the importance of the optically thin radiation term by a factor of 4.

Case 19: As Case 17 but with the initial density increased by a factor of three.

In Case 17, the simulation result shows that the radiative losses are not particularly important, especially when the temperature is high. Hence, Case 18 and 19 are introduced to investigate the importance of radiative losses when it is enhanced by factors of 4 and 9 receptively.

4.1 Numerical method

The *Lare3d* code and the numerical method have been discussed in Sections 2, therefore, we will not repeat ourselves here. In this chapter, the initial equilibria are the same as previous sections and a brief summary is listed below:

- $B_0 = 5 \times 10^{-3}$ Tesla, $\rho_0 = 1.67 \times 10^{-12}$ kg m^{-3};
- The minimum temperature is raised; now $T = 2 \times 10^4$ K;
- The temperature at the boundaries is no longer free-floating (fixed at $T = 2 \times 10^4$ K);
- Thermal conduction and optically thin radiation effects are included.

Such configuration is chosen to prevent the code from crashing, as it is difficult to compute the energy and δt when the grid temperature drops below $T = 2 \times 10^4$ K. This configuration will give a very short timescale, $t_A = 0.7249$ seconds. Our simulations, which are run for 300 Alfvén times, will be shown to be approximately 216 seconds in real time. As previously stated, optically thin radiation is less important over short times; thus we should expect that the optically thin radiation is not important, in general. However, we will try to increase the plasma density and length scale in a number of our simulations to enhance the radiation effect.

4.2 Numerical results

4.2.1 Energy evolutions and maximum temperature

We begin our analysis by studying the behaviour of the three different energy terms, integrated over the computational volume. We then investigate how the maximum temperature within the computational domain is changed under the effects of thermal conduction and optically thin radiation.

Figure 4.1 shows the time evolution of the volume integrated magnetic, kinetic and internal energy for Cases 14 to 17. The solid curves in black are for Case 14, which show the evolution without thermal conduction and optically thin radiation effect. The dashed curves in blue are for Case 15 with thermal conduction added, while the dotted-dashed curves in red are for Case 16 which has only the optically thin radiation added. The double-dotted-dashed curves in purple are for Case 17, which show the evolution with both thermal conduction and optionally thin radiation included. All cases start with the same initial temperature of 2×10^4 K and evolve in response to the non-linear development of the kink instability. The initial stage (up to about 65 seconds) is

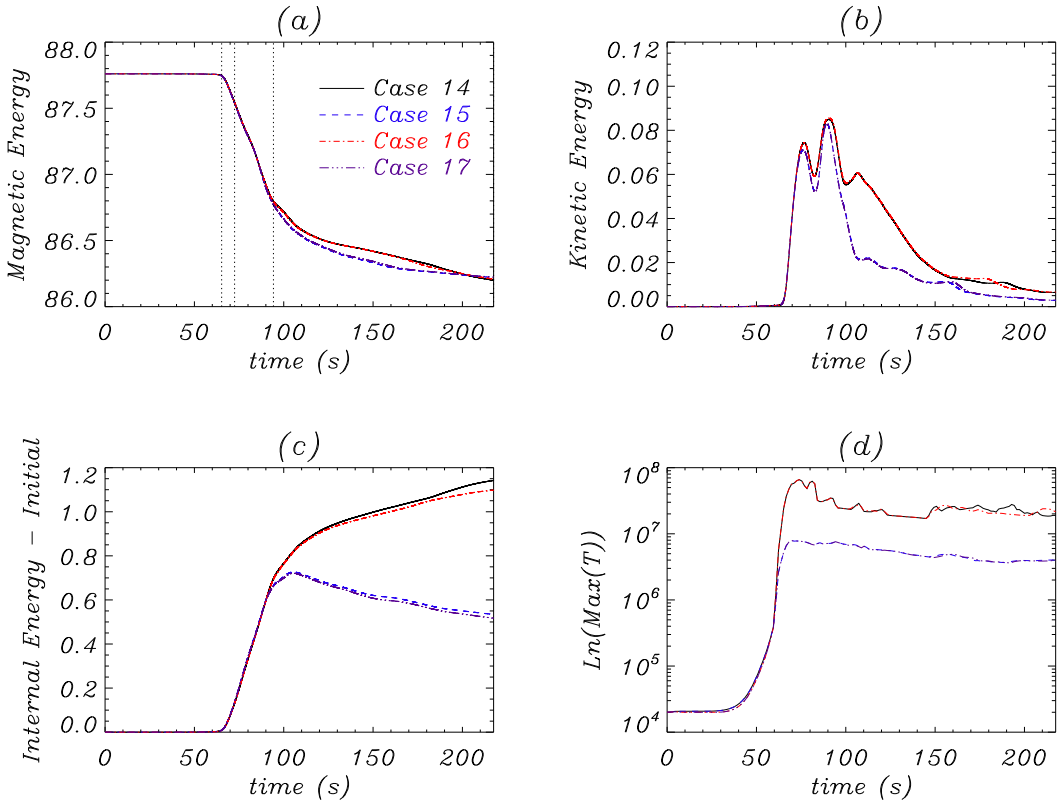

Figure 4.1: The volume integrated energies as function of time (in real units) for **(a)** magnetic energy, **(b)** kinetic energy and **(c)** internal energy. In **(d)**, the maximum temperature is shown as a function of time. Case 14 (*black solid* curves) is the reference case which has no thermal conduction and no optically thin radiation included, Case 15 (*blue dashed* curves) includes only thermal conduction, Case 16 (*red dotted-dashed* curves) includes only optical radiation and Case 17 (*purple double-dotted-dashed* curves) includes both. All of these cases have an initial temperature of 2×10^4 K.

the development of a helical current sheet (e.g. Figure 3.8), as the most unstable mode of the kink instability grows from a given initial perturbation. The initial perturbation is very small, allowing the instability to develop naturally. Hence, the initial stages behave as an ideal plasma and the magnetic energy remains unchanged. As a consequence, the maximum current also remains below the critical value ($j_{crit} = 5$), so that the resistivity remains zero and therefore the initial energy remains at its initial value. There is no heat generated during this stage.

Around $t = 50$ seconds, the maximum temperature begins to rise. It is only visible in the logarithm plot of the maximum temperature in Figure 4.1(d). This increase must be localised and is simply due to the compression of the plasma, as a current sheet is beginning to form. At $t = 65$ seconds, the volume integrated magnetic energy begins to decrease. During this stage, resistivity becomes important, as the critical current is reached. Magnetic reconnection develops, untwists

the magnetic field lines and releases magnetic energy. The magnetic energy released will heats the plasma within the loops through both ohmic heating and viscous heating in shocks. Since the initial temperature is low, slow mode shocks are easily formed. The rapid loss of magnetic energy is the same for all cases and lasts until $t = 90$ seconds. This comes towards the end of the rapid release of magnetic energy and the evolution is independent of the additional terms in the internal energy equation. The evolution is solely governed by the magnetic forces. After $t = 90$ seconds, the subsequent release of magnetic energy becomes significantly slower, as the field relaxes towards a lower energy state through many small-scale reconnection events. A difference can now be observed between the cases: the magnetic energy in Cases 14 and 16 (i.e. without thermal conduction) is nearly identical during the simulation, indicating that radiation effect does not have a substantial influence on the release of magnetic energy in our simulation. The reason for this is the kinked instability is due to Lorentz force and plasma β is still small (less then 0.05), so the pressure of plasma does not change the evolution of instability. Meanwhile, the loss of magnetic energy increases slightly for $90 < t < 200$ in Cases 15 and 17 (i.e. with thermal conduction included). By the end of the simulation, the loss of magnetic energy in each case is approximately the same.

The kinetic energy curves for Cases 14 to 17 all follow the same general evolution (see Figure 4.1(b)). At time $t = 65$ seconds, the curves begin to rise rapidly as the magnetic energy decreases. There are two peaks around $t = 73$ and 90 seconds, with a possible third peak at $t = 94$, before the kinetic energy decreases towards zero as the field relaxes towards its final state. There are slight differences again with the cases in which thermal conduction is included. For example, in Cases 15 and 17, the kinetic energy has slightly narrower and lower peaks at $t = 73$ and 90 seconds, and is noticeably lower after $t = 94$, suggesting that thermal conduction does influence the magnetic force and the plasma motion.

The volume integrated internal energy shows the largest variation of the four cases studied. As we can see in Figure 4.1(c), all the curves match each other until $t = 94$. When optically thin radiation is included (i.e Case 16), only a small amount of internal energy is reduced compared to the reference case (i.e. Case 14), but when thermal conduction (i.e. Cases 15 and 17) is included there is a significant reduction in the internal energy. The high temperature is quickly conducted away from localised hot spots in the volume.

The variation of the maximum temperature as a function of time is shown in Figure 4.1(d) . Due to the fact that radiation is most efficient at transition region temperatures, it has no significant influence on the maximum temperature until well after the main release of energy. On the other hand, it is clear that thermal conduction reduces the maximum temperature to around 10^7 K, as compared with Cases 14 and 16.

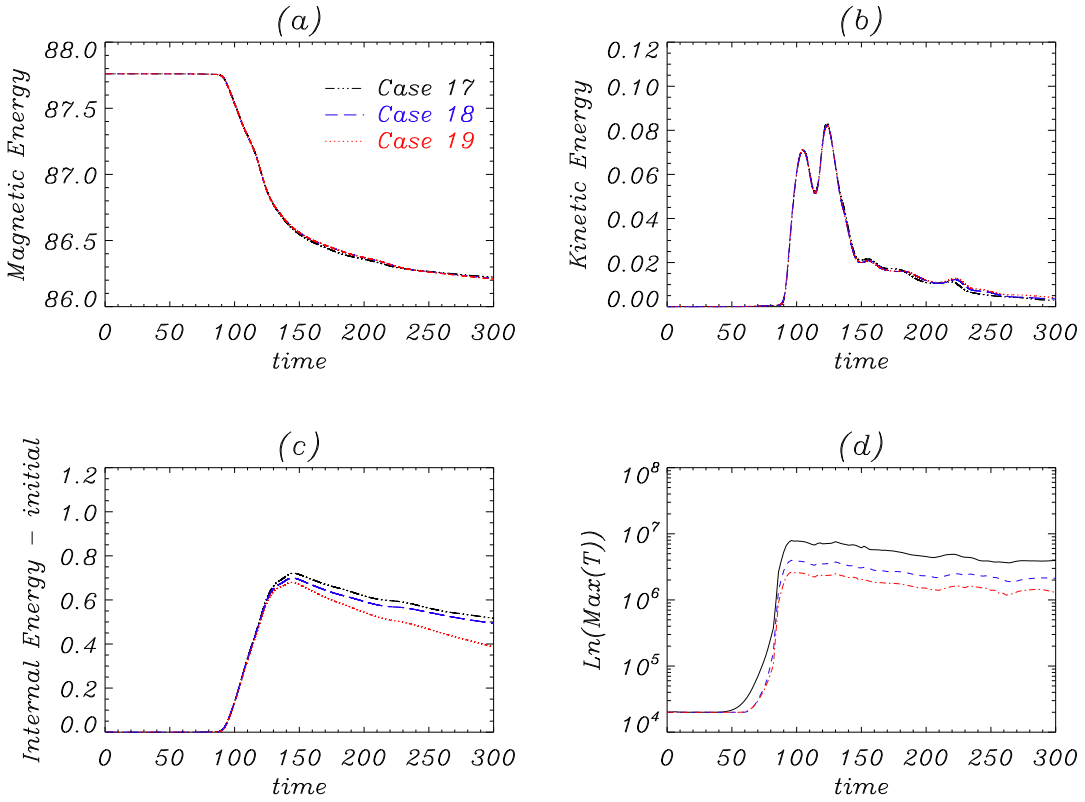

Figure 4.2: The volume integrated energies as function of time (in dimensionless unit) for **(a)** magnetic energy, **(b)** kinetic energy, **(c)** internal energy. **(d)** the maximum temperature over time. All cases have an initial temperature of 2×10^4 K and are under the influence of thermal conduction and optically thin radiation. Here, Case 17 (*black solid* curves) is the reference case, while Case 18 (*blue dashed* curves) has the initial density enhanced by 2 and Case 19 (*red dotted-dashed* curves) has the initial density enhanced by 3.

4.2.2 Enhanced radiation

To increase the importance of radiation, we compare the results from Case 17 with two additional cases, Cases 18 and 19, that have the initial density increased by factors of two and three respectively. Increasing the density will not only increase the size of optically thin radiation but also increases the Alfvén timescale. Therefore, the kink instability will occur later in Cases 18 and 19 when compared to Case 17.

To make a more accurate comparison, the volume integrated energy and the maximum temperature plots are shown in Alfvén time units (see Figure 4.2). The evolution of the integrated magnetic and kinetic energy curves are similar, while the internal energy and the maximum temperature show different behaviours. The internal energy drops even further in the cases with higher density. The value of the maximum temperature is also reduced, due to the enhancement of op-

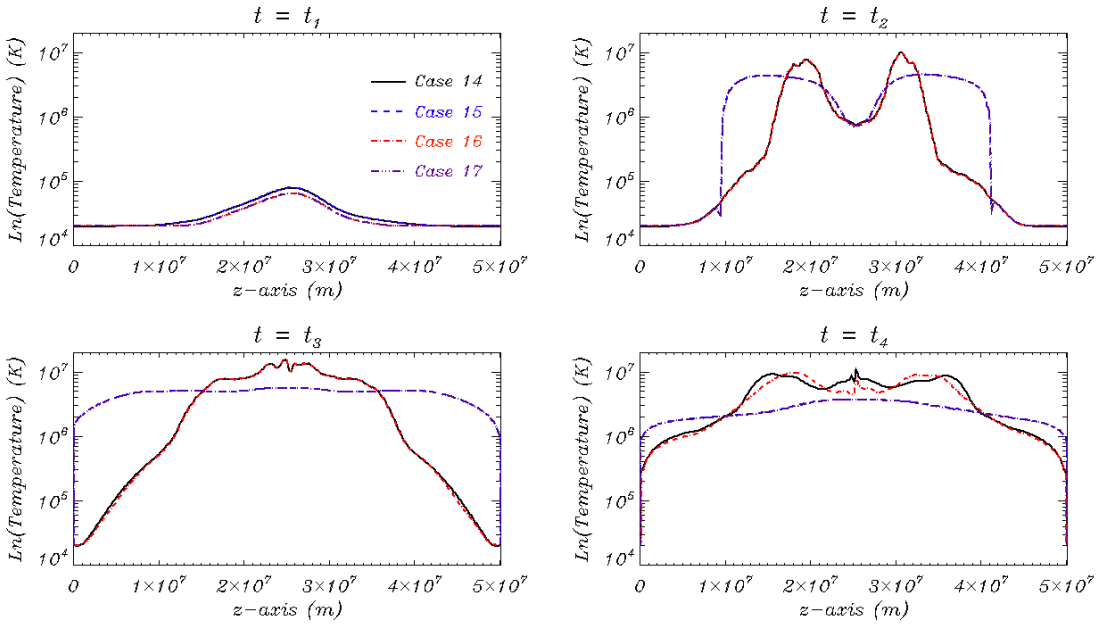

Figure 4.3: The temperature of Cases 14 to 17 are shown as a function of z at $x = y = 0$, for the times $t_1 = 65$ s, $t_2 = 73$ s, $t_3 = 94$ s and $t_4 = 218$ s. Here, Case 14 is shown in black solid curves, Case 15 in blue dashed curves, Case 16 in red dashed-dotted curves and Case 17 in purple dashed-triple-dotted curves, which matches with the curves for Case 15.

tically thin radiation as it is now more efficient at cooling the plasma. We note that the initial increase of the maximum temperature is delayed in Cases 18 and 19. Radiation is very efficient at transition region temperatures and hence more heating is required to raise the temperature higher. The enhanced cooling also means that the integrated internal energy is reduced at a faster rate for Case 19 than the other two cases (see Figure 4.2(c)).

4.2.3 Temperature structure formation and evolution

To understand how the temperature evolves throughout the loop, we plot the temperature as a function of z, at $x = 0$ and $y = 0$, at different times. In Figure 4.3, $t_1 = 65$ seconds corresponds to the start of the kink instability; $t_2 = 73$ seconds is during the non-linear rise of the kinetic energy; $t_3 = 94$ seconds is after the main magnetic energy release and the start of the slow evolution towards the final energy state; and $t_4 = 218$ seconds which is the end of the simulation. Once the kink instability is fully developed, $z = 0$ is no longer the location of the loop axis, but this location does demonstrate how heat is being distributed.

At $t = t_1$, the temperature near the mid-point of the loop is beginning to rise slightly higher for Cases 14 and 15 than Cases 16 and 17 with optically thin radiation included. Radiation tends to keep the temperature near the footpoint lower; however, it is seen to be unimportant. By the end of

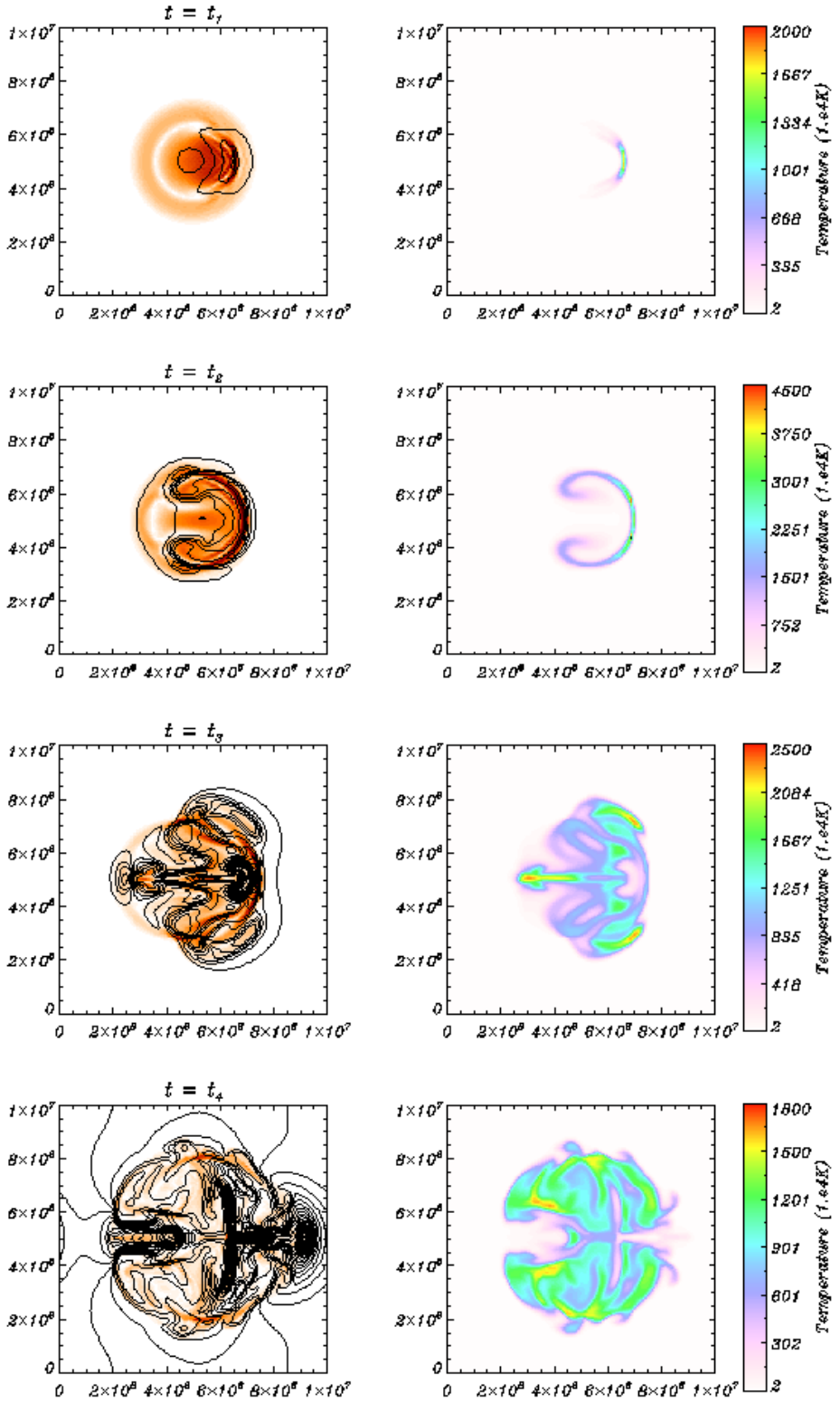

Figure 4.4: Case 14: The current density profile (*left*) and temperature profile (*right*) at $z = 0$ for times $t_1 = 65$ s, $t_2 = 73$ s, $t_3 = 94$ s and $t_4 = 218$ s. The contour plots on the left have colour scale from 0 (*white*) to 6 (*red*) for current density. The plasma density contours are also shown as black curves.

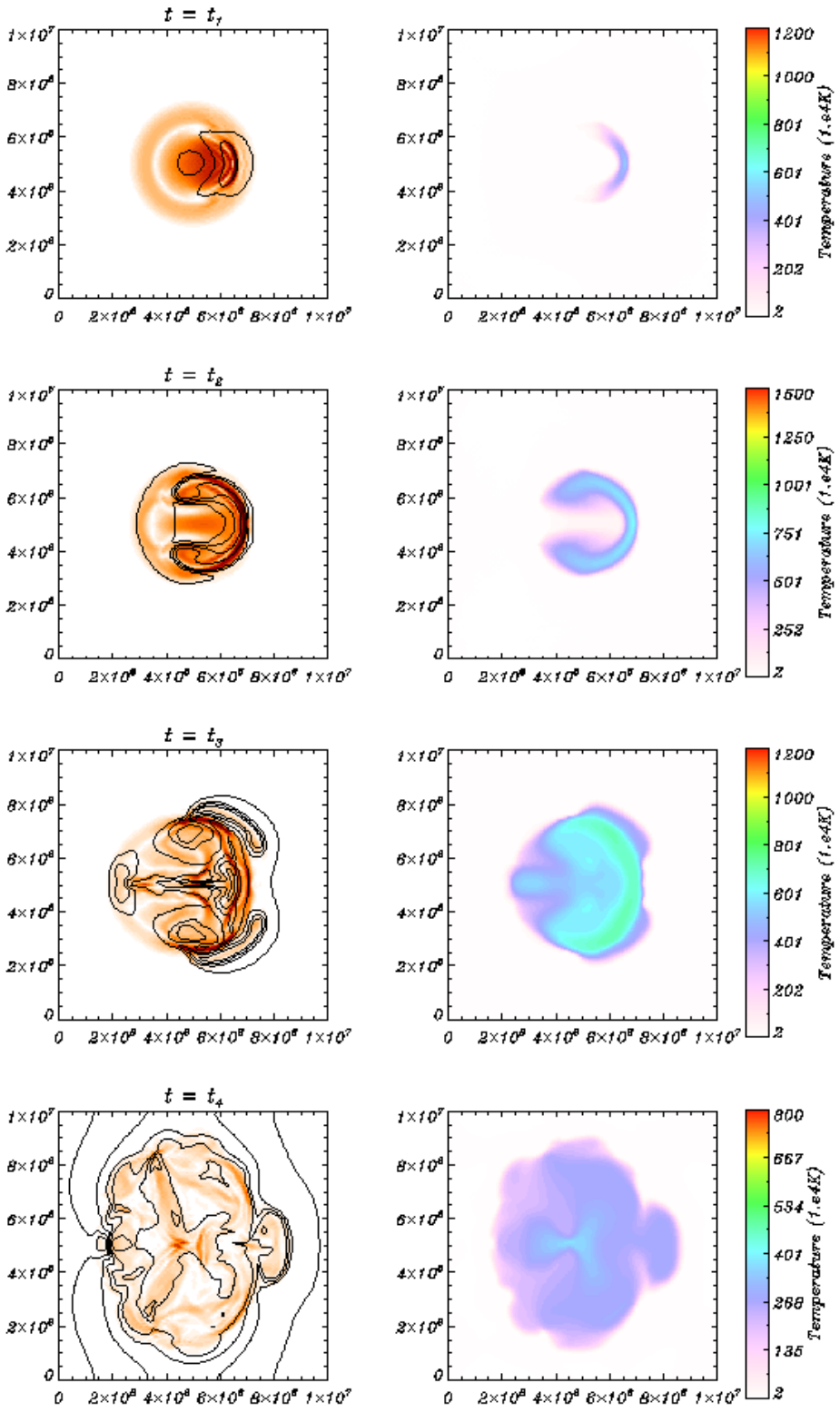

Figure 4.5: Case 17: The current density profile (*left*) and temperature profile (*right*) at $z = 0$ for times $t_1 = 65$ s, $t_2 = 73$ s, $t_3 = 94$ s and $t_4 = 218$ s. The contour plots on the left have colour scale from 0 (*white*) to 6 (*red*) for current density. The plasma density contours are also shown as black curves.

the simulation, at $t = t_4$, the conduction increases the temperature near the footpoints and reduces the temperature elsewhere (Figure 4.3, bottom right). There is a strong conduction front, clearly seen in Cases 15 and 17 at $t = t_2$ and t_3, that propagates down towards the footpoints. Once this conduction front reaches the footpoints, it is difficult for the numerical code to conduct the heat out of the box in an efficient manner. In addition, this rapid heating of the footpoints should result in chromospheric evaporation but it is not allowed by our choice of boundary conditions. It would not be sensible to attempt chromospheric heating without a realistic model for the chromosphere.

Consider now the evolution of current density, plasma density and temperature for Cases 14 and 17, for which the three profiles in the central cross-section of the loop at $z = 0$ are shown in Figures 4.4 and 4.5. The columns on the left-hand side show the magnitude of the current density (in shades of orange) and the plasma density (solid contours), while the right-hand side columns show the temperature contours, with the colour scale shown beside each panel. The overall evolutions are basically the same. However, the inclusion of thermal conduction and optically thin radiation smooths out the fine structures and reduces the temperature globally.

For Case 17, at time $t = 65$ seconds the helical current sheet which is created by the kink instability begins to develop. It is clear that not only is the current density increasing, but also the plasma density. The current sheet formation process causes compression and the density will rise at the current sheet; in addition, the temperature starts to rise in response to the compression and ohmic heating. At time $t = 73$ seconds, vortex patterns are seen near the loop boundary while the current density, plasma density and temperature are all rising, forming part of a ring at the edge of the current sheet. The full nonlinear evolution is shown at later times. At times $t = 94$ and 218 seconds, the current sheet has fragmented into smaller current sheets throughout the loop cross-section. The overall temperature of the loop in the cross-section is raised to above 10^6 K.

4.2.4 Physical timescales

We can understand which of the various physical process dominate during the evolution of these heating events by investigating how the relevant timescales evolve in time. The basic timescale is the Alfvén travel time,

$$\tau_A = L/v_A = L\sqrt{\mu\rho}/B,$$

where L is the length along the field line. It is a constant time timescale used in the dimensionless MHD equations. The conduction timescale and radiation timescale are

$$\tau_C = \frac{pL^2}{(\gamma-1)\kappa_0 T^{7/2}},$$
$$\tau_R = \frac{p}{(\gamma-1)\rho^2\chi T^{\alpha}}.$$

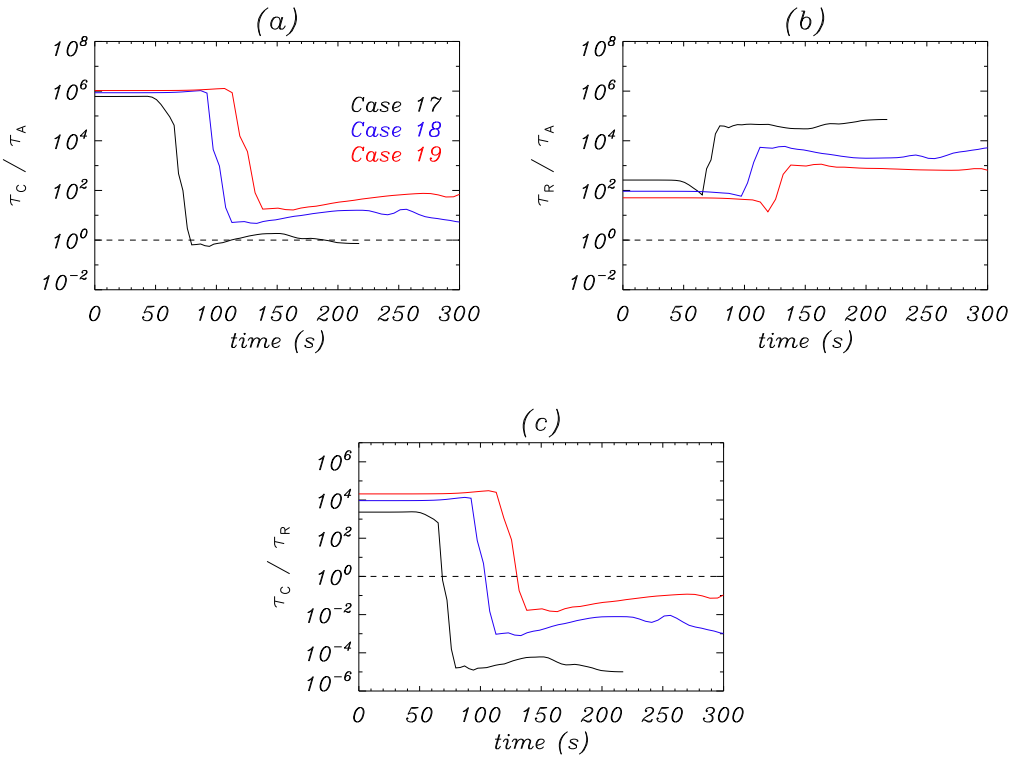

Figure 4.6: Case 17-19: The timescale plots of the plasma at the centre of the domain, i.e. $x = y = z = 0$. **(a)** conduction time/Alfv́en time, **(b)** radiation time/Alfv́en time and **(c)** conduction time/radiation time. The Alfv́en travel time of Cases 17-19 are $\tau_A = 0.7249$, 1.0251 and 1.2556 seconds.

It is obvious that the density, ρ, plays an important role in both of the timescales.

Figure 4.6 shows the ratio of the timescales for Cases 17-19 as functions of time at the centre of the thread (i.e. $x = y = z = 0$). Initially, thermal conduction is unimportant and the ratio (τ_C/τ_A) is large. However, once there is significant heating, conduction becomes more important. The ratio drops slightly below unity for Case 17 but remains above unity for Cases 18 and 19. This means the thermal conduction effect can never really dominate over magnetic effects. The ratio of radiation to Alfvén timescales is shown in Figure 4.6(b) and shows that the radiation timescale is initially 100 times longer then the Alfvén timescales. Initially, the radiation timescale for all cases is slightly above unity at low temperature. It then loses importance quickly as the temperature rises. Enhancing the density in Cases 18 and 19 does reduce the radiation timescale, although this is hard to see due to the logarithmic scale. The comparison of conduction to radiation timescales is shown in Figure 4.6(c). It shows that optically thin radiation dominates over thermal conduction until time around $t = 73$ seconds, while the plasma temperature is low and the instability has not yet been fully developed. However, once the magnetic energy is released and the temperature rises, thermal conduction begins to dominate radiation.

One key result is the fact that neither radiation nor conduction ever really dominate the magnetic properties, as identified by the size of the Alfvén timescale.

4.3 Other properties

The evolution of temperature, plasma density and velocity in our simulations can be computed into quantities for comparison with observational data. The temperature and plasma density are needed to calculate an emission measure (Cargill, 1994; Reale et al., 2000; Botha et al., 2012). The line-of-sight integral for the measured intensity (I) is

$$I = \int_{-L_y}^{+L_y} n_e^2 G(T)\, dy = \int_{-L_y}^{+L_y} \left(\frac{\rho}{m_p}\right)^2 G(T)\, dy,$$

where n_e is the electron number density, ρ is plasma density, m_p is the mass of proton and $G(T)$ is the temperature response function of the respective instruments. The figures in this section are presented simply: the volumes are categorised as $a \leq F < b$, where F represents the variables, as a and b are the minimum and maximum values in the intervals. For example, if the plasma density from the simulation is $\rho = 0.92$, it will be binned in the $0.9 \leq \rho < 1$; similarly, if $\rho = 1$, it will be binned $1 \leq \rho < 1.1$ region (see Figure 4.9).

4.3.1 Temperature and density distributions

In Figure 4.7, the temperature above 10^5 K is plotted as histograms for Case 14 (the reference case) and Case 17 (with thermal conduction and optically thin radiation effect). The logarithmic

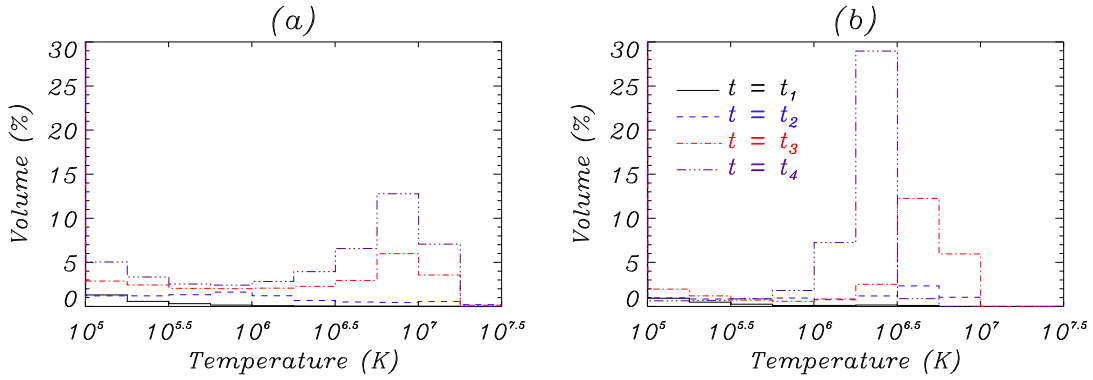

Figure 4.7: The temperature distribution by histogram for **(a)** Case 14 and **(b)** Case 17 for different times. Time $t_1 = 65$ s is shown as black (*solid*), $t_2 = 73$ s as blue (*dashed*), $t_3 = 94$ s as red (*dotted-dashed*) and $t_4 = 218$ s as purple (*triple dotted-dashed*).

temperature at every point in the computational domain is binned. The number in each bin is then multiplied by the cell volume and the total value will be divided by the total volume to create the percentage volume of the simulation at the corresponding temperature. The volume percentage as a function of temperature is shown for four different times.

At time $t_1 = 65$ s, the temperature (*black solid* curves) begins to rise to over 10^5 K in both Cases 14 and 17. The volume of temperature over 10^5 K for Case 17 is slightly lower than Case 14, as the conduction and radiation are continually operating to cool the plasma. During the simulation, the temperature distribution of Case 14 is fairly flat compared to Case 17. At time $t_4 = 218$ s, the temperature of the plasma is widely distributed up to about 2×10^7 K in Case 14, but peaks more strongly around 4×10^6 K for Case 17. It shows that the thermal conduction limits the maximum temperature reached and optically thin radiation reduces the temperature to below 10^5 K (Reale and Landi, 2012), as the peaks around 10^5 K in Figure 4.7(a) are removed in Figure 4.7(b). These can also be observed in Figure 4.8(a), which shows the volume of plasma in different temperature ranges. The curves clearly show that optically thin radiation is strong only around the temperature range 10^5 K $\leq T < 1$ MK. Thermal conduction is the leading cooling effect, as the purple curves overlap the blue curves, for all plasma with temperature range above 1 MK. The general shape of the histogram is similar to the typical active region emission measure distribution (Sakamoto et al., 2009). However, we would need more threads in the system to generate a more realistic distribution for a proper comparison with observations.

The density histogram is shown in Figure 4.9 for Cases 14 and 17, which shows very little difference between the two. For the times t_1, t_2 and t_3, the density is dominated by the initial uniform density at unity. However, at the end of the simulation, t_4, the density distribution is more uniform up to a value of 1.1. Therefore, there is very little dense plasma (except very close to the two footpoints) and more of a reduction in value throughout the majority of the loop. This is due to conservation of mass and the fact that we are not able to resolve the chromospheric evaporation in *Lare3d*. In our simulations, mass conservation holds to within 1%, as does energy conservation.

Figure 4.10 shows that all of the grid cells initially had a dimensionless plasma densities at unity. Once the simulation begins, around 45% of grid cells have their plasma density reduced to slightly below 1. This behaviour is due to the inclusion of an initial perturbation, which changes the pressure of plasma and so the density. It remains roughly the same until the kink instability occurs at time $t = 70$. When the kink instability is rising, the plasma density begins to rise in some of the grid cells. Figure 4.10(a) shows that about 85% of the cells have their plasma density increase back to above unity again. However, a strong current sheet is formed at $t = 100$, when the plasma density begins to fall slowly all the way until the end of the simulation. The purple curves (for Case 17) always overlap with the blue curves (for Case 15), indicating that thermal conduction dominates the cooling effects by controlling the motions of the plasma and the plasma density is rarely reduced to 0.5 or less.

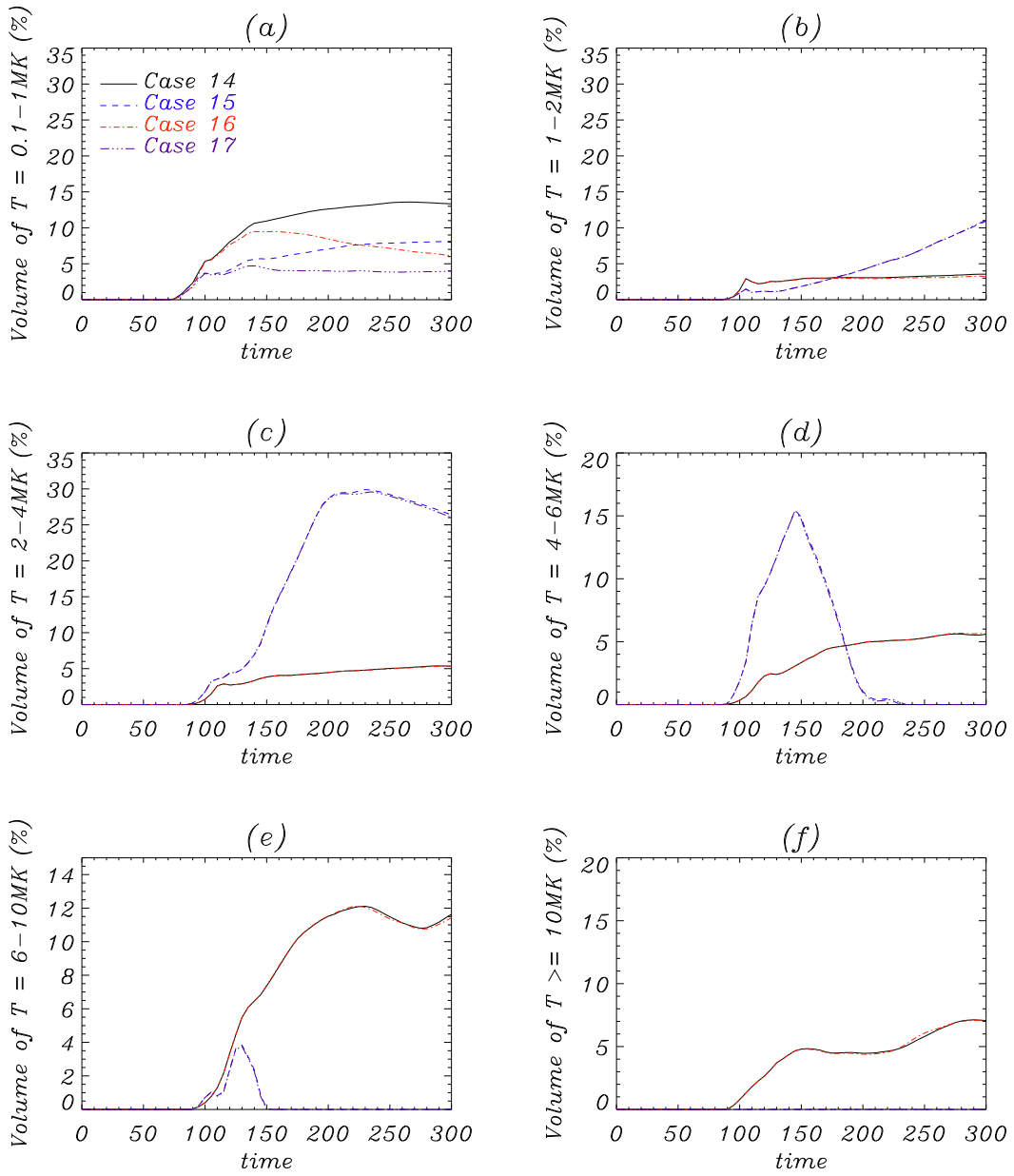

Figure 4.8: The volume of cells over a certain temperature for Cases 14-17, where **(a)** 10^5 K $\leq T <$ 1 MK, **(b)** 1 MK $\leq T <$ 2 MK, **(c)** 2 MK $\leq T <$ 4 MK, **(d)** 4 MK $\leq T <$ 6 MK, **(e)** 6 MK $\leq T <$ 10 MK and **(f)** $T \geq$ 10 MK.

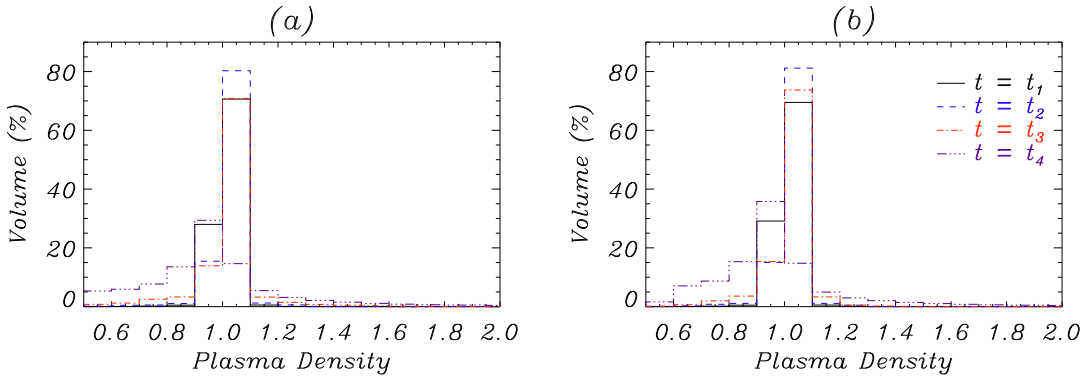

Figure 4.9: The density histogram, in units of the initial uniform density, for **(a)** Case 14 and **(b)** Case 17 at different times. Time $t_1 = 65$ s is shown as black (*solid*), $t_2 = 73$ s as blue (*dashed*), $t_3 = 94$ s as red (*dotted-dashed*) and $t_4 = 218$ s as purple (*triple dotted-dashed*).

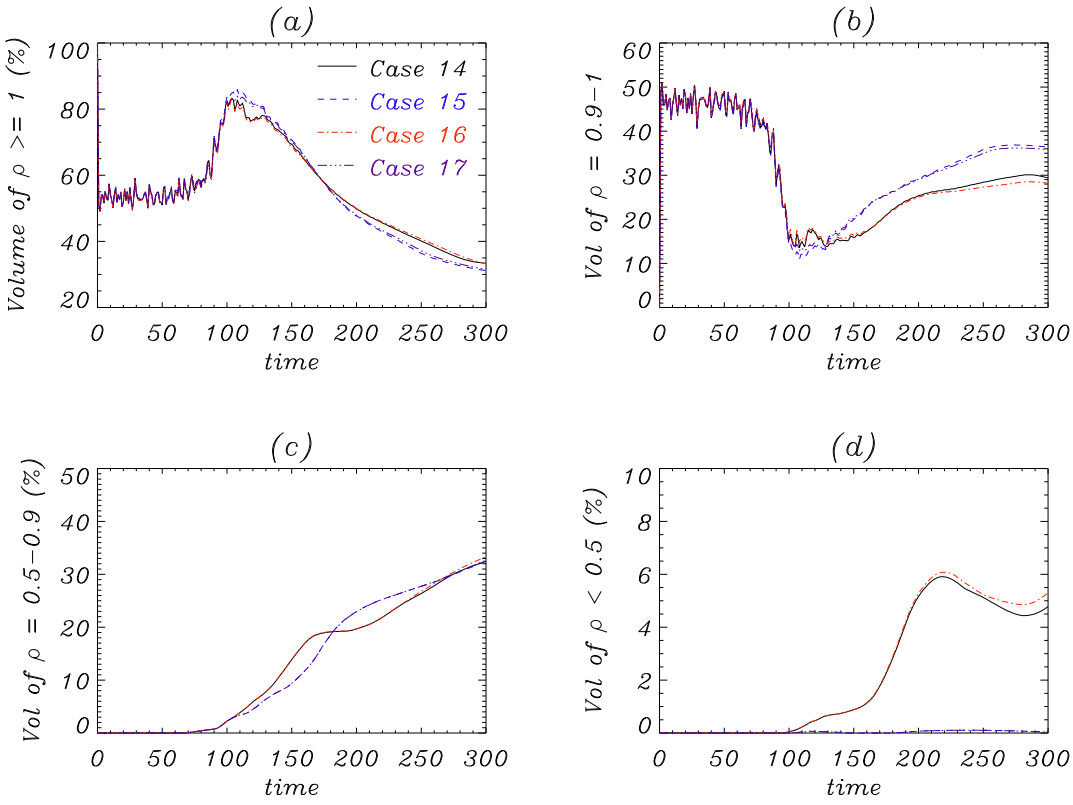

Figure 4.10: The volume of cells over a certain range of plasma density for Cases 14-17, where **(a)** $\rho \geq 1$, **(b)** $0.9 \leq \rho < 1$, **(c)** $0.5 \leq \rho < 0.9$. and **(d)** $\rho < 0.5$.

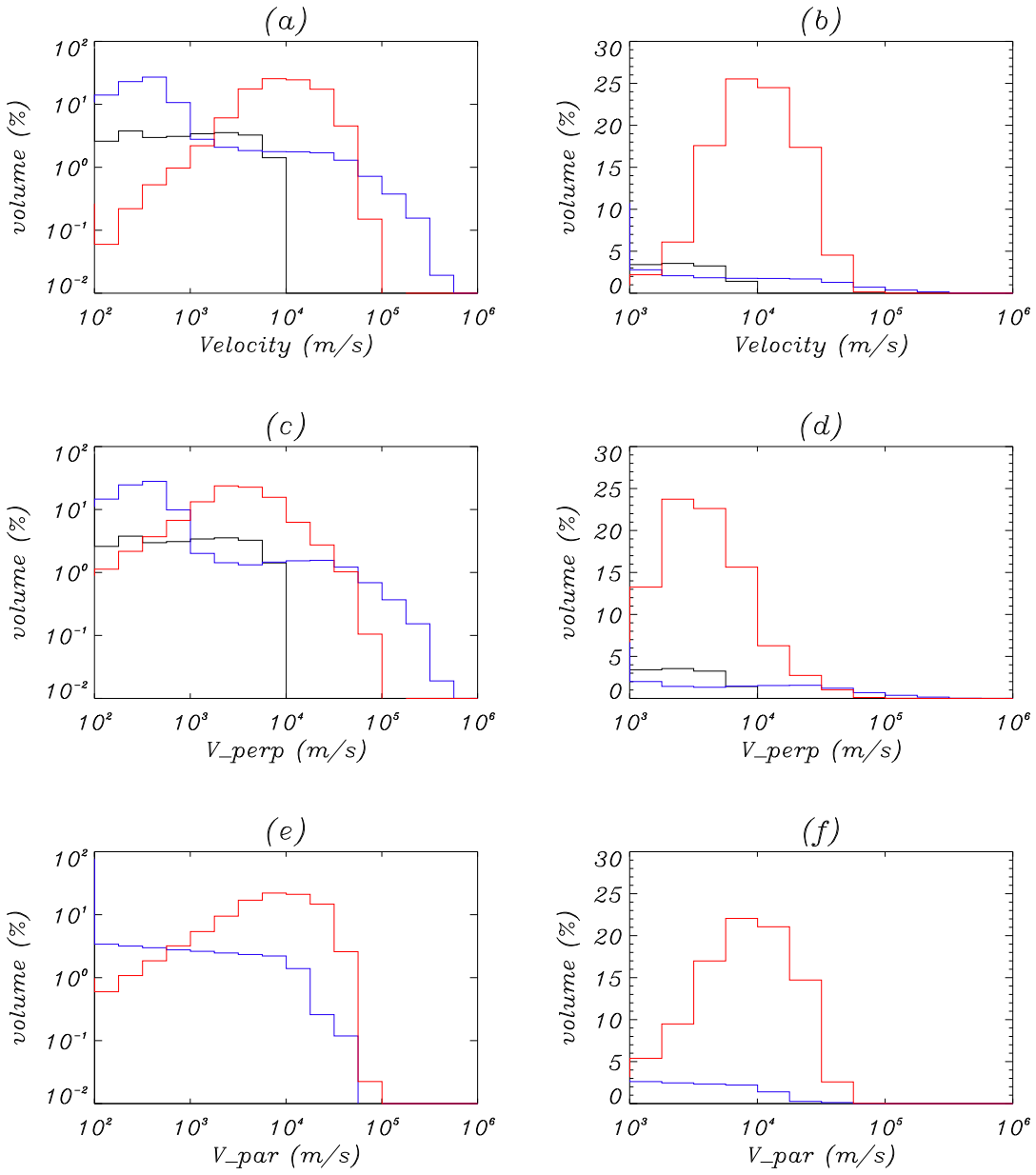

Figure 4.11: The velocity distribution by histogram for Case 17. Black is for $t_0 = 0$ s, blue for $t_1 = 65$ s and red for $t_4 = 218$ s. The top row is the velocity magnitude, the middle row is the magnitude of the velocity perpendicular to the magnetic field and the bottom row is the magnitude of the velocity parallel to the magnetic field.

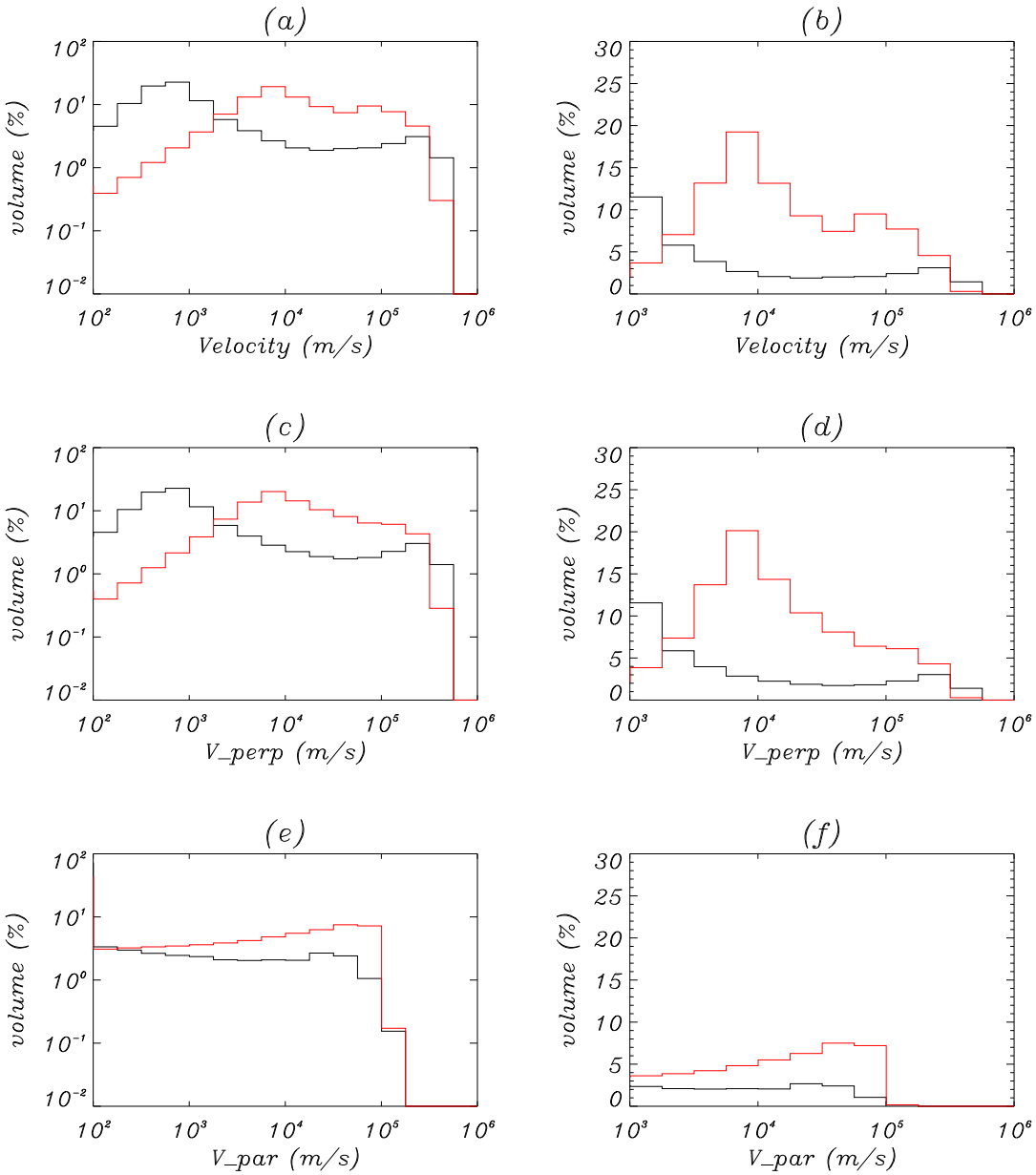

Figure 4.12: The velocity distribution by histogram for Case 17. Black is for $t_2 = 73$ s and red for $t_3 = 94$ s. The top row is the velocity magnitude, the middle row is the magnitude of the velocity perpendicular to the magnetic field and the bottom row is the magnitude of the velocity parallel to the magnetic field.

4.3.2 Velocity distributions

The percentage volume of the velocity distributions of Case 17 are shown in Figures 4.11 and 4.12. The left-hand column shows this as log-log plots, for velocities staying between 100 m s^{-1} and 1 Mm s^{-1}. The right-hand column shows this as log-linear plots, with the slower velocities removed and concentrates on the the speed from 1 km s^{-1} up to 1 Mm s^{-1}. The top row shows the magnitude of the velocity, the middle row shows the magnitudes of the velocity component parallel to the magnetic field and the bottom row shows the magnitude of the velocity component perpendicular to the magnetic field. In our experiments, the speed never becomes super Alfvénic.

At $t = 0$ second, the velocity (Figure 4.11, *black*) is just the imposed initial disturbance. This is essentially confined within the loop and its maximum value should be highly sub-Alfvénic. The velocity disturbance is initially perpendicular to the magnetic field and the parallel component will only develop later through the nonlinear terms in the MHD equations. At time $t = t_1$ (Figure 4.11, *blue*), the ideal kink instability begins to rise. The maximum speed will be around half the Alfvén speed while the percentage volume is still mostly filled by the slow-moving plasma. The main energy release occurs around t_2 (Figure 4.12, *black*) and there is some evidence in these histograms of fast reconnection jets at a few hundred km s^{-1}. The reconnection outflows only involve the reconnecting component of the magnetic field and these will be sub-Alfvénic, when the Alfvénic speed is based on all the magnetic field components. By time t_3 (Figure 4.12, *red*), the main energy release is finished and about 80% of the volume has plasma moving between 5 to 100 km s^{-1}. At the end of the simulation (Figure 4.11, *red*), the majority of the fast flows have slowed and there is now a peak in the distribution about 10 km s^{-1}. Note that this is mainly due to the parallel flows, as the perpendicular velocity peaks at the slower speed of just a few km s^{-1}.

A key result is that the initial velocity is highly dependend upon the perpendicular velocity as in the configuration (see Section 3.2) and it then turns into parallel velocity under the influence of thermal conduction (see Section 2.2.5), as expected.

4.3.3 Velocity-temperature scatter plots

In this section, we will investigate the relationship between the plasma temperature and velocity as the relaxation process takes place. We will plot the velocity at the grid points against the temperature at the same position. Figures 4.13 and 4.14 show the results for Cases 14 and 17, for four different times: $t = t_1$ is during linear phase of the kink instability, t_2 is during the nonlinear phase of the instability, t_3 is after the main release of magnetic energy and t_4 is at the end of the simulation, very close to the relaxed state. The temperatures are restricted to the values above 10^5 K, as we are only concerned with the plasma that has been heated by the relaxation process. Recall that the maximum initial velocity disturbance is 10^4 m s^{-1} and the majority of the hotter

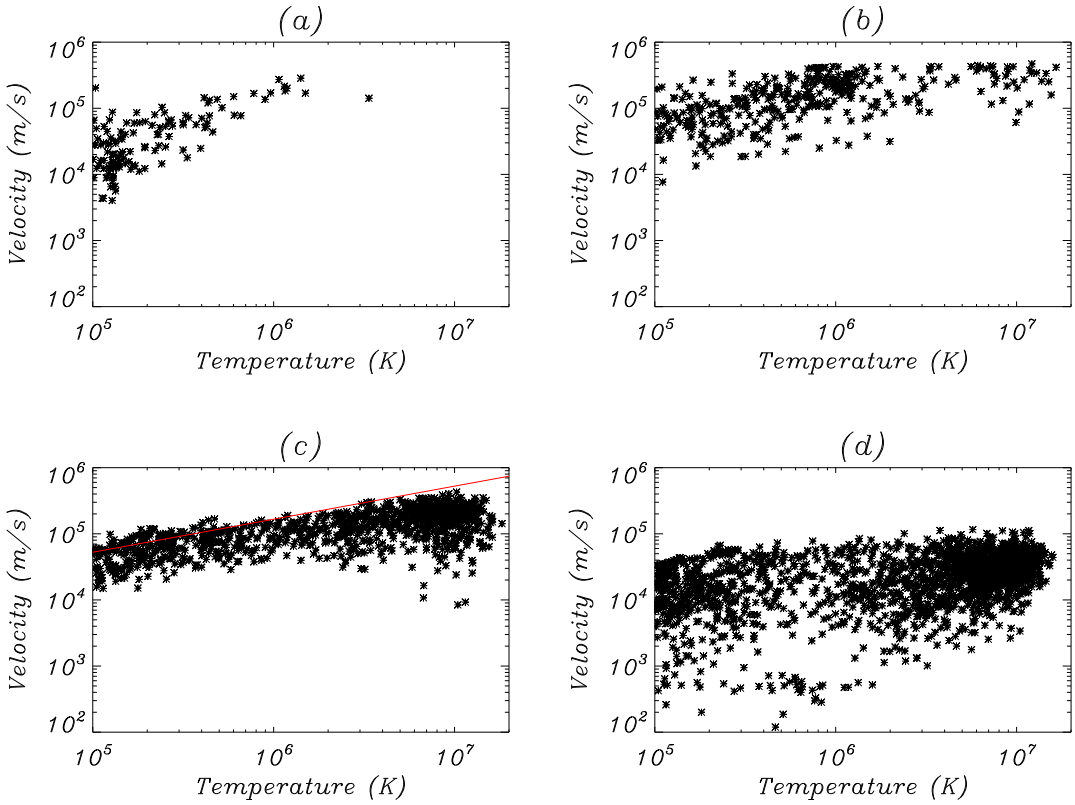

Figure 4.13: The log-log plot of temperature against velocity for Case 14 at four different times: **(a)** $t_1 = 65$ s, **(b)** $t_2 = 73$ s, **(c)** $t_3 = 94$ s and **(d)** $t_4 = 218$ s. The red line in (c) shows the velocity is capped under the sound speed gradient.

plasma will be accelerated to speeds above this initial value. For all four times, there is a weak trend indicating that hotter plasma has a higher velocity.

In our reference case, the thermal conduction and optically thin radiation are not included. Figure 4.13(a) shows that there is very little plasma to be heated above 10^6 K when the instability first starts, while the maximum velocity is around 300 km s^{-1}. The majority of the points show that the plasma is significantly cooler and has a much smaller velocity during the linear phase of the kink instability. At $t = t_2$, as it changes to the nonlinear phase, Figure 4.13(b) shows a much wider spread in temperature, with the hottest regions reaching 10^7 K and a wide range of velocities, from 10 km s^{-1} to a fairly strict upper bound at 400 km s^{-1}. When the instability is well developed and the main release of magnetic energy is finished, Figure 4.13(c) shows a more concentrated plot and the velocity is somehow limited by the sound speed $\left(c_s = \sqrt{\gamma P/\rho}\right)$ for the plasma temperature above 5×10^5 K. At $t = t_4$, the majority of the plasma has been slowed and cooled by the relaxation process. Most of the points are distributed at the low temperature range of 1 to 2×10^5 K and 4×10^6 K to 1.5×10^7 K with a velocity range of $5 - 100$ km s^{-1}.

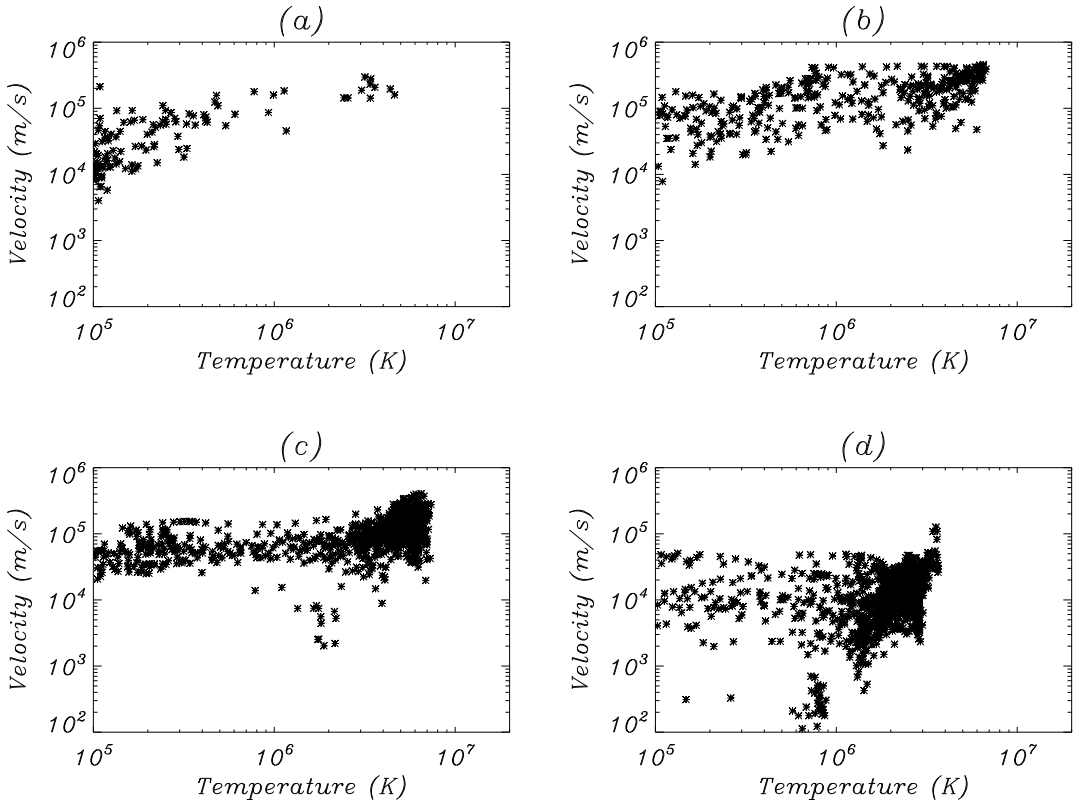

Figure 4.14: The log-log plot of temperature against velocity for Case 17 at four different times: **(a)** $t_1 = 65$ s, **(b)** $t_2 = 73$ s, **(c)** $t_3 = 94$ s and **(d)** $t_4 = 218$ s.

Once the thermal conduction and optically thin radiation effects are included in Case 17, Figure 4.14 shows that these extra effects have removed a significant amount of plasma within the temperature range, (5×10^5 K $\leq T \leq 2 \times 10^7$ K) and the plasma has been slowed and cooled down by the relaxation process as discussed in Section 4.3.3.

4.4 Conclusions

We have investigated how coronal heating develops when governed by Taylor relaxation theory. We used 3D simulations to demonstrate that cylindrical coronal loops can release sufficient energy to the heat the corona. When a loop becomes kink unstable, magnetic energy is released; a large helical current sheet forms, reconnection occurs and is followed by current sheet fragmentation. Eventually the magnetic topology relaxes to a minimum energy state.

In this chapter, we included thermal conduction and optically thin radiation effect in the case studies. Thermal conduction effectively reduced the maximum temperature (as well as the plasma

density) and also smoothed out the temperature along the magnetic field lines. Significant reductions of fine structures in the isosurface of current density, plasma density and temperature were also observed. Optically thin radiation was shown to be unimportant in the temporal evolution in our magnetic field configuration (e.g. sub-Alfvén time). We have also run some experiments with higher density, which leads to an enhancement in the radiation effect (as $L_r = \rho^2 \chi T^\alpha$); thus we can demonstrate the effect of optically thin radiation (see Appendix B). We will run simulations with much larger length scales to increase the Alfvén and conduction timescales and demonstrate the importance of optically thin radiation.

A clear result of our simulations is that, in the coronal environment, the cooling effect of kinked-unstable loops is dominated by thermal conduction; optically thin radiation is less important as it requires a longer timescale to become active. This agrees closely with the previous 1D simulations carried out by many authors, such as Cargill (1994), Cargill and Klimchuk (2004), Sarkar and Walsh (2008) and Reale and Landi (2012). Our results have been studied in detail: the energetics, magnetic and velocity components, current sheet structures, connectivity of magnetic field lines and temperature evolution were all closely examined. We will also introduce a number of new techniques to enhance our analysis, for example, magnetic topology and forward modelling. The techniques will be discussed in Chapter 6.

Chapter 5

Final Discussions

After this series of experiments, it is perhaps appropriate to ask "what solar phenomenon is the kink instability most applicable to?". Our discussion may begin by evaluating the energy released during the instability. Here, we will consider the energy released by the simulations and nanoflares.

Figure 4.1(a) shows the energy releases in two phases: an initial drop which lasts for about 30 seconds and slower decline which lasts for about 200 seconds. The dimensionless energy decreases by roughly 1 and 0.4 dimensionless energy units respectively. This can be contrasted with the results of Browning et al. (2008) who showed a decrease in the energy of roughly 1 and 0.3 units in 30 and 200 Alfvén times. Another case (their Figure 10) showed a rapid decrease of 4 units in 30 to 40 Alfvén times. These values need to be converted into real units.

To begin with, we note that absolute energy values in these figures depend to a considerable degree on the spatial extent of the system since the energy is calculated cumulatively over the computational domain. The total energy is $W = \int B^2/2\mu \, dV$, which integrates over the box with B being the dimensionless magnetic field strength and $L_x = L_y = 4$ and $L_z = 20$. We need to multiply these results by the appropriate units, namely $W_0 = B_0^2 r_0^3/\mu_0$.

For this thesis, $B_0 = 5 \times 10^{-3}$ Tesla, $r_0 = 2.5 \times 10^6$ m and the length of the loop is 100 Mm with the aspect ratio 1:20. Therefore, $W_0 = 3 \times 10^{20}$ J. As the loss of total magnetic energy was about $1.5 - 1.6$ units in our experiments, so the energy released will be slightly greater. We can observe that both the magnetic field strength and the length scale somewhat unrealistic. For a typical coronal loops, magnetic field strength of $B_0 = 10^{-2}$ Tesla and loop length of 80 Mm seems reasonable. By keeping the same aspect ratio, the radius becomes $r_0 = 2 \times 10^6$ m, i.e $W_0 \approx 6 \times 10^{20}$ J. Thus, the energy release by kink unstable mode is too large for a single nanoflare (a few 10^{16} J, see Testa et al. (2013)). However, there are other events within this energy range, e.g. microflares and solar flares, for which the kink instability is an attractive solution.

Microflares were discovered during a balloon flight in the 1980s. Their properties have been well documented by Christe et al. (2008) and Hannah et al. (2008a,b). Precise measurement of their energy is not possible because of difficulties resolving the thermal and non-thermal components. Hannah shows that the distribution of thermal energies lies between $10^{21} - 10^{22}$ J and the

non-thermal somewhat lower. The loops studied have length scales which vary between 7 and 77 Mm. The widths have a range of $3 - 20$ Mm, shorter and much fatter than the kink instability cases discussed in this thesis. The average lifetimes of their loops are 5.4 minutes and vary between 2.2 and 15 minutes. Gordovskyy and Browning (2011) have also demonstrated that the kink instability in its evolved state can lead to mild particle acceleration, which seems to be what one is looking for in a microflare.

The second question is "what else can we do enhance the *Lare* code?". In our studies, we introduced the optically thin radiation into the *Lare* code and support the previous papers (e.g. Cargill, 1994; Cargill and Klimchuk, 2004; Sarkar and Walsh, 2008; Reale and Landi, 2012). However, the code is not able to fully resolve the radiation transfer with plasma temperature below $T = 2 \times 10^4$ K, since the plasma will become optically thick and partially ionisatised. In addition to this, the effects of transition region and gravity are also absent. The inclusion of these three effects should allow us to better resolve the physics. One must also pay attention to the coronal flux tube expansion. By the end of our simulations, the radii of the magnetic threads have expanded by about 50%. However, having observed 43 soft X-ray slowing evolving loops from Yohkoh, Klimchuk (2000) suggests that the flux tube expansion rate should be less than 30%.

The final question is "what else can we do improve our experiments?". We might use other magnetic configurations in our simulations: e.g. including a random photospheric motion at the boundaries of footpoints and the curvature of the coronal magnetic field. Such effects may change the dynamics of the MHD simulations. For example: it is uncertain whether the photospheric motion is a driver of the relaxation process. In our simulations, we have imposed an initial perturbation to the magnetic field in order to trigger the instability and relaxation process. One can argue that the initial perturbation is not good enough to represent the photospheric motions. In the *Lare* code, it is possible to apply a pre-determined velocity profile to the boundaries; therefore, we can choose the same magnetic configuration and then apply a rotating boundary condition to the footpoints of the thread. Such experiments will allow us to study the relationship between photospheric motion and the relaxation process. Note that a continuous photospheric motion may also alter the final state of the relaxation process and hence we may also be able to obtain a different temporal energy evolution depending on the choice of driver velocity. We could also try to model and reproduce some observational events by using a following modelling code for comparisons (see Section 6.6).

Chapter 6

Ongoing Future Works

In this section, we will discuss the new techniques used to analyse our data. Here, we will mainly focus on the methods related to magnetic topology (see Section 1.3.2).

6.1 Fieldline tracing and footpoint mapping

Coronal magnetic fields are anchored in the photosphere at the footpoints. If there is no photospheric motion and magnetic reconnection, the footpoints should remain at the initial position. In our simulations, the magnetic field lines are well twisted whilst line-tied at the photospheric ends, where all the velocity components vanish at the upper or lower boundary ($z = \pm 10$). In previous sections, we have shown that the kink instability is capable of triggering energy release, untwisting the field lines, creating current sheets and ultimately raising the temperature. In this section, we will present the development techniques to trace the field lines and see if this make it possible to identify the type of magnetic reconnection.

Recall the definition of our magnetic field. An equilibrium magnetic thread is placed at the centre of the computational domain with a zero net axial current. The thread is modelled by a straight twisted cylinder, with the cylinder's axis located at (x_0, y_0) with a smooth α profile. For $r^2 \leq 1$, the magnetic field components of each thread have the form

$$\begin{aligned} B_\theta &= B_0 \lambda r (1-r^2)^3, \\ B_z &= B_0 \sqrt{1 - \frac{\lambda^2}{7} + \frac{\lambda^2}{7}(1-r^2)^7 - \lambda^2 r^2 (1-r^2)^6}, \\ \alpha &= \frac{2\lambda (1-r^2)^2 (1-4r^2)}{B_z}, \end{aligned}$$

and for $r^2 > 1$, $B_\theta = 0, \quad B_z = B_0 \sqrt{1 - \frac{\lambda^2}{7}}, \quad$ and, $\quad \alpha = 0.$

With the definition of the magnetic field, we can calculate the location of the field lines and their footpoints analytically for the initial timestep. Using cylindrical coordinates, we have

$$x = r\cos\theta, \quad y = r\sin\theta, \quad r = \sqrt{x^2 + y^2}, \quad \theta = \tan^{-1}(y/x).$$

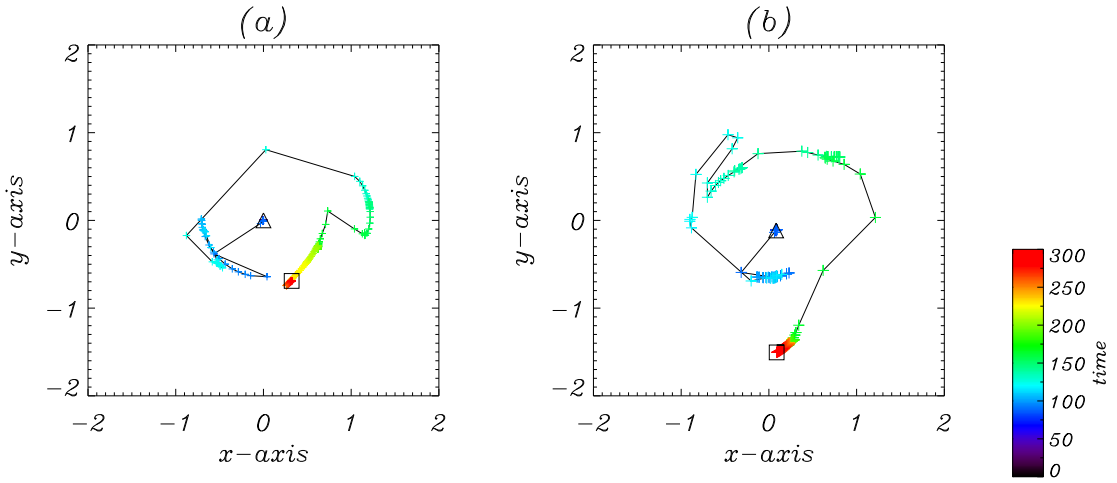

Figure 6.1: Case 17: The location of the footpoints mapped to the upper boundary (at $z = 10$) for two magnetic field lines during the simulation. The field lines are traced from starting points **(a)** $P_1(x, y, z) = (0, 0, -10)$ and **(b)** $P_2(x, y, z) = (0.1, 0.1, -10)$. The colour labels the location of the footpoint as a function of time, from the beginning of simulation ($t = 0$) by purple to the end of the simulation ($t = 300$) by red. The triangle and square symbols also indicate the beginning and end of the simulation.

and the position of a field line, $L(z = \pm 10)$, can be represented by

$$X = r\cos\left(\Phi(r) + \theta\right) \quad \text{and} \quad Y = r\sin\left(\Phi(r) + \theta\right),$$

where $\Phi(r) = L(z)B_\theta / rB_z$ is the pitch angle along the field line.

On the other hand, we use the 4th order Runge-Kutta method (RK4) to approximate the position of the field lines (in Case 17), starting from two locations: $P_1(x, y, z) = (0, 0, -10)$ and $P_2(x, y, z) = (0.1, 0.1, -10)$. The footpoints of these field lines are mapped to the upper boundary (at $z = 10$); and the results are shown in Figure 6.1. The locations of the footpoints are labelled by the "+" symbols and they are coloured according to time. The first and final times are also labelled by the triangle and square symbols respectively. The magnetic field lines and the footpoints remain at their initial locations until $t = 90$ (blue colour), until the kink instability is triggered. Then the footpoints begin to shift to other locations. It is also observed that the footpoints have drifted slowly, presenting arc-like structures over time. This behaviour is presumably due to numerical diffusion.

The location of footpoints in the upper boundary can also be plotted as a function of time. Figure 6.2 shows the location of the footpoint of a magnetic field line as functions of $x(t)$ and $y(t)$, where the field line is traced from $P_1(x, y, z) = (0, 0, -10)$. The plots show that the footpoint has remained at the initial position for a period. It then jumps six times in the x and y directions

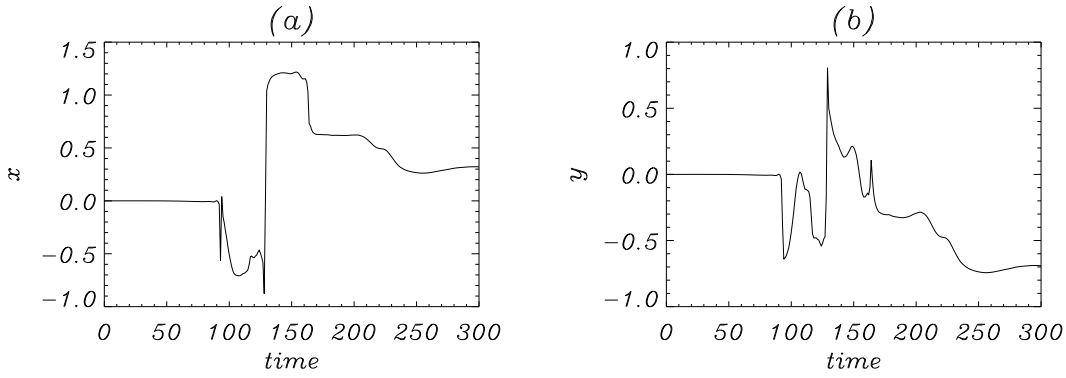

Figure 6.2: Case 17: The location of the end point of the field line (at $z = 10$) as function of time. The field line is traced from $(x, y, z) = (0, 0, -10)$.

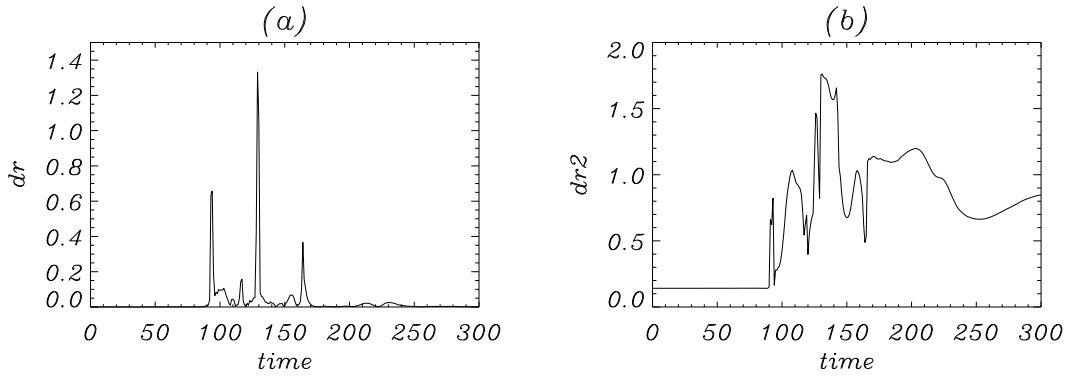

Figure 6.3: Case 17: **(a)** The distance travelled by the end point as a function of time and **(b)** the change of the distance between two end points of the field lines. The field lines are traced from $P_1(x, y, z) = (0, 0, -10)$ and $P_2(x, y, z) = (0.1, 0.1, -10)$.

between $t = 90$ and 150. This agrees with the evolution discussed in the previous section: a huge amount of magnetic energy is released in this period and followed by slow decay, indicative of magnetic reconnection taking place.

An alternative interpretation of this result is to calculate the distance travelled by the end point as a function of time. Here, we define the notation of the end point of the field lines traced from P_1 as P_1'. Then, we have

$$dr(t) = \sqrt{(P'_{1x}(t) - P'_{1x}(t-1))^2 + \left(P'_{1y}(t) - P'_{1y}(t-1)\right)^2}.$$

Figure 6.3(a) indicates that there are three major changes of displacement with dr occurring at time $t = 90$, 130 and 160. This can help us identify the times when magnetic reconnection occurs. We can also calculate the distance between the two end points between P_1' and P_2' (traced

from $P_1(x, y, z) = (0, 0, -10)$ and $P_2(x, y, z) = (0.1, 0.1, -10)$ respectively):

$$dr2(t) = \sqrt{\left(P'_{1x}(t) - P'_{2x}(t-1)\right)^2 + \left(P'_{1y}(t) - P'_{2y}(t-1)\right)^2}.$$

Figure 6.3(b) shows that the distance between the end points remains unchanged until the instability is triggered. It then shows the distance has changed rapidly as both of the end points move from $t = 90$ onwards.

6.2 Evolution along a field line

The mapping of footpoints in Case 17 (traced from $P_1(x, y, z) = (0, 0, -10)$) suggests that there were multiple magnetic reconnection events occurring before $t = 130$ (see Figures 6.2 and 6.3). Therefore, we can analyse the field line by investigating the variables as functions of the distance along the field line at three consecutive times, in order to show evidence of magnetic reconnection.

Figure 6.4 shows the parallel electric field and temperature along the field line for time $t = 128$ (*black solid* curves), 129 (*red dashed* curves) and 130 (*blue dotted-dashed* curves). The curves show that there are small peaks of parallel electric field at time $t = 128$ and 129. As discussed in Section 1.3.3.1, a parallel electric field arises where a current sheet is formed and it is an indication of magnetic reconnection. After the rise of $E_{\parallel}$, the plasma density and temperature curves show decreases (and increases) at the same position at the following timesteps.

6.3 Q-factor

In 3D reconnection, the presence of magnetic null points is not necessary. We have stated that reconnection can still occur at Quasi-Separatrix Layers (QSLs) and the connectivity of magnetic field lines will change rapidly. We describe this change by measuring the *degree of squashing*, Q.

To begin with, we consider the field line mapping in Cartesian coordinates from one photospheric footpoint to the opposite one as $R_- = (x_-, y_-, z_-) \rightarrow R_+ = (x_+, y_+, z_+)$ and the reverse one as $R_+ = (x_+, y_+, z_+) \rightarrow R_- = (x_-, y_-, z_-)$. These mappings can be represented by the vector functions $\left(X_-\left(x_+, y_+\right), Y_-\left(x_+, y_+\right)\right)$ and $\left(X_+\left(x_-, y_-\right), Y_+\left(x_-, y_-\right)\right)$ respectively.

The Norms, $N(R_+)$ and $N(R_-)$, of the respective Jacobian matrix (Priest and Démoulin, 1995; Demoulin et al., 1996) are:

$$N\left(R_\pm\right) = \sqrt{\left(\frac{\partial X_\mp}{\partial x_\pm}\right)^2 + \left(\frac{\partial X_\mp}{\partial y_\pm}\right)^2 + \left(\frac{\partial Y_\mp}{\partial x_\pm}\right)^2 + \left(\frac{\partial Y_\mp}{\partial y_\pm}\right)^2} \equiv N_\pm. \tag{6.1}$$

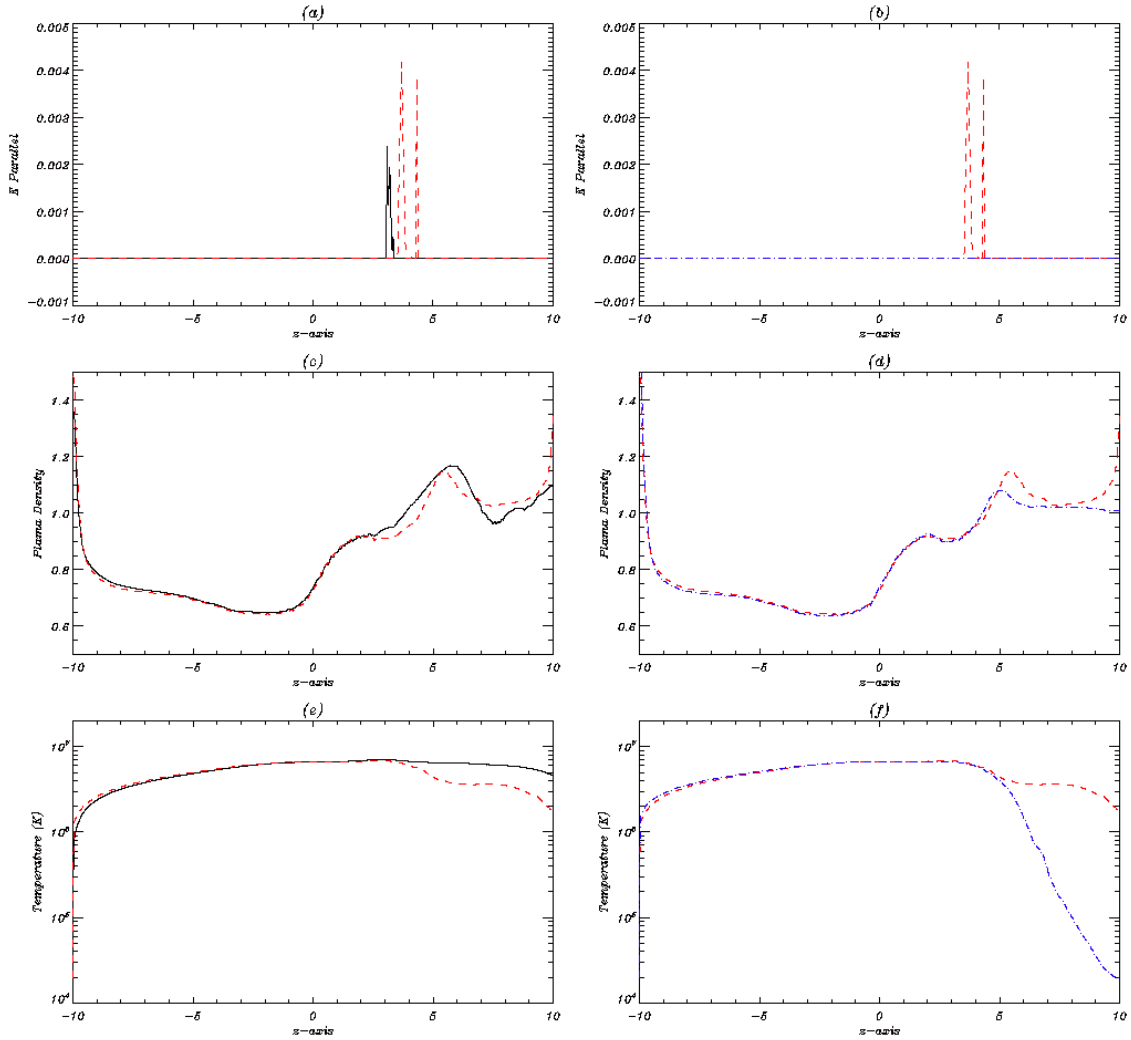

Figure 6.4: Case 17: The plots of parallel electric field (top row), plasma density (middle row) and temperature (bottom row) along a field line traced from $(x, y, z) = (0, 0, -10)$ for three consecutive times. In the left-hand column, it details the magnetic field line at time $t = 128$ (by *black solid* curves) and 129 (*red dashed* curves); in the right-hand column, it details the field line for $t = 129$ (*red dashed* curves) and 130 (by *blue dotted-dashed* curves).

It is proposed that if this quantity is $N(R_{\pm}) \geq 1$, then it defines the field lines which map the footpoints in a QSL. However, a problem occurs if $|B_{n^+}| \neq |B_{n^-}|$, i.e. $N(x_+, y_+) \neq N(x_-, y_-)$. This means there is no unique condition to define a QSL. A slightly more complicated expression is introduced by Titov et al. (2002) to solve this problem,

$$Q_{\pm} = \frac{N_{\pm}^2}{\left|B_{n^{\pm}}/B_{n^{\mp}}^*\right|} \equiv Q_{\mp}^* = \frac{N_{\mp}^{*2}}{\left|B_{n^{\mp}}^*/B_{n^{\pm}}\right|} \equiv Q. \tag{6.2}$$

We refer to the value of Q in the QSLs as the *Q-factor*. This function indicates that $x_{\mp}$ and $y_{\mp}$ are substituted on $X_{\mp}(x_{\pm}, y_{\pm})$ and $Y_{\mp}(x_{\pm}, y_{\pm})$ respectively.

Both the norm and the Q-factor are dimensionless variables and characterise QSL reconnection in the same way. The rate of change of their values is directly proportional to the shift of the footpoints. Therefore, high values of Q indicate the occurrence of reconnection and current sheet formation.

In our studies, we are attempting to simulate the energy released from coronal magnetic fields where the footpoints are anchored on the photosphere and governed by relaxation processes. We have restricted our simulations to line-tied magnetic threads with the field lines stretched between two boundaries. In this system, the magnetic fields are always continuous in volume without the presence of magnetic null points. Therefore, the type of magnetic reconnection in our studies is likely to be QSL reconnection.

Here, we recall the definitions of the Norm (Eq. 6.1) and Q-factor (Eq. 6.2). Since the definition of the Norm is just a simple derivative, we can compare the analytical result with the simulation data at the initial stage. For simplicity, we use cylindrical coordinates. The Norm can be rewritten as

$$N = \sqrt{\left(\frac{\partial X}{\partial r}\right)^2 + \left(\frac{1}{r}\frac{\partial X}{\partial \theta}\right)^2 + \left(\frac{\partial Y}{\partial r}\right)^2 + \left(\frac{1}{r}\frac{\partial Y}{\partial \theta}\right)^2} = \sqrt{2 + r^2\left(\frac{\partial \Phi}{\partial r}\right)^2},$$

where the position of the field lines are

$$X = r\cos\left(\Phi(r) + \theta\right) \quad \text{and} \quad Y = r\sin\left(\Phi(r) + \theta\right),$$

and $\phi(r) = L(z)B_\theta / rB_z$ is the pitch angle along the field line. In the event of footpoint mappings, $X_\pm$ and $Y_\pm$ denote the locations of the footpoints of the field lines at the boundary as $L(z = -10) = 0$ and $L(z = 10) = 20$.

Figure 6.5 shows the nature of the Norm when the magnetic field of Case 17 (which included both thermal conduction and optically thin radiation effect) is in an initial equilibrium. Figure 6.5(a) shows the Norm has a smooth ring structure. The high value of the norm near the edge of the loop radius is due to the fact that the magnetic loop is twisted, hence the footpoints of the field lines do not map at exactly at the same position for $X_\pm$ and $Y_\pm$. Next, we calculate the value of the Norm analytically along $y = 0$ to determine the accuracy of the numerical results. In (b), the numerical data are represented by the solid curve and the analytical result is the dashed curve. The curves match very well except near the maximum value of the peaks. These differences are probably due to truncation error or due to lack of resolution while the field lines are being traced.

Figure 6.6 shows the contour plots of Q-factors for four different times. At time $t = 0$, the plot has basically the same structure as the Norm plot in Figure 6.5(a), except that the maximum increases to $Q_{max} = 2250$. At time $t = 90$, the instability begins to rise and the Q-factors begin

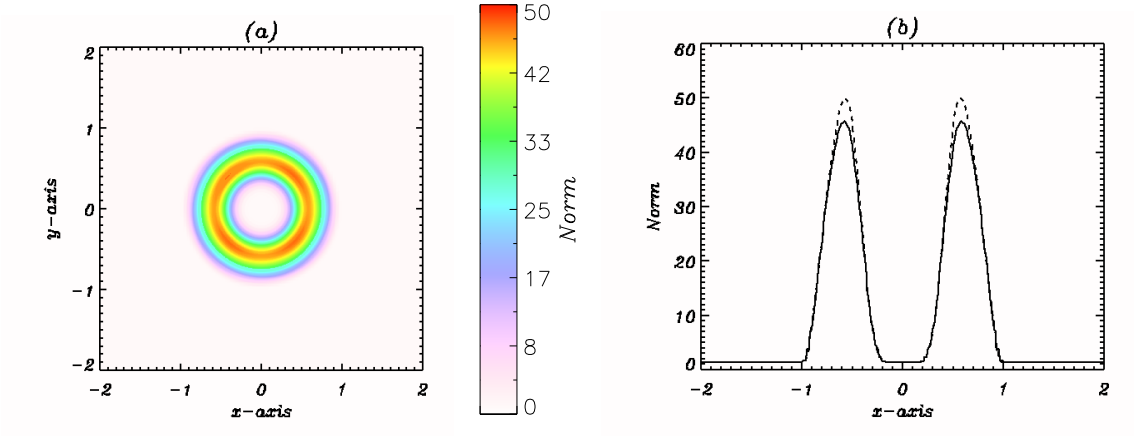

Figure 6.5: Case 17: The contour plot of the Norm at time $t = 0$. **(a)** shows the results as contour plots and **(b)** shows the results as a function of x at $y = 0$. The solid curve denotes the numerical result of the Norm and the dashed curve is the analytical result.

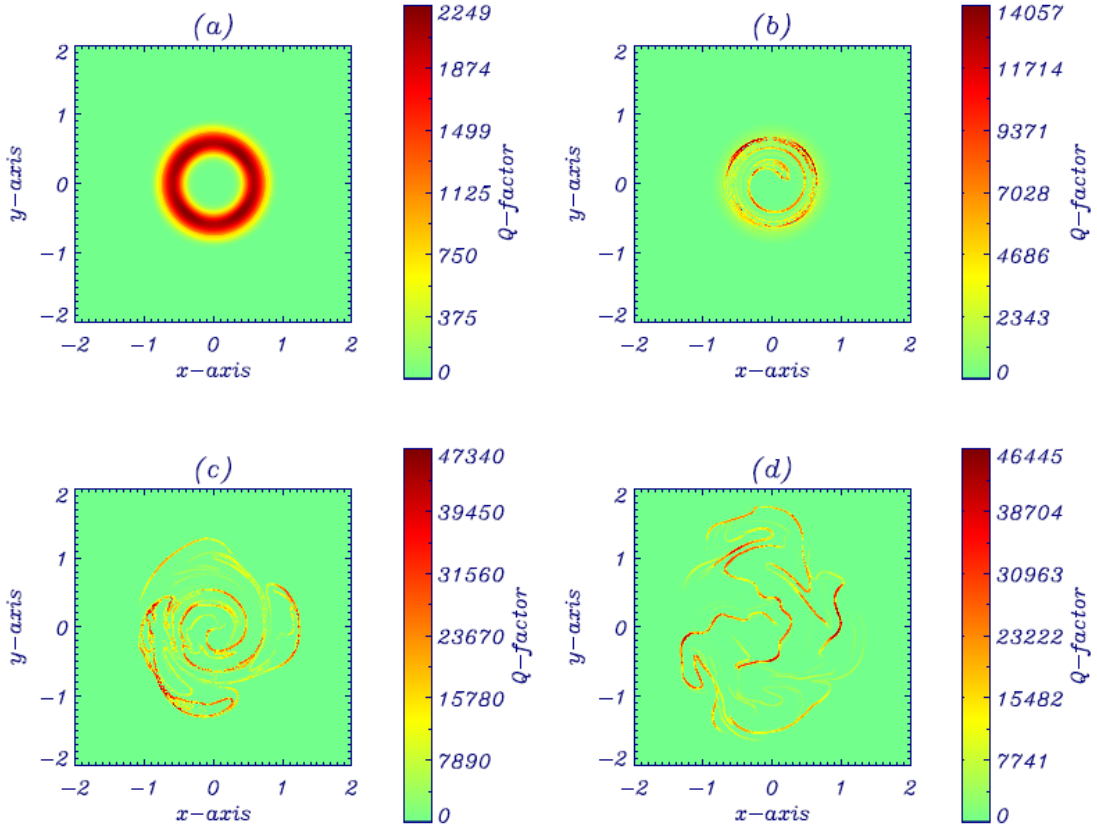

Figure 6.6: Case 17: The contour plots of Q-factors for four different times: **(a)** $t = 0$, **(b)** $t = 90$, **(c)** $t = 130$ and **(d)** $t = 300$.

to form a vortex structure with an increasing value of $Q_{max} = 1.4 \times 10^4$. During the simulation, the Q-factor plots show an untwisting and expanding nature, which we can also observe from the current sheet formation. Note that the maximum value of Q continues tp rise as the instability develops. The $Q_{max} = 4.7 \times 10^4$ at $t = 130$ and then the structure spreads further and reduces slightly to $Q_{max} = 4.6 \times 10^4$ at $t = 300$. This indicates that the field lines are untwisted and the footpoints are located at different locations.

6.4 Multiple threads

The footpoint mapping method can also provide evidence of reconnection in the avalanche events. Here, we recall the simulation result of Case 9, where an unstable thread in the right-hand side domain was able to destabilise a neighbouring thread on the left, subsequently, the two threads combined to form a single larger structure. We can use the same method to trace the footpoints of the field lines. Figure 6.7 presents a mapping of four field lines. The field lines are traced from the footpoints started from (a) $P_1(x, y, z) = (-0.7, 0.3, -10)$, (b) $P_2(x, y, z) = (-0.7, -0.3, -10)$, (c) $P_3(x, y, z) = (-1.3, 0.3, -10)$ and (d) $P_4(x, y, z) = (-1.3, -0.3, -10)$ and anchored at the upper boundary (where $z = 10$). Two of these field lines are traced from the right-hand side thread and two more from the left-hand side thread, where the threads are touching each other at $x = -1$. The remarkable result from this figure is that these field lines did cross over and reconnect with the neighbouring threads and anchored their footpoints in the opposite sides during the simulation. We can also see that such field lines may reconnect to the original side in some cases.

In order to have a better understanding of the whole system, we trace and map all the field lines for each grid and interpret the result with a graphical colour mapping method. Figure 6.8 presents the colour maps for (a) the lower boundary $z = -10$ and (b) the upper boundary $z = 10$ at the end of the simulation. Every grid cell $R_- = (x_0, y_0)$ on the lower boundary is given one of the four colors according to the field line mapping to the upper boundary $R_+ = (x_0, y_0)$. We split the domain into two parts (left-hand region, $-4 \leq x \leq -1$ and right-hand side region, $-1 \leq x \leq 2$) and focus on the regions where the unstable equilibrium threads are located. For the lower boundary map (see Figure 6.8(a)), we use green if the footpoints of the field lines remain on the left-hand and red if they map to the opposite side; we use yellow if the footpoints remain on the right-hand side and blue if they map to the opposite side. As a current sheet begins to form in the right-hand side thread, its field lines expand and combine with the left-hand side thread. A related image of this mapping is shown in Figure 6.8(b) for the upper boundary. The colours of blue and red show where the footpoints have ended up. Both are sharply divided at the middle, can be seen to spread and are anchored relatively far away from the middle. The mapping technique shows that 15.5% of the field lines (blue colour area) have been reconnected and anchored in the opposite side and 15.3% of the field lines (red colour area) are mapped to the opposite side. This

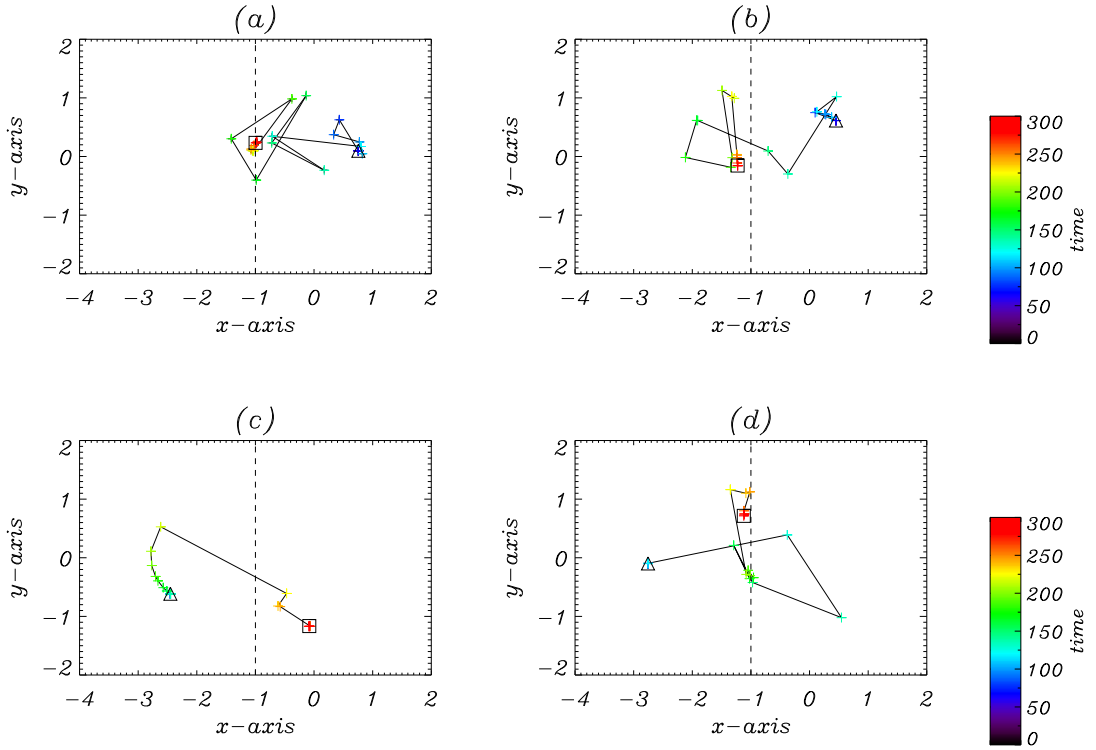

Figure 6.7: Footpoints mapping (to $z = 10$) for Case 9. The field lines are traced from **(a)** $P_1(x, y, z) = (-0.7, 0.3, -10)$, **(b)** $P_2(x, y, z) = (-0.7, -0.3, -10)$, **(c)** $P_3(x, y, z) = (-1.3, 0.3, -10)$ and **(d)** $P_4(x, y, z) = (-1.3, -0.3, -10)$. The colour labels the location of the end point as a function of time, from the beginning of simulation ($t = 0$) by purple to the end of the simulation ($t = 300$) by red. The triangle and square symbols also indicate the beginning and the end of the simulation.

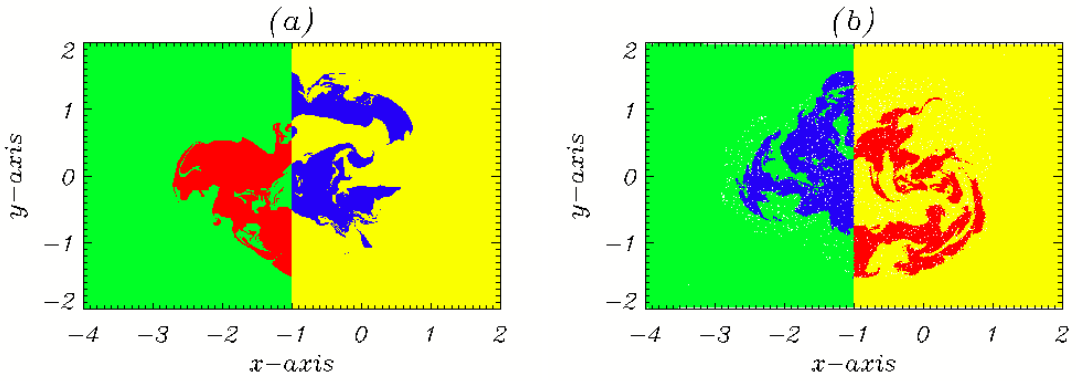

Figure 6.8: $t = 300$: Colour maps of the footpoints of Case 9 for **(a)** the lower boundary $z = -10$ to **(b)** the upper boundary $z = 10$. The yellow and green colours indicate footpoints of the field lines staying in the same side of computational domain, while the blue and red colours indicated the footpoints of the field lines anchoring to the opposite side.

difference is very small, which should be correct because the conservation of fluxes should be equal within numerical accuracy.

This colour mapping method clearly proves reconnection for multiple thread cases. However, this method does not take all field lines into account. Those field lines which start and end in the same sides of the domain, but cross sides along the way, are not consider and thus another kind of topological function is also studied.

6.5 Curl of $\mathcal{A}$ function

Curly $\mathcal{A}$ function is a topological quantity introduced by Yeates and Hornig (2013). It can be applied to any non-zero and line-tied magnetic field while its field lines are connected between two boundaries. The topological flux function is a scalar function involving the integral of the relative magnetic helicity. It is slightly different from the Q-factor, which only calculates the degree of squashing between the two boundaries. This method provides a unique characteristic of the whole magnetic field.

To begin with, we use a similar notation as before, where the magnetic field B is defined by $V = \{(r, \phi, z); -10 \leq z \leq 10; 0 \leq r \leq R\}$. The field line mapping is a function $f(x_0, y_0; z)$, which denotes the location of a point along the z-axis on the field line traced from one side of the boundary to the opposite side using Euler's Method. Here (x_0, y_0) is the same as in previous sections, where $X_- = (r_-, \phi_-, z_-)$ at the $z = -10$ boundary.

Then the topological flux function is

$$\mathcal{A}(x_0, y_0) = \int_{z=-10}^{z=+10} \mathbf{A} \cdot d\mathbf{l} = \int_{-10}^{+10} \frac{\mathbf{A}\left(f(x_0, y_0; z)\right) \cdot \mathbf{B}\left(f(x_0, y_0; z)\right)}{B_z\left(f(x_0, y_0; z)\right)} dz,$$

where $\mathbf{A}$ is the vector potential along the magnetic field lines (i.e. $\mathbf{B} = \nabla \times \mathbf{A}$). It has a direct relationship with magnetic helicity (see Eq. 1.17). We use cylindrical coordinates to obtain

$$\begin{aligned} H &= \int_V \mathbf{A} \cdot \mathbf{B}\, dV = \int_V \mathbf{A}(r, \phi, z) \cdot \mathbf{B}(r, \phi, z)\, r\, dr d\phi dz \\ &= \int \mathbf{A}\left(f(x_0, y_0; z)\right) \cdot \mathbf{B}\left(f(x_0, y_0; z)\right) \frac{B_z(x_0, y_0)}{B_z\left(f(x_0, y_0; z)\right)} dx_0 dy_0 dz \\ &= \int_{z=-10} \mathcal{A}(x_0, y_0) B_z(x_0, y_0)\, dx_0 dy_0, \end{aligned}$$

substituting the variables of $(r, \phi, z) = f(x_0, y_0; z)$ where $x_0 = (r_-, \phi_-, z_-)$ is the footpoint of the field line along (r, ϕ, z) at the $z = -10$ boundary. $\mathbf{A}$ is a probability density function of H, hence, can highlight the relaxation process.

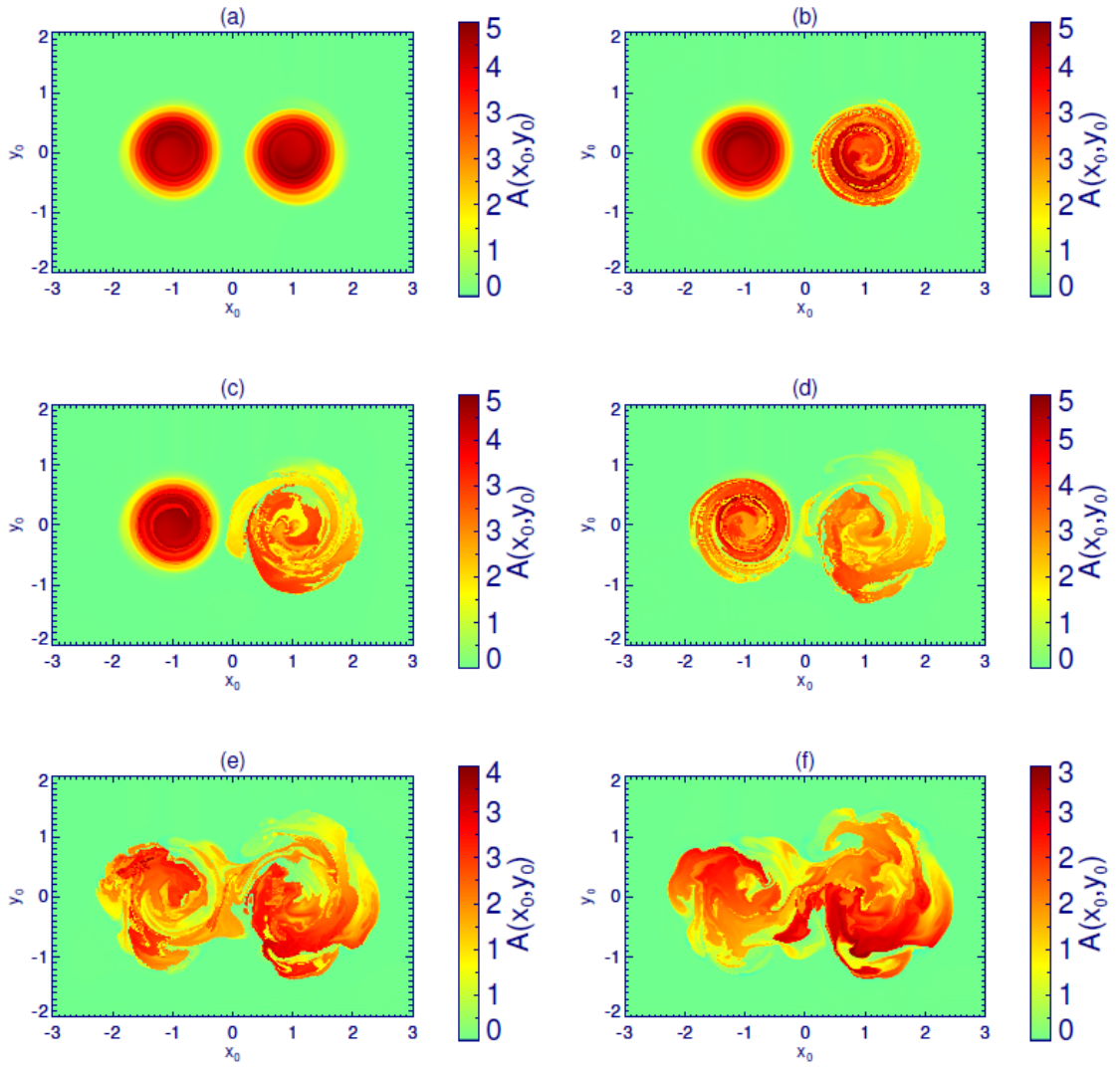

Figure 6.9: The topological flux function $\mathcal{A}$ in a two-thread simulation for different times: **(a)** $t = 0$, **(b)** $t = 90$, **(c)** $t = 120$, **(d)** $t = 150$, **(e)** $t = 200$ and **(f)** $t = 300$ (from left to right, top to bottom).

Figure 6.9 shows an example of the topological flux function $\mathcal{A}$ in a two-thread simulation. In this case, the configurations, such as the computational domain and magnetic instability, are basically the same as the ones defined in Case 9 except that the threads are centred at different locations $x = -1$ and $x = 1$ and have been run at a lower resolution of $320 \times 160 \times 320$. It shows that at time $t = 0$, the topological flux function $\mathcal{A}(x_0, y_0)$ of the magnetic threads displays two vortex structures with darker colour near the centre. The minimum and maximum values of the $\mathcal{A}(x_0, y_0)$ are about 0 and 5, as indicated by the legend. The vortex structure in the right-hand side thread begins to deform at about $t = 90$, as the kink instability is triggered. As discussed earlier in this thesis, the field lines in the thread begin to untwist, together with current sheet formation and release of magnetic energy. This thread and its field lines then expand and untwist to the nearby

region. At $t = 120$, a tail is beginning to appear from the right-hand side near $x = 0$, the colour shows that the value of $\mathcal{A}(x_0, y_0)$ is slightly above two and the maximum value of the $\mathcal{A}(x_0, y_0)$ in the right-hand side is reduced to about 3. At time $t = 150$, as the evolution continues, it appears that the tail from the right-hand thread is then attached to the left-hand side thread. The figure also shows that the vortex structure on the left is deforming as well. Throughout the simulation, both threads are deformed as they are relaxing towards their minimum energy states. It is clear that the value of $\mathcal{A}(x_0, y_0)$ is reduced to less than 3 and high connectivity is observed around $x = 0$. This indicates that the two threads are reconnected with each other at $x = 0$ and the field lines are untwisting and relaxing towards the minimum energy status.

6.6 Forward Modelling

Forward modelling can be used to investigate the differences between the results produced by simulations and the observational data, such as TRACE, SOHO/CDS and Hinode/EIS. These kind of comparisons can help us to develop a better understanding of how the theoretical results compare to the real phenomena. The results generated by our simulations are expressed in terms of magnetic pressure, density, temperature, energy and so on, which cannot be compared directly with observational data. The best way is to calculate the intensity perturbations of plasma temperature at around 1 MK from the density and temperature perturbations. Observational signatures of the coronal heating by nanoflares have been detailed by many authors, such as Cargill (1993, 1994), Cargill and Klimchuk (1997, 2004), Klimchuk and Cargill (2001), Bradshaw and Cargill (2006, 2010) and De Moortel et al. (2008).

In this section, we use the code provided by De Moortel and Bradshaw (2008). The synthesised emission is calculated by the combination of ionisation balance, solar coronal abundances and ion emissivities. It is done by reading the emissivities from the emission table with the given temperature and number density, using the basic linear interpolation method. The code will return the emission result as the intensity perturbations of plasma at temperature around 1 MK

$$I(z) \quad = \quad \frac{0.83 \times A \times d \times B(T_e(z)) \times R(\lambda) \times E(\lambda, n_e(z), T_e(z)) \times \lambda}{n_e(z) h c 4\pi}$$

in units of DN cm^6 pixel^{-1} s^{-1}; where I is the intensity perturbation, T_e the temperature and n_e the number density as functions of z (the position of these variables along the z-axis). 0.83 is the ratio of protons to electrons, A is the abundance of the relevant ion relative to hydrogen, d is the line-of-sight depth in the y-axis, B is the ionisation balance, R is the instrument response function which depends on a chosen wavelength (λ), E is the emissivity, h is the Planck's constant and c is the speed of light. In addition to these, we need to bear in mind that the look-up table for the relevant ions requires the variables of temperature and number density in the form of a logarithm.

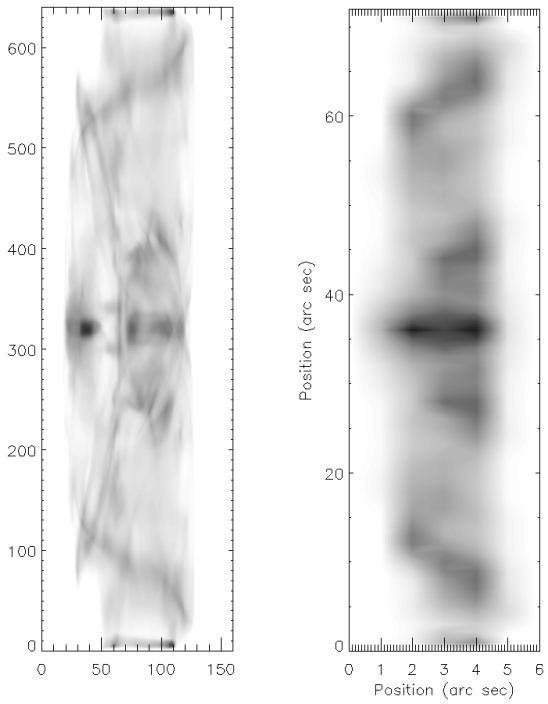

Figure 6.10: The plasma with temperature about 1 MK can be seen using the *TRACE* 171 Å filter. These figures are produced with data from a test case at $t = 200$. This case excludes the effects of thermal conduction and optically thin radiation. *Left*: the line-of-sight integrated intensity function; *Right*: the spatially averaged function.

In our studies, we focus our attention on the emission lines which are comparable with the TRACE 171 Å filter data. This limits the choice of the above variables.

Figure 6.10 shows the forward modelling result from a test case at $t = 200$, which is about the same time the decay of magnetic energy becomes significantly slower. In this case, the configuration of the magnetic field is the same as Case 5, except that the resolution is changed to $160^2 \times 640$. The figure on the *left* shows the hot plasma in the magnetic field with temperture about 1 MK. It is given by the intensity function, $I(z)$, integrated along the line-of-sight from the simulation result. The spatially averaged function is shown on the *right* with a smoothed resolution to present the observational signatures to match up with the *TRACE* 171 Å filter. In this figure, we are still able to observe a helical structure, however, we do not usually see these structures from observation. Recently, Botha et al. (2011, 2012) have conducted studies of the thermal conduction effect in coronal magnetic fields and subsequently applied the forward modelling method to obtain the observational signatures which agrees with the theories. In the future, we could also conduct a similar study with the inclusion of both thermal conduction and optically thin radiation effects when we have a better understanding of the forward modelling code.

Appendix A

A Brief Explanation Of The Time Splitting Method

The time splitting method is accurate at least to first order in time. If we consider the change of total energy as a sum of energy sources and sinks (e.g. Eq. (1.12): coronal heating functions, thermal conduction and optically thin radiation), then we can consider the change of energy as the combination of different energy terms. For example,

$$\frac{\partial e}{\partial t} = F_1(e) + F_2(e) + F_3(e).$$

where

$$\begin{aligned} F_1(e) &= H_0 + j^2/\sigma + H_v, \\ F_2(e) &= \nabla \cdot (\kappa_{\|} \nabla T, \\ F_3(e) &= -\rho \chi T^{\alpha}). \end{aligned}$$

The change of energy at a small timestep, δt, under the first energy function is given by

$$\begin{aligned} \frac{e^* - e^n}{\delta t} &= F_1(e^n), \quad \text{thus,} \\ e^* &= e^n + \delta t \, F_1(e^n). \end{aligned} \tag{A.1}$$

Then, applying the same method to the next energy function we obtain:

$$\frac{e^{**} - e^*}{\delta t} = F_2(e^*). \tag{A.2}$$

By substituting Eq. (A.1) into the Eq. (A.2), it can be rearranged again to

$$\begin{aligned} e^{**} &= e^* + \delta t \, F_2(e^*), \\ &= e^n + \delta t \, [F_1(e^n) + F_2(e^n)] + \delta t^2 \, F_1(e^n) F_2'(e^n), \\ &= e^n + \delta t \, [F_1(e^n) + F_2(e^n)] + O(\delta t^2). \end{aligned}$$

We then repeat the same process step by step until the last energy function. The energy for the next timestep is then given by

$$\frac{e^{n+1} - e^{**}}{\delta t} = F_3(e^{**}),$$

and, hence,

$$e^{n+1} = e^n + \delta t \ [F_1(e^n) + F_2(e^n) + F_3(e^n)] + O(\delta t^2).$$

This confirms that the time splitting method is at least a first order accurate method.

Appendix B

Miscellaneous Numerical Results

Here we show the results of our extra simulations, which were not presented in Chapter 4. We have rerun the simulations of Cases 14-19 again with an increase in the length scale of the radius by a factor of 20. Such a configuration will enhance the Alfvén timescale by 20 times and the conduction timescale by 400 times. (see Section 4.2.4). Therefore, conduction will have less effect on the evolution and we will be able to see if optically thin radiation becomes more important. A summary of the six cases are:

Case 14b: An unstable equilibrium thread without the thermal conduction and optically thin radiation effects, this is our reference case.

Case 15b: Only the thermal conduction effect is included.

Case 16b: Only the optically thin radiation effect is included.

Case 17b: Both thermal conduction and optically thin radiation are included.

Case 18b: Both thermal conduction and optically thin radiation are included and the initial density is increased by a factor of two.

Case 19b: Both thermal conduction and optically thin radiation are included and the initial density is increased by a factor of three.

Figure B.1 shows that once the length scale (i.e. timescale) is increased, thermal conduction reacts differently compared to the previous results (Figures 4.1(c) and 4.2(c)). The blue curve for Case 15b shows that the volume integrated internal energy takes the same path as in Case 14b until time $t = 1800$ s, followed by an further increase. It indicates that more plasma is heated by conduction along field lines. This agrees closely with Cargill (1994) who pointed out that thermal conduction can play a significant heating role over a longer timescale. However, the extra heating by conduction does not last long, in fact, the internal energy begins to level off when the magnetic field is relaxing towards a minimum energy state. Next, by comparing the red (for Case 16b) and purple (for Case 17b) curves, we can see that the new evolutions are dominated by optically thin radiation. The curves begin to decrease by similar rates from $t = 1800$ s onwards and also finished with roughly the same values by the end of the simulations. Figure B.1(b) also demonstrates the

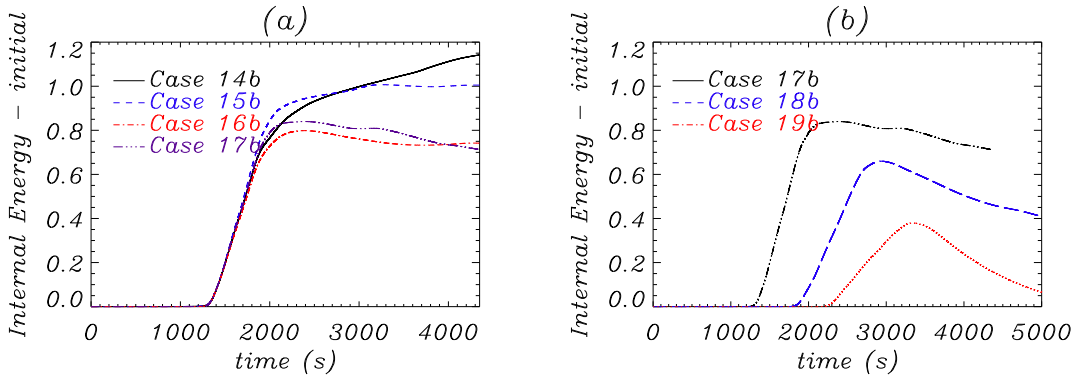

Figure B.1: The volume integrated internal energies as function of time (in real units) for **(a)** Case 14b-17b and **(b)** Cases 17b-19b. All of these cases have an initial temperature of 2×10^4K and have their length scales enhanced by a factor of 20.

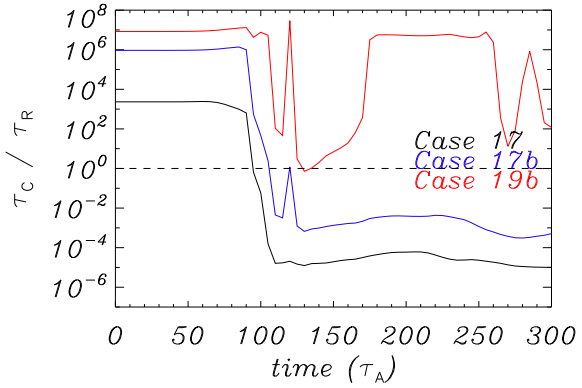

Figure B.2: The timescale plots of the plasma at the centre of the domain, i.e. $x = y = z = 0$, for Case 17 in Section 4 (*black*), Case 17b (*blue*) and Case 19b (*red*). The individual figures are **(a)** conduction time/Alfv́en time, **(b)** radiation time/Alfv́en time and **(c)** conduction time/radiation time. The Alfv́en travel time of Cases 17, 17b and 19b are $\tau_A = 0.72$, 14.50 and 25.11 seconds.

increase of density also increases the Alfvén timescale and the size of optically thin radiation for Cases 18b and 19b.

The key result we have obtained is: in a shorter timescale, optically thin radiation is not important compared to thermal conduction; thermal conduction can effectively reduce the maximum temperature and smooth the temperature along the magnetic field lines; and in the cases of longer timescale (and high plasma density), optically thin radiation will become more important and efficiently cool down the plasma. In Figure B.2, we can see that the ratio of the conduction and radiation timescales, τ_C/τ_R, begins to rise closer to unity in Case 17b (and well above unity in Case 19b) as the radiation effect becomes more and more important compared to the thermal con-

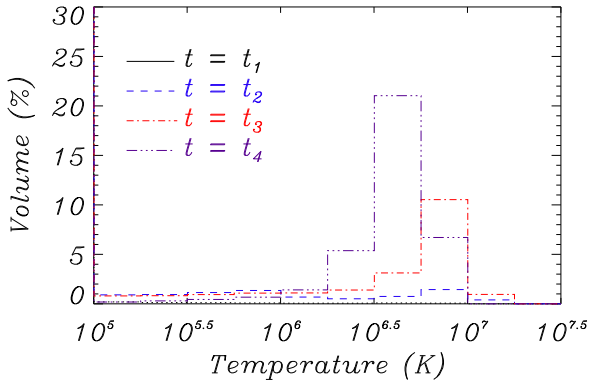

Figure B.3: The temperature distribution by histogram for Case 17b for different times. Time $t_1 = 1305$ s is shown as black solid, $t_2 = 1445$ s as blue dashed, $t_3 = 1885$ s as red dotted-dashed and $t_4 = 4350$ s as purple triple dotted-dashed.

duction. A small spike is also seen at $\tau_R = 120$ for both Cases 17b and 19b, which shows that optically thin radiation suddenly becomes important as it is at the same time as a strong current sheet is formed and the plasma temperature begins to rise to a higher level.

The temperature histogram (Figure B.3) also indicates that the volume of plasma temperature has dropped even further between the 10^5 K $\leq T < 10^6$ K region (compare to Case 17). This decrease is believed to be introduced by the enhancement of optically thin radiation. It seems that thermal conduction also plays a role in spreading the heat. The volume of hot plasma with temperature between $10^6 - 10^{6.5}$ K has been redistributed over the hotter region between $10^{6.25} - 10^7$, especially at time $t = 4350$ s. We will present further temperature plots to support these arguments.

The velocity histograms (Figures B.4 and B.5) indicate that when the timescale is increased, the velocity in the parallel direction is also increased. The volume of plasma with speed between $10^4 - 10^{4.25}$ m s^{-1} has decreased by about 5% (compare to Case 17), while the volume between the ranges $10^{4.5} - 10^{4.75}$ m s^{-1} and $10^{4.75} - 10^5$ m s^{-1} has been increased by about 12% and 6%, respectively. This suggests that the plasma has a higher velocity while conducting heat along the field lines. Indeed, the plasma density histograms, Figure B.6(a), show that the volume of the grid cells, which have a plasma density between $0.9 - 1$, has been reduced by 10%, while the volume of regions with lower plasma density (density range from $0.5 - 0.8$) have increased. The velocity-temperature scatter plot in Figure B.6(b) also shows that the majority of the plasma vanished at the lower temperature ($10^5 - 10^6$ K).

More figures are also presented for Cases 14b-17b. These figures demonstrate the evolutions in different temperature ranges and indicate when thermal conduction and optically thin radiation

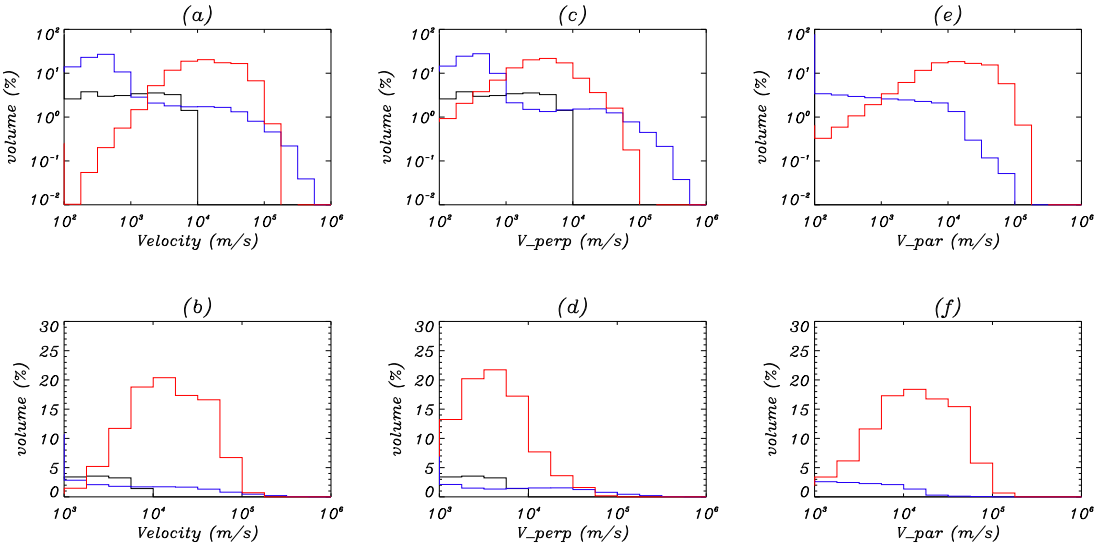

Figure B.4: The velocity distribution by histogram for Case 17b for five different times. Time $t_0 = 0$ s is shown as black, $t_1 = 1305$ s is shown as blue and $t_4 = 4350$ s as red. The left column is for the velocity magnitude, the middle column is the magnitude of the velocity perpendicular to the magnetic field and the right row is the magnitude of the velocity parallel to the magnetic field.

become the leading cooling effect. For example, in Cases 14b-17b, in which the length scale is enhanced (Figure B.8), optically thin radiation is more efficient for reducing the heat at the temperature range between $10^5 - 10^6$ K. Optically thin radiation is also important around $6 \times 10^6 - 10^7$ K in Case 17b. If the length scale is shorter (e.g. Case 17), Figure 4.8 shows that optically thin radiation does nothing except at the temperature range between $10^5 - 10^6$ K and thermal conduction plays an important role at all temperature ranges.

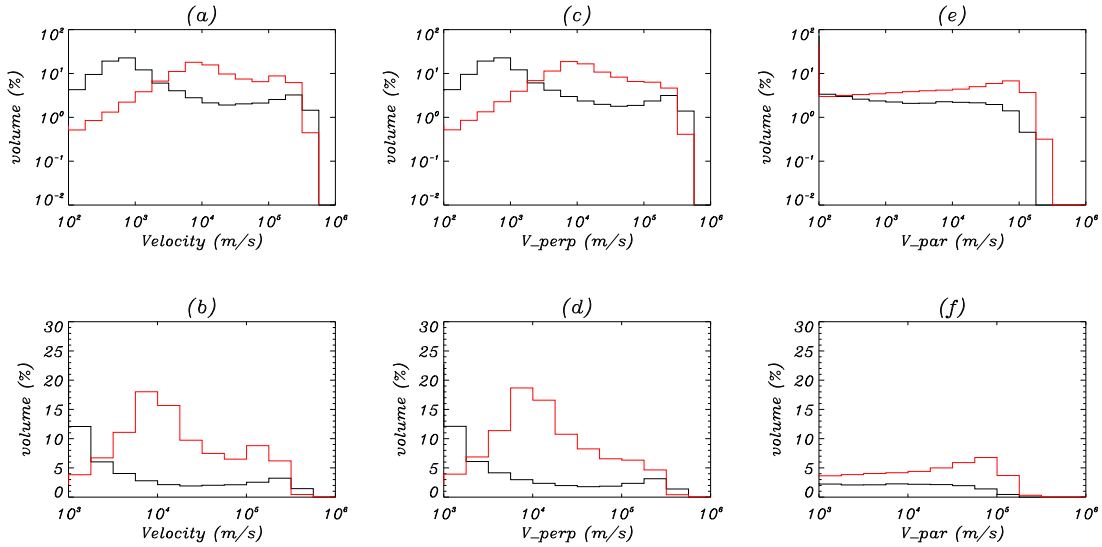

Figure B.5: The velocity distribution by histogram for Case 17b for five different times. Time $t_2 = 1445$ s is shown as black and $t_3 = 1885$ s is in red. The left column is for the velocity magnitude, the middle column is the magnitude of the velocity perpendicular to the magnetic field and the right row is the magnitude of the velocity parallel to the magnetic field.

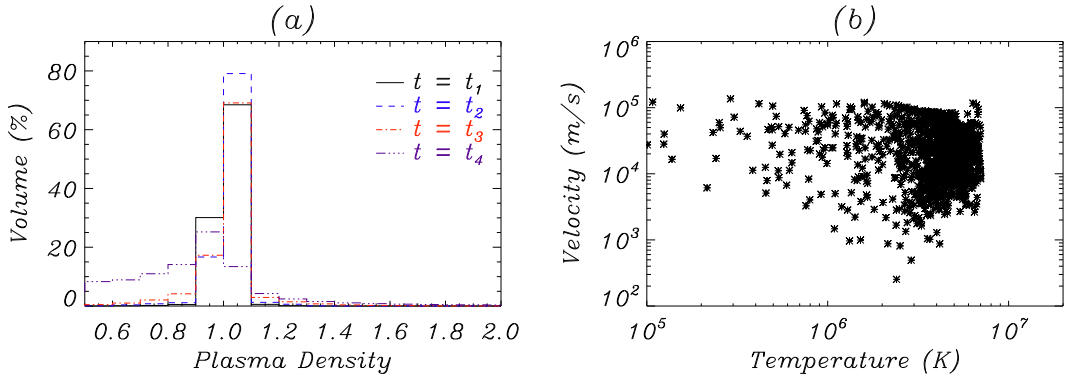

Figure B.6: **(a)** The density histogram (in dimensionless units) for Case 17b for different times. Time $t_1 = 1305$ s is shown as black solid, $t_2 = 1445$ s as blue dashed, $t_3 = 1885$ s as red dotted-dashed and $t_4 = 4350$ s as purple triple dotted-dashed. **(b)** is the log-log plot of temperature against velocity for $t_4 = 4350$ s.

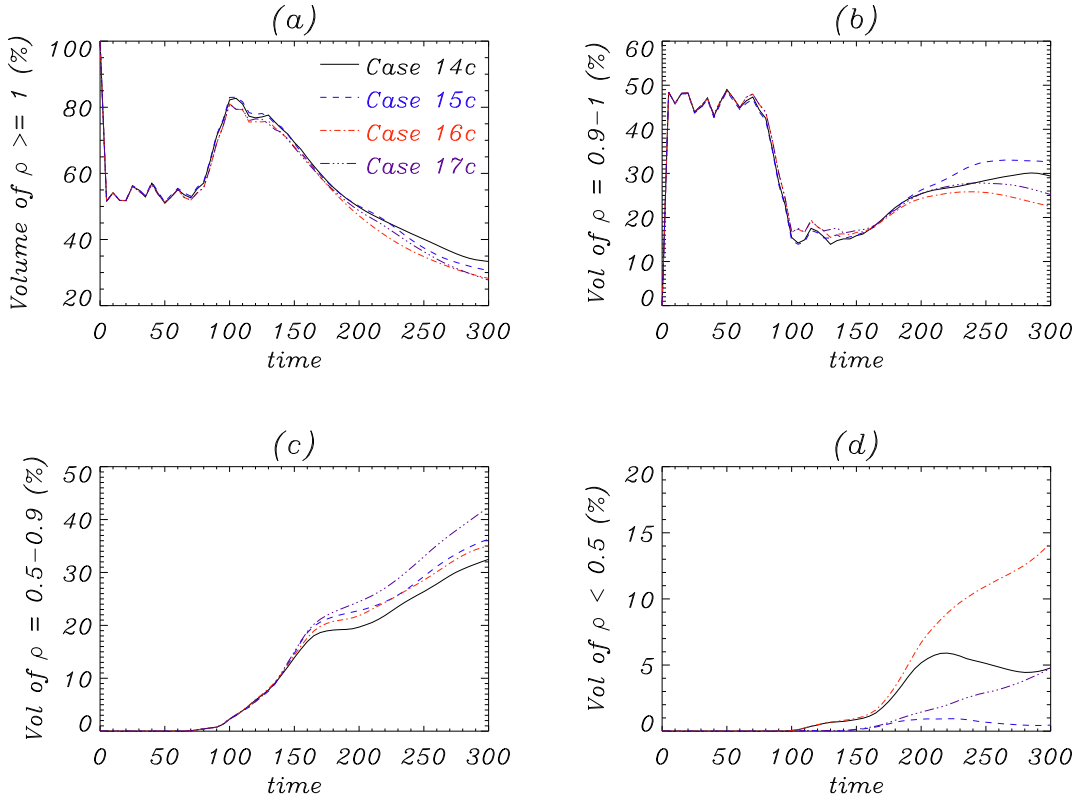

Figure B.7: The volume of cells over a certain range of plasma density for Cases 14c-17c, where **(a)** $\rho \geq 1$, **(b)** $0.9 \leq \rho < 1$, **(c)** $0.5 \leq \rho < 0.9$ and **(d)** $\rho < 0.5$.

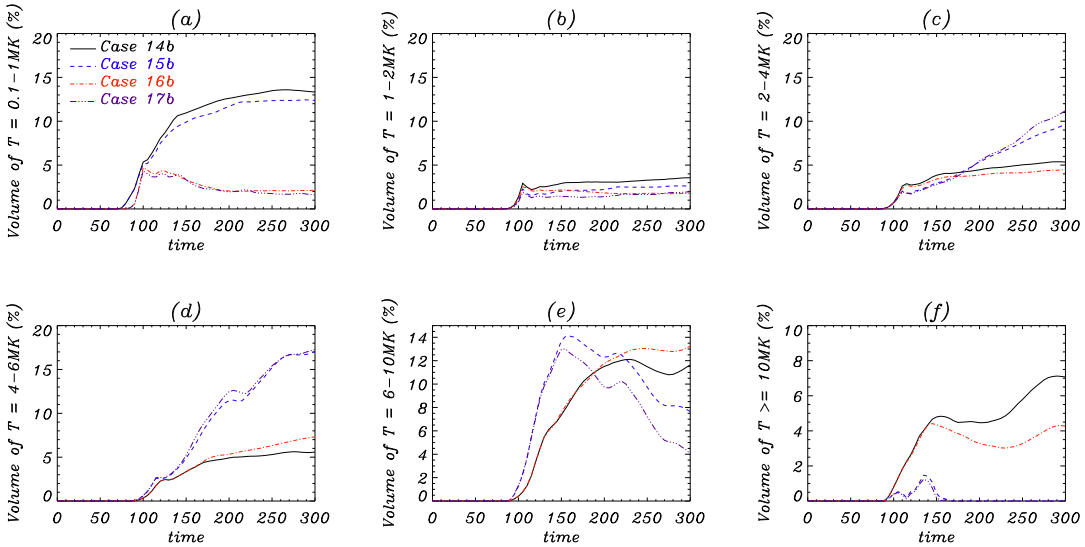

Figure B.8: The volume of cells over a certain temperature for Cases 14b-17b, where **(a)** 10^5 K $\leq T <$ 1 MK, **(b)** 1 MK $\leq T <$ 2 MK, **(c)** 2 MK $\leq T <$ 4 MK, **(d)** 4 MK $\leq T <$ 6 MK, **(e)** 6 MK $\leq T <$ 10 MK and **(f)** $T \geq$ 10 MK.

Bibliography

T. D. Arber, A. W. Longbottom, C. L. Gerrard, and A. M. Milne. A Staggered Grid, Lagrangian-Eulerian Remap Code for 3-D MHD Simulations. *Journal of Computational Physics*, 171: 151–181, July 2001. doi: 10.1006/jcph.2001.6780.

M. R. Bareford, P. K. Browning, and R. A. M. van der Linden. A nanoflare distribution generated by repeated relaxations triggered by kink instability. *Astron. Astrophys.*, 521:A70, October 2010. doi: 10.1051/0004-6361/201014067.

M. R. Bareford, P. K. Browning, and R. A. M. van der Linden. The Flare-Energy Distributions Generated by Kink-Unstable Ensembles of Zero-Net-Current Coronal Loops. *Solar Phys.*, 273: 93–115, October 2011. doi: 10.1007/s11207-011-9832-4.

M. A. Berger and G. B. Field. The topological properties of magnetic helicity. *Journal of Fluid Mechanics*, 147:133–148, October 1984. doi: 10.1017/S0022112084002019.

D. Biskamp. *Nonlinear magnetohydrodynamics*. 1993.

G. J. J. Botha, T. D. Arber, and A. W. Hood. Thermal conduction effects on the kink instability in coronal loops. *A&A*, 525:A96, 2011. doi: 10.1051/0004-6361/201015534. URL http://dx.doi.org/10.1051/0004-6361/201015534.

G. J. J. Botha, T. D. Arber, and A. K. Srivastava. Observational Signatures of the Coronal Kink Instability with Thermal Conduction. *Astrophys. J.*, 745:53, January 2012. doi: 10.1088/0004-637X/745/1/53.

T. J. M. Boyd and J. J. Sanderson. *The Physics of Plasmas*. January 2003.

S. J. Bradshaw and P. J. Cargill. Explosive heating of low-density coronal plasma. *Astron. Astrophys.*, 458:987–995, November 2006. doi: 10.1051/0004-6361:20065691.

S. J. Bradshaw and P. J. Cargill. The Cooling of Coronal Plasmas. III. Enthalpy Transfer as a Mechanism for Energy Loss. *Astrophys. J.*, 717:163–174, July 2010. doi: 10.1088/0004-637X/717/1/163.

P. K. Browning. Helicity injection and relaxation in a solar-coronal magnetic loop with a free surface. *Journal of Plasma Physics*, 40:263–280, October 1988.

P. K. Browning and R. A. M. Van der Linden. Solar coronal heating by relaxation events. *Astron. Astrophys.*, 400:355–367, March 2003. doi: 10.1051/0004-6361:20021887.

P. K. Browning, C. Gerrard, A. W. Hood, R. Kevis, and R. A. M. van der Linden. Heating the corona by nanoflares: simulations of energy release triggered by a kink instability. *Astron. Astrophys.*, 485:837–848, July 2008. doi: 10.1051/0004-6361:20079192.

P. J. Cargill. The Fine Structure of a Nanoflare-Heated Corona. *Solar Phys.*, 147:263–268, October 1993. doi: 10.1007/BF00690717.

P. J. Cargill. Some implications of the nanoflare concept. *Astrophys. J.*, 422:381–393, February 1994. doi: 10.1086/173733.

P. J. Cargill and J. A. Klimchuk. A Nanoflare Explanation for the Heating of Coronal Loops Observed by YOHKOH. *Astrophys. J.*, 478:799, March 1997. doi: 10.1086/303816.

P. J. Cargill and J. A. Klimchuk. Nanoflare Heating of the Corona Revisited. *Astrophys. J.*, 605: 911–920, April 2004. doi: 10.1086/382526.

S. Chandrasekhar. Stochastic Problems in Physics and Astronomy. *Reviews of Modern Physics*, 15:1–89, January 1943. doi: 10.1103/RevModPhys.15.1.

P. Charbonneau, S. W. McIntosh, H.-L. Liu, and T. J. Bogdan. Avalanche models for solar flares (Invited Review). *Solar Phys.*, 203:321–353, November 2001. doi: 10.1023/A:1013301521745.

S. Christe, I. G. Hannah, S. Krucker, J. McTiernan, and R. P. Lin. RHESSI Microflare Statistics. I. Flare-Finding and Frequency Distributions. *Astrophys. J.*, 677:1385–1394, April 2008. doi: 10.1086/529011.

T. G. Cowling. *Magnetohydrodynamics*. 1976.

I. De Moortel. An overview of coronal seismology. *Royal Society of London Philosophical Transactions Series A*, 363:2743–2760, December 2005. doi: 10.1098/rsta.2005.1665.

I. De Moortel and S. J. Bradshaw. Forward Modelling of Coronal Intensity Perturbations. *Solar Phys.*, 252:101–119, October 2008. doi: 10.1007/s11207-008-9238-0.

I. De Moortel and K. Galsgaard. Numerical modelling of 3D reconnection due to rotational footpoint motions. *Astron. Astrophys.*, 451:1101–1115, June 2006a. doi: 10.1051/0004-6361:20054587.

I. De Moortel and K. Galsgaard. Numerical modelling of 3D reconnection. II. Comparison between rotational and spinning footpoint motions. *Astron. Astrophys.*, 459:627–639, November 2006b. doi: 10.1051/0004-6361:20065716.

I. De Moortel and D. J. Pascoe. The Effects of Line-of-sight Integration on Multistrand Coronal Loop Oscillations. *Astrophys. J.*, 746:31, February 2012. doi: 10.1088/0004-637X/746/1/31.

I. De Moortel, P. Browning, S. J. Bradshaw, B. Pintér, and E. P. Kontar. The way forward for coronal heating. *Astronomy and Geophysics*, 49(3):030000–3, June 2008. doi: 10.1111/j.1468-4004.2008.49321.x.

P. Demoulin, J. C. Henoux, E. R. Priest, and C. H. Mandrini. Quasi-Separatrix layers in solar flares. I. Method. *Astron. Astrophys.*, 308:643–655, April 1996.

J. A. Eddy and R. Ise. *A new sun : the solar results from SKYLAB*. April 1979.

L. Einkemmer and A. Ostermann. An almost symmetric Strang splitting scheme for nonlinear evolution equations. *ArXiv e-prints*, September 2013.

J. M. Finn and T. A. Antonsen. Magnetic Helicity: What Is It and What Is It Good For? *Commun. Plas. Phys. Cont. Fus.*, 9:111–126, 1985.

R. A. Freedman and W. J. Kaufmann. *Universe: Stars & Galaxies w/Starry Night Enthusiast*.

2008.

G. A. Gary. Plasma Beta above a Solar Active Region: Rethinking the Paradigm. *Solar Phys.*, 203:71–86, October 2001. doi: 10.1023/A:1012722021820.

M. Gordovskyy and P. K. Browning. Particle Acceleration by Magnetic Reconnection in a Twisted Coronal Loop. *Astrophys. J.*, 729:101, March 2011. doi: 10.1088/0004-637X/729/2/101.

M. Güdel, M. Audard, V. L. Kashyap, J. J. Drake, and E. F. Guinan. Are Coronae of Magnetically Active Stars Heated by Flares? II. Extreme Ultraviolet and X-Ray Flare Statistics and the Differential Emission Measure Distribution. *Astrophys. J.*, 582:423–442, January 2003. doi: 10.1086/344614.

I. G. Hannah, S. Christe, S. Krucker, G. J. Hurford, H. S. Hudson, and R. P. Lin. RHESSI Microflare Statistics. II. X-Ray Imaging, Spectroscopy, and Energy Distributions. *Astrophys. J.*, 677:704–718, April 2008a. doi: 10.1086/529012.

I. G. Hannah, S. Krucker, H. S. Hudson, S. Christe, and R. P. Lin. An intriguing solar microflare observed with RHESSI, Hinode, and TRACE. *Astron. Astrophys.*, 481:L45–L48, April 2008b. doi: 10.1051/0004-6361:20079019.

J. Heyvaerts and E. R. Priest. Coronal heating by reconnection in DC current systems - A theory based on Taylor's hypothesis. *Astron. Astrophys.*, 137:63–78, August 1984.

A. W. Hood. Photospheric line-tying conditions for the MHD stability of coronal magnetic fields. *Solar Phys.*, 105:307–312, June 1986. doi: 10.1007/BF00172049.

A. W. Hood, P. K. Browning, and R. A. M. van der Linden. Coronal heating by magnetic reconnection in loops with zero net current. *Astron. Astrophys.*, 506:913–925, November 2009. doi: 10.1051/0004-6361/200912285.

H. S. Hudson. Solar flares, microflares, nanoflares, and coronal heating. *Solar Phys.*, 133:357–369, June 1991. doi: 10.1007/BF00149894.

J. A. Klimchuk. Cross-Sectional Properties of Coronal Loops. volume 193, pages 53–75, April 2000. doi: 10.1023/A:1005210127703.

J. A. Klimchuk and P. J. Cargill. Observational Signatures of Nanoflare-Heated Loops. *AGU Spring Meeting Abstracts*, page 52, May 2001.

J. A. Klimchuk, S. Patsourakos, and P. J. Cargill. Highly Efficient Modeling of Dynamic Coronal Loops. *Astrophys. J.*, 682:1351–1362, August 2008. doi: 10.1086/589426.

K. R. Lang. *The Cambridge Encyclopedia of the Sun*. August 2001.

R. P. Lin, R. A. Schwartz, S. R. Kane, R. M. Pelling, and K. C. Hurley. Solar hard X-ray microflares. *Astrophys. J.*, 283:421–425, August 1984. doi: 10.1086/162321.

R. Lionello, M. Velli, G. Einaudi, and Z. Mikic. Nonlinear Magnetohydrodynamic Evolution of Line-tied Coronal Loops. *Astrophys. J.*, 494:840–+, February 1998. doi: 10.1086/305221.

D. W. Longcope. Separator current sheets: Generic features in minimum-energy magnetic fields subject to flux constraints. *Physics of Plasmas*, 8:5277–5290, December 2001. doi: 10.1063/1.1418431.

D. W. Longcope. Topological Methods for the Analysis of Solar Magnetic Fields. *Living Reviews*

in Solar Physics, 2:7, November 2005. doi: 10.12942/lrsp-2005-7.

D. W. Longcope and S. C. Cowley. Current sheet formation along three-dimensional magnetic separators. *Physics of Plasmas*, 3:2885–2897, August 1996. doi: 10.1063/1.871627.

E. T. Lu and R. J. Hamilton. Avalanches and the distribution of solar flares. *Astrophys. J. Lett.*, 380:L89–L92, October 1991. doi: 10.1086/186180.

E. T. Lu, R. J. Hamilton, J. M. McTiernan, and K. R. Bromund. Solar flares and avalanches in driven dissipative systems. *Astrophys. J.*, 412:841–852, August 1993. doi: 10.1086/172966.

C. Mellor, C. L. Gerrard, K. Galsgaard, A. W. Hood, and E. R. Priest. Numerical Simulations of the Flux Tube Tectonics Model for Coronal Heating. *Solar Phys.*, 227:39–60, March 2005. doi: 10.1007/s11207-005-1713-2.

R. Mitalas and K. R. Sills. On the photon diffusion time scale for the sun. *Astrophys. J.*, 401:759, December 1992. doi: 10.1086/172103.

V. M. Nakariakov and E. Verwichte. Coronal Waves and Oscillations. *Living Reviews in Solar Physics*, 2:3, July 2005. doi: 10.12942/lrsp-2005-3.

V. M. Nakariakov, L. Ofman, E. E. Deluca, B. Roberts, and J. M. Davila. TRACE observation of damped coronal loop oscillations: Implications for coronal heating. *Science*, 285:862–864, August 1999. doi: 10.1126/science.285.5429.862.

E. N. Parker. Sweet's Mechanism for Merging Magnetic Fields in Conducting Fluids. *J. Geophys. Res.*, 62:509–520, December 1957. doi: 10.1029/JZ062i004p00509.

E. N. Parker. Topological Dissipation and the Small-Scale Fields in Turbulent Gases. *Astrophys. J.*, 174:499, June 1972. doi: 10.1086/151512.

E. N. Parker. Magnetic Neutral Sheets in Evolving Fields - Part Two - Formation of the Solar Corona. *Astrophys. J.*, 264:642–+, January 1983. doi: 10.1086/160637.

E. N. Parker. Nanoflares and the solar X-ray corona. *Astrophys. J.*, 330:474–479, July 1988. doi: 10.1086/166485.

C. E. Parnell and I. De Moortel. A contemporary view of coronal heating. *Royal Society of London Philosophical Transactions Series A*, 370:3217–3240, July 2012. doi: 10.1098/rsta.2012.0113.

C. E. Parnell and A. L. Haynes. Three-Dimensional Magnetic Reconnection. In S. S. Hasan and R. J. Rutten, editors, *Magnetic Coupling between the Interior and Atmosphere of the Sun*, pages 261–276, 2010. doi: 10.1007/978-3-642-02859-5_20.

H. E. Petschek. Magnetic Field Annihilation. *NASA Special Publication*, 50:425, 1964.

D. I. Pontin and I. J. D. Craig. Current singularities at finitely compressible three-dimensional magnetic null points. *Physics of Plasmas*, 12(7):072112, July 2005. doi: 10.1063/1.1987379.

D. I. Pontin and I. J. D. Craig. Dynamic Three-dimensional Reconnection in a Separator Geometry with Two Null Points. *Astrophys. J.*, 642:568–578, May 2006. doi: 10.1086/500725.

D. I. Pontin, G. Hornig, and E. R. Priest. Kinematic reconnection at a magnetic null point: spine-aligned current. *Geophysical and Astrophysical Fluid Dynamics*, 98:407–428, May 2004. doi: 10.1080/0309192042000272324.

D. I. Pontin, A. Bhattacharjee, and K. Galsgaard. Current sheets at three-dimensional magnetic

nulls: Effect of compressibility. *Physics of Plasmas*, 14(5):052109, May 2007. doi: 10.1063/1.2734949.

D. I. Pontin, A. L. Wilmot-Smith, G. Hornig, and K. Galsgaard. Dynamics of braided coronal loops. II. Cascade to multiple small-scale reconnection events. *Astron. Astrophys.*, 525:A57, January 2011. doi: 10.1051/0004-6361/201014544.

J. G. Porter, J. Toomre, and K. B. Gebbie. Frequent ultraviolet brightenings observed in a solar active region with solar maximum mission. *Astrophys. J.*, 283:879–886, August 1984. doi: 10.1086/162375.

E. Priest and T. Forbes. *Magnetic Reconnection*. June 2000.

E. R. Priest. *Solar magneto-hydrodynamics*. 1982.

E. R. Priest and P. Démoulin. Three-dimensional magnetic reconnection without null points. 1. Basic theory of magnetic flipping. *J. Geophys. Res.*, 100:23443–23464, December 1995. doi: 10.1029/95JA02740.

E. R. Priest and A. W. Hood, editors. *Advances in Solar System Magnetohydrodynamics, 1991*, June 1991.

E. R. Priest, T. N. Bungey, and V. S. Titov. The 3D topology and interaction of complex magnetic flux systems. *Geophysical and Astrophysical Fluid Dynamics*, 84:127–163, 1997. doi: 10.1080/03091929708208976.

E. R. Priest, J. F. Heyvaerts, and A. M. Title. A Flux-Tube Tectonics Model for Solar Coronal Heating Driven by the Magnetic Carpet. *Astrophys. J.*, 576:533–551, September 2002. doi: 10.1086/341539.

A. F. Rappazzo, M. Velli, G. Einaudi, and R. B. Dahlburg. Coronal Heating, Weak MHD Turbulence, and Scaling Laws. *Astrophys. J. Lett.*, 657:L47–L51, March 2007. doi: 10.1086/512975.

A. F. Rappazzo, M. Velli, G. Einaudi, and R. B. Dahlburg. Nonlinear Dynamics of the Parker Scenario for Coronal Heating. *Astrophys. J.*, 677:1348–1366, April 2008. doi: 10.1086/528786.

F. Reale. Coronal Loops: Observations and Modeling of Confined Plasma. *Living Reviews in Solar Physics*, 7:5, November 2010. doi: 10.12942/lrsp-2010-5.

F. Reale and E. Landi. The role of radiative losses in the late evolution of pulse-heated coronal loops/strands. *Astron. Astrophys.*, 543:A90, July 2012. doi: 10.1051/0004-6361/201219280.

F. Reale, G. Peres, S. Serio, R. M. Betta, E. E. DeLuca, and L. Golub. A Brightening Coronal Loop Observed by TRACE. II. Loop Modeling and Constraints on Heating. *Astrophys. J.*, 535:423–437, May 2000. doi: 10.1086/308817.

B. Roberts, P. M. Edwin, and A. O. Benz. On coronal oscillations. *Astrophys. J.*, 279:857–865, April 1984. doi: 10.1086/161956.

R. Rosner, W. H. Tucker, and G. S. Vaiana. Dynamics of the quiescent solar corona. *Astrophys. J.*, 220:643–645, March 1978. doi: 10.1086/155949.

Y. Sakamoto, S. Tsuneta, and G. Vekstein. A Nanoflare Heating Model and Comparison with Observations. *Astrophys. J.*, 703:2118–2130, October 2009. doi: 10.1088/0004-637X/703/2/

2118.

A. Sarkar and R. W. Walsh. Hydrodynamic Simulation of a Nanoflare-heated Multistrand Solar Atmospheric Loop. *Astrophys. J.*, 683:516–526, August 2008. doi: 10.1086/589552.

K. Schindler, M. Hesse, and J. Birn. General magnetic reconnection, parallel electric fields, and helicity. *J. Geophys. Res.*, 93:5547–5557, June 1988. doi: 10.1029/JA093iA06p05547.

P. A. Sweet. The Neutral Point Theory of Solar Flares. In B. Lehnert, editor, *Electromagnetic Phenomena in Cosmical Physics*, volume 6 of *IAU Symposium*, page 123, 1958.

J. B. Taylor. Relaxation of Toroidal Plasma and Generation of Reverse Magnetic Fields. *Physical Review Letters*, 33:1139–1141, November 1974. doi: 10.1103/PhysRevLett.33.1139.

J. B. Taylor. Relaxation and magnetic reconnection in plasmas. *Reviews of Modern Physics*, 58: 741–763, July 1986. doi: 10.1103/RevModPhys.58.741.

P. Testa, B. De Pontieu, J. Martínez-Sykora, E. DeLuca, V. Hansteen, J. Cirtain, A. Winebarger, L. Golub, K. Kobayashi, K. Korreck, S. Kuzin, R. Walsh, C. DeForest, A. Title, and M. Weber. Observing Coronal Nanoflares in Active Region Moss. *Astrophys. J. Lett.*, 770:L1, June 2013. doi: 10.1088/2041-8205/770/1/L1.

V. S. Titov, G. Hornig, and P. Démoulin. Theory of magnetic connectivity in the solar corona. *Journal of Geophysical Research (Space Physics)*, 107:1164, August 2002. doi: 10.1029/2001JA000278.

A. Vourlidas, J. A. Klimchuk, C. M. Korendyke, T. D. Tarbell, and B. N. Handy. On the Correlation between Coronal and Lower Transition Region Structures at Arcsecond Scales. *Astrophys. J.*, 563:374–380, December 2001. doi: 10.1086/323835.

A. L. Wilmot-Smith, D. I. Pontin, and G. Hornig. Dynamics of braided coronal loops. I. Onset of magnetic reconnection. *Astron. Astrophys.*, 516:A5, June 2010. doi: 10.1051/0004-6361/201014041.

G. L. Withbroe and R. W. Noyes. Mass and energy flow in the solar chromosphere and corona. *Annual. Rev. Astron. Astrophys.*, 15:363–387, 1977. doi: 10.1146/annurev.aa.15.090177.002051.

A. R. Yeates and G. Hornig. Unique topological characterization of braided magnetic fields. *Physics of Plasmas*, 20(1):012102, January 2013. doi: 10.1063/1.4773903.

T. Yokoyama, K. Akita, T. Morimoto, K. Inoue, and J. Newmark. Clear Evidence of Reconnection Inflow of a Solar Flare. *Astrophys. J. Lett.*, 546:L69–L72, January 2001. doi: 10.1086/318053.

H. Zirin and R. Cameron. New Studies of Polar Spicules. In *American Astronomical Society Meeting Abstracts #192*, volume 30 of *Bulletin of the American Astronomical Society*, page 840, May 1998.

	Resolution:	Test Objectives:
Chapter 3		Single thread: parameter studies
Case 1	$80^2 \times 160$	Low resolution
Case 2	$80^2 \times 160$	Low resolution and non-zero background resistivity
Case 3	$160^2 \times 320$	Medium resolution
Case 4	$320^2 \times 640$	High resolution
Case 5	$320 \times 160 \times 640$	Twist parameter $\lambda = 1.8$ in a double size domain
Case 5b	160^3	Twist parameter $\lambda = 1.8$ for 600 Alfvén times
Case 6	$320 \times 160 \times 640$	Twist parameter $\lambda = 1.6$ in a double size domain
Case 6b	160^3	Twist parameter $\lambda = 1.6$ for 600 Alfvén times
Case 7	$320 \times 160 \times 640$	Twist parameter $\lambda = 1.4$ in a double size domain
Case 7b	160^3	Twist parameter $\lambda = 1.4$ for 600 Alfvén times
Chapter 3		Two threads: avalanche effects
Case 8	640×320^2	Threads are 2 units away with twist parameters $\lambda = 1.8$
Case 9	640×320^2	Threads are side by side with twist parameters $\lambda = 1.8$
Case 10	640×320^2	Threads are 2 units away, the thread to be destabilised (if possible) has twist parameter reduces to $\lambda = 1.6$
Case 11	640×320^2	Threads are side by side, the thread to be destabilised (if possible) has twist parameter reduces to $\lambda = 1.6$
Case 12	640×320^2	Threads are 2 units away, the thread to be destabilised (if possible) has twist parameter reduces to $\lambda = 1.4$
Case 13	640×320^2	Threads are side by side, the thread to be destabilised (if possible) has twist parameter reduces to $\lambda = 1.6$
Chapter 4		Single thread: cooling effects
Case 14	$100^2 \times 400$	Reference case
Case 15	$100^2 \times 400$	With thermal conduction effect
Case 16	$100^2 \times 400$	With optically thin radiation effect
Case 17	$100^2 \times 400$	With both thermal conduction and optically thin radiation
Case 18	$100^2 \times 400$	With both thermal conduction and optically thin radiation and enhance the radiation effect by 4
Case 19	$100^2 \times 400$	With both thermal conduction and optically thin radiation and enhance the radiation effect by 9
Appendix B		Single thread: enhance radiation effects
Case 14b	$100^2 \times 400$	Reference case
Case 15b	$100^2 \times 400$	With thermal conduction effect
Case 16b	$100^2 \times 400$	With optically thin radiation effect
Case 17b	$100^2 \times 400$	With both thermal conduction and optically thin radiation
Case 18b	$100^2 \times 400$	With both thermal conduction and optically thin radiation and enhance the radiation effect by 4
Case 19b	$100^2 \times 400$	With both thermal conduction and optically thin radiation and enhance the radiation effect by 9

A summary of all the simulations investigated in this thesis.